

AD-A050 075

STANFORD UNIV CALIF EDWARD L GINZTON LAB
ENERGY STORAGE AND TWO-PHOTON EXTRACTION FROM METASTABLE STATES--ETC(U)
NOV 77 H KOMINE

F/6 20/5

F44620-74-C-0039

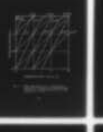
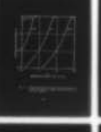
UNCLASSIFIED

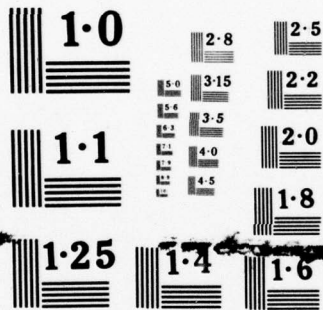
GL-2753

AFOSR-TR-78-0077

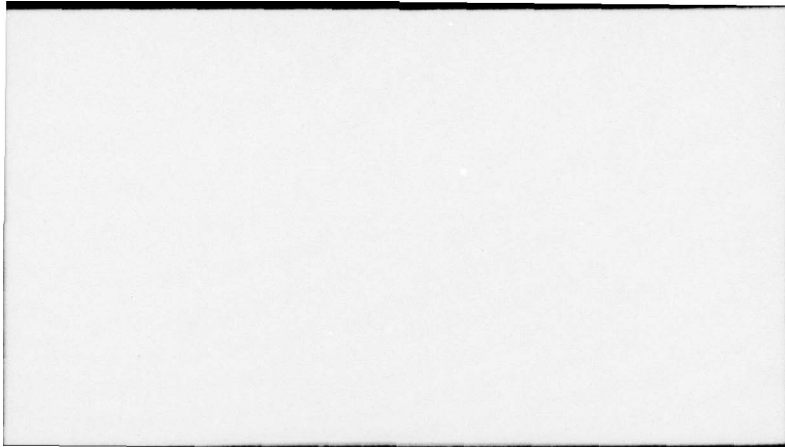
NL

1 OF 2
ADA
050075





NATIONAL BUREAU OF STANDARDS
MICROCOPY RESOLUTION TEST CHART



2

6 ENERGY STORAGE AND TWO-PHOTON EXTRACTION FROM METASTABLE STATES

by

10 Hiroshi/Komine

L. Report No. 2753

11 Nov 1977

12 165 p.

14 GL-2753

7 Final Report, 19 Apr 74 - 30 Jun 77,

for

15 F44620-74-C-0039

16 2301

17 A1

18 AFOSR

19 TR-78-0077 for the period

19 April 1974 - 30 June 1977

AIR FORCE OFFICE OF SCIENTIFIC RESEARCH (AFSC) NOTICE OF TRANSMITTAL TO DDC

This technical report has been reviewed and is approved for public release IAW AFR 190-12 (7b). Distribution is unlimited.

A. D. BLOSE Technical Information Officer

Edward L. Ginzton Laboratory W.W. Hansen Laboratories of Physics Stanford University Stanford, California

DISTRIBUTION STATEMENT A Approved for public release; Distribution Unlimited

DDC RECEIVED FEB 16 1978 B 409 640

UNCLASSIFIED

SECURITY CLASSIFICATION OF THIS PAGE (When Data Entered)

REPORT DOCUMENTATION PAGE		READ INSTRUCTIONS BEFORE COMPLETING FORM								
1. REPORT NUMBER AFOSR-TR. 78-0077	2. GOVT ACCESSION NO.	3. RECIPIENT'S CATALOG NUMBER								
4. TITLE (and Subtitle) ENERGY STORAGE AND TWO-PHOTON EXTRACTION FROM METASTABLE STATES	5. TYPE OF REPORT & PERIOD COVERED Final Report 19 April 74 - 30 June 1977									
	6. PERFORMING ORG. REPORT NUMBER G.L. Report No. 2753									
7. AUTHOR(s) Hiroshi Komine	8. CONTRACT OR GRANT NUMBER(s) F44620-74-C-0039									
9. PERFORMING ORGANIZATION NAME AND ADDRESS Edward L. Ginzton Laboratory W.W. Hansen Laboratories of Physics Stanford University, Stanford, CA 94305	10. PROGRAM ELEMENT, PROJECT, TASK AREA & WORK UNIT NUMBERS 2301/A1 61102F									
11. CONTROLLING OFFICE NAME AND ADDRESS Air Force Office of Scientific Research/INP Bolling AFB, Building 410 Washington, D. C. 20332	12. REPORT DATE November 1977									
	13. NUMBER OF PAGES 161									
14. MONITORING AGENCY NAME & ADDRESS (if different from Controlling Office)	15. SECURITY CLASS. (of this report) Uncl									
	15a. DECLASSIFICATION/DOWNGRADING SCHEDULE									
16. DISTRIBUTION STATEMENT (of this Report) Approved for public release; distribution unlimited										
17. DISTRIBUTION STATEMENT (of the abstract entered in Block 20, if different from Report)										
18. SUPPLEMENTARY NOTES										
19. KEY WORDS (Continue on reverse side if necessary and identify by block number)										
<table border="0"> <tr> <td>excited metastable species</td> <td>metastable states</td> </tr> <tr> <td>optical energy extraction</td> <td>high energy optical pulses</td> </tr> <tr> <td>two-photon transitions</td> <td>laser fusion</td> </tr> <tr> <td>high power laser applications</td> <td>photochemical studies</td> </tr> </table>			excited metastable species	metastable states	optical energy extraction	high energy optical pulses	two-photon transitions	laser fusion	high power laser applications	photochemical studies
excited metastable species	metastable states									
optical energy extraction	high energy optical pulses									
two-photon transitions	laser fusion									
high power laser applications	photochemical studies									
20. ABSTRACT (Continue on reverse side if necessary and identify by block number) This dissertation presents experimental studies on the energy storage characteristics of excited metastable species and theoretical analysis of optical energy extraction schemes based on stimulated two-photon transitions. Metastable states of atoms and molecules have recently received attention as optical energy storage media for potential high power laser applications. The large energy capacity and long lifetime of metastable states offer attractive properties for generating high energy optical pulses for laser fusion and photochemical studies. Recent experimental results on the metastable states of molecular mercury										

DD FORM 1473 1 JAN 73 EDITION OF 1 NOV 65 IS OBSOLETE

UNCLASSIFIED

SECURITY CLASSIFICATION OF THIS PAGE (When Data Entered)

2 next page

20. (continued)

illustrate some of the important properties of energy storage in a gaseous medium. In particular, collisional deactivation of excited metastable species by mutual two-body quenching and by molecular formation are discussed in relation to storage limitations. The measured quenching rate constant in the mercury dimer system suggests a maximum storage density on the order of 10^{17} cm^{-3} with a lifetime of 0.1 microsecond, which corresponds to an optical energy capacity of 50 joules per liter. The optical extraction of energy stored in an inverted metastable system using stimulated two-photon transitions offers nonlinear characteristics not available in the ordinary laser amplifiers. Since the extraction efficiency is an important amplifier parameter, the growth of an optical pulse in the steady-state approximation is investigated theoretically including the saturation of the medium. Analytical expressions for the extraction efficiency of an ideal two-photon emission amplifier are derived. The feasibility of two-photon amplifier is discussed with two proposed systems in atomic mercury and atomic iodine. The semi-empirical methods of gain calculation are described for the near-resonance case and the non-resonant case. The use of spherical tensor operator algebra and the evaluation of electric dipole matrix elements in the intermediate angular momentum coupling scheme are discussed. The experimental requirements for the proposed systems based on the calculated gains indicate that the currently available pumping methods and trigger laser sources may lead to a demonstration of two-photon amplification and energy extraction.

ACCESSION for		
NTIS	White Section	<input checked="" type="checkbox"/>
DDC	Buff Section	<input type="checkbox"/>
UNANNOUNCED		<input type="checkbox"/>
JUSTIFICATION _____		
BY _____		
DISTRIBUTION/AVAILABILITY CODES		
Dist.	AVAIL.	and/or SPECIAL
A		

ABSTRACT

This dissertation presents experimental studies on the energy storage characteristics of excited metastable species and theoretical analysis of optical energy extraction schemes based on stimulated two photon transitions.

Metastable states of atoms and molecules have recently received attention as optical energy storage media for potential high power laser applications. The large energy capacity and long lifetime of metastable states offer attractive properties for generating high energy optical pulses for laser fusion and photochemical studies.

Recent experimental results on the metastable states of molecular mercury illustrate some of the important properties of energy storage in a gaseous medium. In particular, collisional deactivation of excited metastable species by mutual two-body quenching and by molecular formation are discussed in relation to storage limitations. The measured quenching rate constant in the mercury dimer system suggests a maximum storage density on the order of 10^{17} cm^{-3} with a lifetime of 0.1 microsecond, which corresponds to an optical energy capacity of 50 joules per liter.

The optical extraction of energy stored in an inverted metastable system using stimulated two photon transitions offers nonlinear characteristics not available in the ordinary

laser amplifiers. Since the extraction efficiency is an important amplifier parameter, the growth of an optical pulse in the steady-state approximation is investigated theoretically including the saturation of the medium. Analytical expressions for the extraction efficiency of an ideal two-photon emission amplifier are derived.

The feasibility of two photon amplifier is discussed with two proposed systems in atomic mercury and atomic iodine. The semi-empirical methods of gain calculation are described for the near-resonance case and the non-resonant case. The use of spherical tensor operator algebra and the evaluation of electric dipole matrix elements in the intermediate angular momentum coupling scheme are discussed. The experimental requirements for the proposed systems based on the calculated gains indicate that the currently available pumping methods and trigger laser sources may lead to a demonstration of two photon amplification and energy extraction.

ACKNOWLEDGEMENTS

I would like to thank all those who have contributed to the successful completion of this work. In particular, I gratefully thank Professor Robert L. Byer for suggesting the research topics and providing constant encouragement with dynamic enthusiasm and expert guidance. His creative insight and lucid explanation continue to stimulate my interest in the physical sciences and help to develop mature understanding and professional skills. The experience gained under his guidance will surely be an invaluable part of my graduate education.

I wish to express my gratitude to Dr. Richard L. Herbst for his technical assistance on innumerable occasions and for sharing interest in my work. His engineering ingenuity is an inspiration for inventive solutions to design problems. I would also like to thank Professor S. E. Harris for useful discussions on some of the theoretical aspects of this work during the early part of my research. Many thanks are due to the students in the quantum electronics group for their support, cooperation, and friendship.

I gratefully acknowledge Professor A. E. Siegman and Professor M. Weissbluth for their critical reading of the manuscript.

My thankful acknowledgement extends to the technical staff of the Ginzton Laboratory: Ben Yoshizumi provided the expertise in high voltage electronics and numerous other skills; and George Kotler prepared a number of nonlinear optics crystals. Paul Constantinitis of the Student Machine Shop patiently instructed me the proper use of the tools and the techniques. The glassblowing and other specialized services rendered by Frank Peters of the SEL Tube Shop are also appreciated.

I am truly indebted to Mary Farley for her generous and expert assistance in typing this manuscript. Her cheerful support and friendship helped the task of completing this dissertation. I am also appreciative of Norm Bettini and his staff for providing the drafting services.

To my parents, Mr. and Mrs. Shoji Komine, I owe many thanks for sharing interest in my higher education and giving constant encouragement for my vocational goals with enthusiastic support and understanding. Finally, I owe special thanks to my wife, Yuriko, for her love, understanding, and patience during the course of my graduate studies at Stanford.

TABLE OF CONTENTS

	Page
ABSTRACT.....	iii
ACKNOWLEDGEMENTS.....	v
LIST OF FIGURES.....	x
LIST OF TABLES.....	xiii
 CHAPTER	
I. INTRODUCTION.....	1
II. ENERGY STORAGE IN METASTABLE STATES.....	3
A. Introduction.....	3
B. Classification of Metastable States..	3
1. Atoms.....	3
2. Diatomic Molecules.....	6
C. Energy Storage Lifetime and Capacity.	9
1. Introduction.....	9
2. Spontaneous Radiative Decay.....	10
3. Population Inversion and Super- fluorescence.....	16
4. Non-Radiative Loss Mechanisms....	24
5. Scaling.....	31
III. TWO PHOTON ENERGY EXTRACTION.....	33
A. Introduction.....	33
B. Theory.....	34
C. Two Photon Amplification.....	43
D. Energy Extraction.....	50

	Page
IV. PROPOSED SYSTEMS AND FEASIBILITY ANALYSIS....	68
A. Introduction.....	68
B. Atomic Mercury ASRS Frequency Up- Converter.....	69
1. Population Inversion and Storage Mechanism.....	69
2. Two Photon Gain Calculations.....	72
C. Atomic Iodine TPE and ASRS Amplifier....	86
1. Iodine System.....	86
2. Non-Resonant Two Photon Gain.....	88
3. Experiment.....	93
V. CONCLUSION.....	99
APPENDICES	
A. OPTICALLY PUMPED Hg ₂ STUDIES.....	102
B. OPTICALLY PUMPED ATOMIC MERCURY PHOTO- DISSOCIATION LASER.....	113
C. POLARIZATION PROPERTIES OF TWO PHOTON TRANSITIONS.....	117
D. REDUCED MATRIX ELEMENT, SPONTANEOUS EMISSION RATE, AND OSCILLATOR STRENGTH IN TWO PHOTON TRANSITIONS.....	131

	Page
E. PROPOSED ATOMIC MERCURY ANTI-STOKES FREQUENCY CONVERTER.....	142
REFERENCES.....	145

LIST OF FIGURES

	Page
1. Radiative decay of metastable states : a) intercombination electric dipole (E1) transition with a change in parity; b) magnetic dipole (M1), electric quad- rupole (E2), and two-photon emission (TPE) transitions with no parity change	11
2. One and two photon energy extraction schemes: a) ordinary one photon laser transition at ω_0 ; b) stimulated TPE amplification at ω_1 and ω_2 ; c) stimulated ASRS amplification at ω_3	35
3. Two-level system for two photon extraction analysis.....	37
4. Ideal TPE amplifier extraction efficiency vs normalized input (trigger) photon flux at ω_1 for $r_2 = \exp(-10)$	58
5. Ideal TPE amplifier extraction efficiency vs normalized input (trigger) photon flux at ω_1 for $r_2 = \exp(-5)$	59
6. Ideal degenerate ($\omega_1 = \omega_2$) TPE amplifier extraction efficiency vs normalized input photon flux.....	62

7. Energy level structure for two photon gain medium:
- a) intermediate states $|k\rangle$ above the energy storage state $|b\rangle$;
 - b) intermediate states $|k\rangle$ below $|b\rangle$ in which radiative decay from $|b\rangle$ to $|k\rangle$ is allowed..... 66
8. Abbreviated energy level diagram of atomic mercury for ASRS amplifier..... 70
9. ASRS cross-section vs incident (trigger) photon energy $\hbar\omega_1$ for the Hg ($6^1P_1^0 \Rightarrow 6^3P_0^0$) transition..... 77
10. ASRS cross-section vs incident photon energy $\hbar\omega_1$ for the Hg ($6^1P_1^0 \Rightarrow 6^3P_1^0$) transition..... 78
11. ASRS cross-section vs incident photon energy $\hbar\omega_1$ for the Hg ($6^1P_1^0 \Rightarrow 6^3P_2^0$) transition..... 79
12. Abbreviated energy level diagram of atomic iodine for TPE and ASRS amplifier..... 87
13. Photolytic production of population inversion in atomic iodine system:

a) Photolysis of C_3F_7I with 266 nm radiation and optical gain at the 1.315 μm transition;	
b) schematic TPE and ASRS amplification and energy extraction in the iodine system.....	94

LIST OF TABLES

	Page
I. Ideal TPE Amplifier Parameters.....	64
II. The Values of R_k for Mercury.....	75
III. $(d\sigma/d\Omega)_{ASRS}$ at 1.064 μm and 10.6 μm for Hg ($6^1P_1^0 \Rightarrow 6^3P_J^0$).....	81
IV. $(d\sigma/d\Omega)_{TPE}$ at 1.064 μm and 10.6 μm for Hg ($6^1P_1^0 \Rightarrow 6^3P_J^0$).....	83
V. Two Photon Gain Coefficients at 1.064 μm and 10.6 μm for Hg ($6^1P_1^0 \Rightarrow 6^3P_J^0$).....	84
VI. I ($2P_{1/2}^0 \Rightarrow 2P_{3/2}^0$) : $(d\sigma/d\Omega)$ and Intensity Gain Coefficient δ	92

CHAPTER I

INTRODUCTION

This dissertation presents experimental studies on the energy storage characteristics of excited metastable species and theoretical analysis of optical energy extraction schemes based on stimulated two photon transitions.

Metastable states of atoms and molecules have recently received attention as optical energy storage media for potential high power laser applications. The large energy capacity and long lifetime of metastable states offer attractive properties for generating high energy optical pulses for laser fusion and photochemical studies.¹

The energy storage characteristics of metastable systems at high population inversion densities of interest depend on two decay processes. They are stimulated radiative decay by amplified spontaneous emission, or superfluorescence, and non-radiative loss mechanisms. Chapter II examines the effect of the two decay processes on the storage capacity and lifetime as well as on the scaling properties. Recent experimental results on the metastable states of molecular mercury illustrate some of the important properties of energy storage in a gaseous medium.² In particular collisional deactivation of excited metastable species by mutual two-body quenching and by molecular formation are analyzed.

The optical extraction of stored energy normally uses a laser transition at a frequency within the gain bandwidth of the inverted medium. An alternative to this approach involves stimulated two photon transitions when such transitions are permitted.

The concept of a two-photon laser was first introduced by Sorokin and Braslau³ in 1964, and by Prokhorov in 1965.⁴ Several years later Letokhov⁵ also proposed amplification by stimulated two-photon emission. Despite these early proposals the two photon energy extraction schemes did not receive much attention until its nonlinear properties were recognized for potential applications in laser fusion.⁶

Chapter III presents the elements of the theory of two photon amplification and investigates the energy extraction efficiency including the saturation of the active medium.

Chapter IV describes two proposed systems in atomic mercury and iodine and discusses experimental feasibility of each system. Frequency up-conversion in Hg using anti-Stokes Raman scattering illustrates the near-resonance enhancement of two photon gain.⁷ The atomic iodine system represents a non-resonant gain medium for stimulated two-photon emission and anti-Stokes Raman scattering.^{6,8}

Chapter V summarizes the findings of this work. The implications of storage limitations and the prospects of demonstrating a two-photon laser are discussed.

CHAPTER II

ENERGY STORAGE IN METASTABLE STATES

A. INTRODUCTION

The metastable states of atoms and molecules have been considered for producing high densities of a long-lived inverted medium for energy storage with potential applications in high power laser systems.¹ The atomic iodine laser^{9,10} which operates on the $^2P_{1/2} - ^2P_{3/2}$ transition is a demonstrated example of energy storage and optical extraction from a metastable state. This chapter describes various types of metastable states and the decay properties that determine the energy storage characteristics. Some of the representative characteristics of metastable states are illustrated with data on atomic iodine and recent experimental results on molecular mercury. The details of the Hg_2 experiments are presented in Appendices A and B.

B. CLASSIFICATION OF METASTABLE STATES

1. Atoms

The metastable states of excited atoms arise from a lack of strongly allowed radiative decay channels for returning to the ground state. Since the strength of radiative transitions depends on the matrix elements of the radiative interaction, strongly allowed transitions occur between states with

non-vanishing matrix elements of the electric dipole operator. The geometrical factor in the matrix element gives the selection rules for strongly allowed transitions. The general selection rules for the total electronic angular momentum, J , and its components, M , are given by

$$\begin{aligned}\Delta J &= 0, \pm 1; \quad J = 0 \leftrightarrow J' = 0 \\ \Delta M &= 0, \pm 1 \\ \text{Parity change} & \qquad \qquad \qquad (2.1a)\end{aligned}$$

For states described by the L-S coupling scheme the orbital and the spin angular momentum quantum numbers change according to

$$\Delta L = 0, \pm 1 \quad \text{and} \quad \Delta S = 0 \quad . \quad (2.1b)$$

Radiative transitions between states that do not satisfy the selection rules generally have many orders of magnitude smaller transition probabilities. Such transitions in fluorescence spectra are historically called "forbidden lines".¹² When the forbidden lines constitute the only radiative decay channels an excited state may be considered metastable.

Since the selection rules for electric dipole transitions are derived from the angular momentum quantum numbers in the Russell-Saunders (L-S coupling) case, weakly allowed transitions basically result from a higher order electromagnetic interaction or a slight departure from the L-S coupling scheme. Thus, a metastable state may be classified according to the mechanism that enables radiative decay. For example, multipole electromagnetic interaction in the L-S coupling

scheme leads to metastable states that can decay without parity change by magnetic dipole, electric quadrupole, or two photon interactions. Except for the parity change and $\Delta L = \pm 1$ rules magnetic dipole transitions obey Eqs.(2.1a) and (2.1b). However, electric quadrupole transitions are governed by different restrictions on J :¹¹

$$\Delta J = 0, \pm 1, \pm 2 ; J + J' \geq 2 \quad (2.2)$$

In contrast the general selection rules for two photon transitions in the electric dipole approximation are given by

$$\begin{aligned} \Delta J &= 0, \pm 1, \pm 2 \\ \Delta M &= 0, \pm 1, \pm 2 \\ \text{No parity change} \end{aligned} \quad (2.3a)$$

Additional selection rules in the L-S coupling scheme are

$$\begin{aligned} \Delta L &= 0, \pm 1, \pm 2 \\ \text{and} \quad \Delta S &= 0 \end{aligned} \quad (2.3b)$$

In heavier elements a small departure from the L-S coupling due to spin-orbit interaction allows $\Delta S \neq 0$ inter-system (intercombination) transitions. The 3P_1 states of atoms with two outer electrons belong to this type of metastable states. Another type of departure from the L-S coupling scheme arises from the hyperfine interaction between the nuclear spin \vec{I} and the electronic angular momentum \vec{J} . Metastable states that decay due to hyperfine perturbation may violate the $J=0 \leftrightarrow J'=0$ selection rule of Eq.(2.1a)

since the selection rules in the (IJFM_F) coupling scheme are given by

$$\Delta F = 0, \pm 1; F = 0 \leftrightarrow F' = 0$$

and
$$\Delta M_F = 0, \pm 1. \quad (2.4)$$

The 2656 Å $^3P_0^o - ^1S_0$ transition in the odd isotopes of mercury atoms is an example of electric dipole decay via hyperfine interaction and spin-orbit interaction.¹³

2. Diatomic Molecules

The metastable states of diatomic molecules arise from the similar restrictions that prevent the radiative decay of metastable atoms. However, since molecules have more degrees of freedom, metastable states are characterized by a larger set of quantum numbers.¹⁴

In the Born-Oppenheimer approximation, the molecular states are specified by the electronic, vibrational, and rotational wave functions with the corresponding quantum numbers. The angular momentum of the electronic state is defined as the component of the angular momentum vector along the internuclear axis. The orbital component of \vec{L} is defined by $\Lambda = |M_L|$, and the spin component of \vec{S} is given by $\Sigma = M_S$. The total electronic angular momentum, Ω , is defined by the absolute value of the sum of Λ and Σ . This (Λ, S) coupling is similar to the Russell-Saunders case in that the interaction between the orbital and the spin components is

assumed to be small. In analogy with the atomic nomenclature the molecular states are denoted by $^{2S+1} \Lambda_{\Omega}$.

When spin-orbit interaction is large Λ and Σ are no longer well defined, and only Ω retains its meaning.¹⁴

Such angular momentum states are denoted only by Ω following Mulliken.¹⁵

The symmetry properties of a molecule leads to additional labels for each electronic wave function. For example, for the special case of the Σ states the electronic wave function is labeled Σ^+ if the phase does not change under the reflection of the coordinates of all electrons about a plane containing the internuclear axis; if a phase change occurs the electronic wave function is labeled Σ^- . Similarly, for electronic states described only by Ω the $\Omega = 0$ states have 0^+ and 0^- labels.

In homonuclear molecules the inversion symmetry of the electronic wave function about the midpoint of the molecule introduces even (gerade, g) and odd (ungerade, u) states independent of the angular momentum coupling scheme. If the phase of the electronic wave function changes under the inversion of the coordinates of all electrons the state is labeled odd; if the phase is invariant under the inversion operation the state is labeled even.

The general selection rules for electric dipole transitions between the electronic states of a diatomic molecule

are given by ¹⁴

$$\Delta J = 0, \pm 1$$

and $J = 0 \leftrightarrow J' = 0$ (2.5)

where J refers to the total angular momentum. For homonuclear molecules the additional symmetry selection rules are given by

$$g \leftrightarrow u, g \leftrightarrow g, u \leftrightarrow u \quad (2.6)$$

In the (Λ, S) coupling scheme the electric dipole selection rules are supplemented by ¹⁴

$$\Delta \Lambda = 0, \pm 1,$$

$$\Delta S = 0,$$

$$\Delta \Omega = 0, \pm 1,$$

$$\Omega = 0 \leftrightarrow \Omega' = 0 \text{ for } \Delta J = 0,$$

and $\Sigma^+ \leftrightarrow \Sigma^+, \Sigma^- \leftrightarrow \Sigma^-, \Sigma^+ \leftrightarrow \Sigma^-$. (2.7)

As in the atomic case metastable molecular states do not satisfy the selection rules given by Eqs.(2.5), (2.6), and (2.7) and may be classified according to the mechanisms that enable radiative decay. Metastable molecular states that decay by a higher order electromagnetic interaction within the (Λ, S) coupling scheme involve magnetic dipole and electric quadrupole transitions. The magnetic dipole transitions are governed by ¹⁴

$$\Delta J = 0, \pm 1,$$

$$J = 0 \leftrightarrow J' = 0,$$

and $g \leftrightarrow g, u \leftrightarrow u, g \leftrightarrow u$. (2.8)

where the symmetry selection rules apply to homonuclear molecules.

The electric quadrupole transitions have the same symmetry rules as Eq. (2.8), but different restrictions apply to the quantum number J:

$$\Delta J = 0, \pm 1, \pm 2$$

$$0 \leftrightarrow 0, \frac{1}{2} \leftrightarrow \frac{1}{2}, 1 \leftrightarrow 0 \quad (2.9)$$

When only Ω is defined, the selection rules for the allowed transitions are given by

$$\Delta \Omega = 0, \pm 1$$

and

$$0^+ \leftrightarrow 0^+, 0^- \leftrightarrow 0^-, 0^+ \leftrightarrow 0^- \quad (2.10)$$

The lowest excited states of diatomic mercury, Hg_2 , are examples of molecular states defined by Ω .¹² The 335 nm-band emission of Hg_2 ($1_u \rightarrow 0_g^+$) derives its transition moment from the atomic $\text{Hg}(^3P_1 \rightarrow ^1S_0)$ intercombination transition at 253.7 nm. Thus, a significant departure of the Hg atomic states from the L-S coupling scheme is reflected in the breakdown of the (Λ, S) coupling in the molecular states of Hg_2 .

C. ENERGY STORAGE LIFETIME AND CAPACITY

1. Introduction

Energy storage for high power laser applications requires high densities of metastable states. The lifetime of metastable states depends not only on the intrinsic radiative

decay but also on the externally induced loss mechanisms such as collisional deactivation and molecular formation. This section presents a brief summary of spontaneous radiative decay rate for various types of metastable states and examines population inversion density limitations imposed by stimulated one photon emission and non-radiative loss mechanisms. Scaling properties are also discussed.

2. Spontaneous Radiative Decay

From the description of the kinds of metastable states in Section B the basic radiative decay mechanisms are either weakly allowed electric dipole transitions due to angular momentum perturbation or higher order electromagnetic interactions involving one and two photon transitions. The two cases are distinguished by an important selection rule on parity as illustrated in Fig. 1. In Fig. 1a the spontaneous electric dipole transition rate from state $|\gamma J\rangle$ to $|\gamma' J'\rangle$ is given by ¹⁶

$$A(\gamma J \rightarrow \gamma' J')_{E1} = \frac{1}{2J+1} \left(\frac{4\omega_0^3}{3\hbar c^3} \right) \left| \langle \gamma J || \vec{\mu}_E || \gamma' J' \rangle \right|^2 \quad (2.11)$$

and

$$\vec{\mu}_E = -e \sum_i \vec{r}_i \quad (2.12)$$

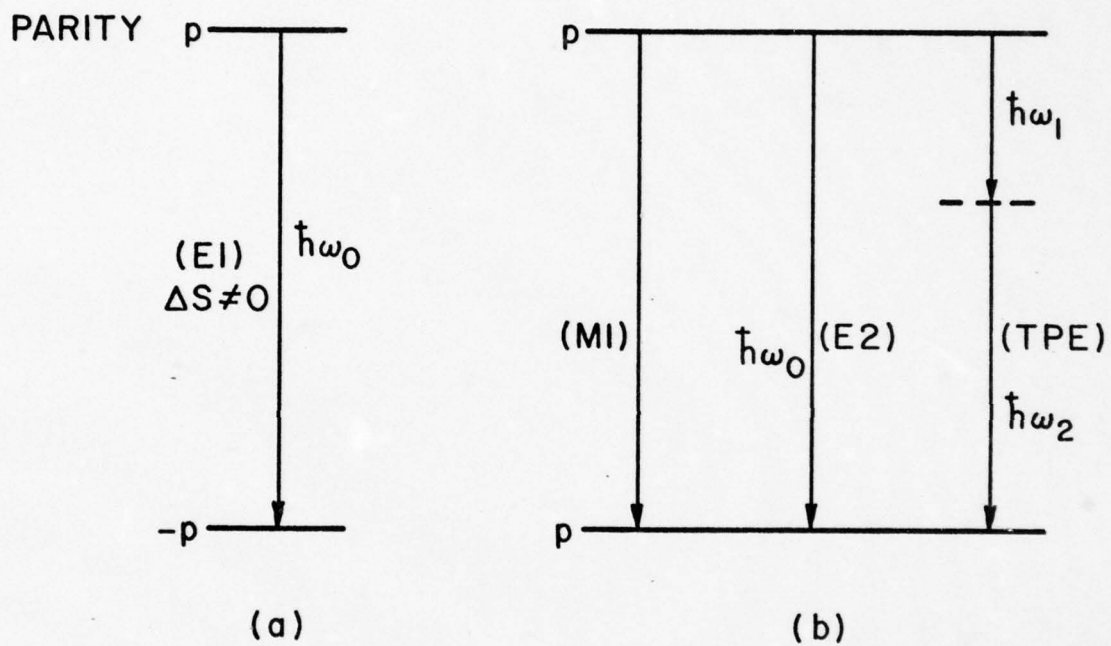


Fig. 1 -- Radiative decay of metastable states:
 (a) Intercombination electric dipole (E1) transition with a change in parity;
 (b) magnetic dipole (M1), electric quadrupole (E2), and two-photon emission (TPE) transitions with no parity change.

where ω_0 is the transition frequency in radians-sec⁻¹. The reduced matrix element of $\vec{\mu}_E$ determines the strength of the transition. For intercombination transitions the reduced matrix element is a small fraction of that of the corresponding strongly allowed transition as determined from the amount of admixture of (SLJM_J) basis functions. The ratio of transition rates for an intercombination line and the corresponding allowed transition typically ranges from about 2×10^{-2} for mercury to 6×10^{-7} for magnesium.¹² Since allowed transition rates are of the order of 10^8 to 10^9 sec⁻¹, the intercombination decay rates are approximately 10^7 sec⁻¹ for Hg and 2×10^2 sec⁻¹ for Mg. The large variation in the intercombination transition rate is due to a larger spin-orbit interaction and the increasing departure from the L-S coupling in the heavier elements.

Hyperfine interaction in atoms with non-zero nuclear spin has been suggested as a possible mechanism for certain forbidden transitions.^{13,17} However, the effect is generally very small, and only in certain cases calculations yield transition rates approaching those of spin-orbit induced intercombination transitions.

In case (b) of Fig. 1 higher order electromagnetic interactions are responsible for radiative decay. The important one photon multipole transitions are magnetic dipole (M1) and electric quadrupole (E2) interactions. The

transition rate formulas are given as follows:¹⁶

$$A(\gamma J \rightarrow \gamma' J')_{M1} = \frac{1}{2J+1} \left(\frac{4 \omega_0^3}{3 \hbar c^3} \right) \left| \langle \gamma J \| \vec{\mu}_M \| \gamma' J' \rangle \right|^2 \quad (2.13)$$

and

$$\vec{\mu}_M = - \mu_B (\vec{L} + 2\vec{S}) / \hbar \quad (2.14)$$

where μ_B is the Bohr magneton.

$$A(\gamma J \rightarrow \gamma' J')_{E2} = \frac{1}{2J+1} \left(\frac{4 \omega_0^5}{15 \hbar c^5} \right) \sum_{q,m,m'} \left| \langle \gamma J m | Q_q | \gamma' J' m' \rangle \right|^2 \quad (2.15)$$

where the q -th component of the electric quadrupole operator, Q , is given in terms of the spherical harmonics,

$$Q_q = -e \sqrt{\frac{4\pi}{5}} \sum_i r_i^2 Y_{2q}(\theta_i, \varphi_i) \quad (2.16)$$

A comparison of Eqs.(2.11), (2.13), and (2.15) shows that the relative transition rates are roughly given by

$$A_{E1} : A_{M1} : A_{E2} = 1 : (\mu_B / ea_0)^2 : (a_0 / \lambda)^2 \quad (2.17)$$

where a_0 is the Bohr radius, and λ is the wavelength. Thus, the relative lifetimes are about $10^{-8} : 10^{-3} : 1$ sec.

Metastable states that cannot radiate by one photon multipole interaction may decay by a simultaneous emission of two photons with energies $\hbar\omega_1$ and $\hbar\omega_2$. The restriction on the photon energies is that the sum must be equal to the transition energy as indicated in Fig. 1b. Thus, spontaneous emission is characterized by a continuum spectra from near-zero frequency to ω_0 . The mechanism for this radiative process was first analyzed by Goeppert-Mayer¹⁸ as a second-order perturbation on the transition rate. In the electric dipole approximation, $\exp(ikr) \approx 1$, the two-photon emission rate from $|b\rangle$ to $|a\rangle$ is given by¹⁶

$$W_{ba}^{(2)} = \frac{\pi g_L}{2 \epsilon_0^2} \frac{\omega_1 \omega_2 (n_1 + 1)(n_2 + 1)}{(L^3)^2 (2J_b + 1)} \sum_{M_b} \sum_{M_a} |\alpha_{1,2}|^2 \quad (2.18a)$$

where

$$\alpha_{1,2} = \sum_k \left[\frac{(\nu_2^\dagger)_{ak} (\nu_1^\dagger)_{kb}}{\hbar(\omega_{kb} + \omega_1)} + \frac{(\nu_1^\dagger)_{ak} (\nu_2^\dagger)_{kb}}{\hbar(\omega_{kb} + \omega_2)} \right] \quad (2.18b)$$

and

$$g_L = \delta(\omega_0 - \omega_1 - \omega_2) \quad (2.18c)$$

In Eq.(2.18a) n_1 and n_2 are the photon occupation numbers for ω_1 and ω_2 , respectively, and L^3 is the quantization

volume. The matrix elements in Eq.(2.18b) are the usual electric dipole matrix elements of $\vec{\mu}_E \cdot \hat{\epsilon}_\ell^* \equiv \mu_\ell^\dagger$, where $\hat{\epsilon}_\ell$ is the polarization of the photon at ω_ℓ .

The spontaneous two-photon emission rate, A^{TPE} , is obtained by multiplying $W_{ba}^{(2)}(n_1=n_2=0)$ by the density of modes, $\rho(\omega)$, for ω_1 and ω_2 and integrating over all frequencies and angles.

$$A_{ba}^{\text{TPE}} = \int W_{ba}^{(2)} \rho(\omega_1) \rho(\omega_2) d\omega_1 d\omega_2 d\Omega_1 d\Omega_2 \quad (2.19a)$$

where

$$\rho(\omega_\ell) = 2 \left(\frac{L}{2\pi} \right)^3 \frac{\omega_\ell^2}{c^2} \quad (2.19b)$$

Breit and Teller¹⁹ evaluated the integral and the summation in Eq.(2.18b) for the metastable 2S states of hydrogen and obtained a rate of between 6.5 and 8.7 sec^{-1} . Shapiro and Breit improved and extended the calculation to the 2S states of hydrogenic atoms.²⁰ For small values of the nuclear proton number, Z, they obtained $A^{\text{TPE}} = (8.226 \pm 0.001) Z^6 \text{sec}^{-1}$. Dalgarno²¹ treated the metastable 2^1S_0 state of helium and obtained $A^{\text{TPE}} = 51.3 \text{sec}^{-1}$ and the two-photon emission spectral distribution.

Spontaneous two-photon emission has been detected in $\text{He}^+(2^2S)$ by Lipeles et. al.,²² and the two-photon emission spectrum of $\text{Ne IX}(2^1S)$ has been observed by Elton et. al.²³

If $n_1 \gg 1$ or $n_2 \gg 1$ the two-photon transition rate is increased considerably over the spontaneous rate. This condition is referred to as the enhanced two-photon emission. Such effect has been observed in the potassium $6^2S - 4^2S$ transition by Yatsiv, Rokni, and Barak.²⁴ Enhanced two-photon emission in the mercury $6^3P_0 - 6^1S_0$ transition has been reported by Fornaca et. al.²⁵ In both cases a high power laser provided the source of intense radiation for creating $n_1 \gg 1$.

If $n_1 \gg 1$ and $n_2 \gg 1$, stimulated two-photon transition rate may become comparable to that of strongly allowed transitions. For a non-inverted medium this condition leads to two-photon absorption (TPA) from $|a\rangle$ to $|b\rangle$. However, in an inverted metastable system $n_1 \gg 1$ and $n_2 \gg 1$ lead to stimulated two-photon emission with optical gain at both ω_1 and ω_2 . The optical gain at the TPE frequencies is the basis of two photon amplifiers discussed in Chapter III.

3. Population Inversion and Superfluorescence

An inverted population in a metastable state is one of the requirements of energy storage for lasers and amplifier systems. Pumping mechanisms for creating population inversion in metastable states vary from one system to another, but all systems have common requirements of a long storage lifetime relative to optical extraction pulse length and a large energy storage capacity. This section considers the

effect of stimulated emission on the energy storage capacity of an inverted metastable system. The actual pumping mechanisms are described in Chapter IV for specific systems. Here, a population inversion is assumed for a two-level metastable system which has a net optical gain at the transition frequency.

In an inverted medium spontaneously emitted radiation may be amplified by stimulated emission according to the following equation which describes the intensity growth in the unsaturated case.²⁶

$$\frac{dI(z)}{dz} = \gamma I(z) - a I(z) + \eta \gamma \quad (2.20)$$

where γ is the gain per unit length, and a is the loss per unit length. The parameter η is a geometry dependent constant which describes the intensity contribution from spontaneous emission. Since the unsaturated gain is assumed to be constant for a uniform gain medium, direct integration of Eq.(2.20) yields the solution for $I(z)$.

$$I(z) = I(0) e^{(\gamma - a)z} + \frac{\eta \gamma}{(\gamma - a)} \left[e^{(\gamma - a)z} - 1 \right] \quad (2.21)$$

where $I(0)$ is the input signal intensity at $z = 0$.

Since $I(0) = 0$ for amplification of spontaneous emission, Eq. (2.21) reduces to

$$I(z) = \frac{\eta \gamma}{(\gamma - a)} \left[e^{(\gamma - a)z} - 1 \right] \quad (2.22)$$

This intensity growth is called superfluorescence.

The parameter η for a gain medium of length ℓ and a cross-sectional area of w^2 may be calculated as follows. In a cross-sectional slab of thickness δZ spontaneously emitted power, δP , due to δN number of excited species is given by

$$\begin{aligned} \delta P &= \delta N h\nu A \\ &= \delta N h\nu / t_{\text{spont}} \end{aligned} \quad (2.23)$$

where t_{spont} is the spontaneous emission lifetime. Since δN is equal to the excited state density, n^* , times $w^2 \delta Z$, the intensity of radiation through the slab is

$$\begin{aligned} \delta I &= \delta P / w^2 \\ &= n^* h\nu A \delta Z \end{aligned} \quad (2.24)$$

A fraction of the emitted radiation that can be amplified by the full length of the gain medium is $(\delta\Omega/4\pi)$, where $\delta\Omega$ is the solid angle which is approximately equal to $(w/\ell)^2$.

Therefore, the intensity growth due to spontaneous emission in one direction is given by

$$\eta \gamma \approx \frac{1}{2} \left(\frac{w}{\ell} \right)^2 \frac{n^* h \nu A}{4 \pi} \quad (2.25)$$

Hence,

$$\eta \approx \frac{1}{8 \pi} \left(\frac{w}{\ell} \right)^2 \frac{n^* h \nu A}{\gamma} \quad (2.26)$$

The intensity growth solution in Eq.(2.22) is valid for intensities less than the saturation intensity, I_{sat} , where I_{sat} is defined as the intensity at which the depletion of population inversion due to stimulated transitions reduces the gain to one half of the unsaturated value. The expression for I_{sat} is given by

$$I_{\text{sat}} = \frac{h \nu}{2 \sigma \tau} \quad (2.27)$$

where σ is the stimulated emission cross-section, and τ is the upper level lifetime.

If amplified spontaneous emission intensity reaches I_{sat} , the gain medium can radiate most of the stored energy without external control. This undesirable behavior is present in many high power gas and solid-state laser systems

and limits a controlled mode of operation to a certain inversion density and dimensions.

The inversion density at which superfluorescence reaches saturation can be estimated by equating Eq. (2.22) and Eq. (2.27). Using η from Eq. (2.26) the calculation yields

$$\left(\frac{n^* \sigma}{\gamma - a} \right) \left[\exp [(\gamma - a) \ell] - 1 \right] \approx 4 \pi \left(\frac{\ell}{w} \right)^2 \frac{t_{\text{spont}}}{\tau} \quad (2.28)$$

The unsaturated gain γ , may be expressed as a product of σ and the inversion density Δn , and thus for a relatively lossless ($a \ll \gamma$) gain medium with $\Delta n \lesssim n^*$ the above expression simplifies to

$$\exp(\sigma \Delta n \ell) \approx 4 \pi \left(\frac{\ell}{w} \right)^2 \frac{t_{\text{spont}}}{\tau} \quad (2.29)$$

Eq. (2.29) assumes that $\exp(\gamma \ell)$ is much larger than 1. This is a good approximation since $\gamma \ell$ product is typically 10 to 20. If Δn is significantly smaller than n^* , the right hand side of Eq. (2.29) must be multiplied by a factor $(\Delta n/n^*)$.

A typical gain medium consisting of metastable states might have the following dimensions and lifetimes:

$$\begin{aligned} \ell & \sim 100 \text{ cm} \\ w & \sim 1 \text{ cm} \\ t_{\text{spont}} & \sim 10^{-3} \text{ sec} \\ \tau & \sim 10^{-6} \text{ sec} \end{aligned} \tag{2.30}$$

These values yield

$$\exp(\sigma \Delta n \ell) \sim e^{20} \tag{2.31}$$

or

$$\sigma \Delta n \ell \approx 20 \tag{2.31b}$$

which is a commonly used superfluorescence saturation condition. Because superfluorescence gain is exponential in $\sigma \Delta n \ell$, Eq. (2.31b) is not sensitive to variation in the assumed parameters. Furthermore, Eq. (2.31b) can be modified slightly to describe the lossy case ($a \lesssim \gamma$). The result is

$$\sigma \Delta n \rho \ell \approx \ln(\rho) \tag{2.32}$$

where

$$\rho \equiv 1 - \frac{\alpha}{\sigma \Delta n} > 0 \quad (2.33)$$

Thus, for example, if $\alpha/\sigma \Delta n = 0.9$, $\sigma \Delta n l$ becomes 200. This indicates that the superfluorescence saturation condition can be increased substantially by reducing the net gain.

In order to evaluate the inversion density limit imposed by superfluorescence saturation an estimate for σ is essential. The numerical value of σ may be obtained experimentally or calculated from a formula given by²⁶

$$\sigma(\nu) = \frac{A c^2}{8\pi\nu^2} g(\nu) \quad (2.34)$$

For a homogeneously broadened transition the spectral line-shape factor, $g(\nu)$, is a normalized Lorentzian function defined by

$$g(\nu) = \left(\frac{2}{\pi}\right) \frac{\Delta\nu}{4(\nu - \nu_0)^2 + (\Delta\nu)^2} \quad (2.36)$$

where the peak value at $\nu = \nu_0$ is $(2/\pi)$ times the reciprocal of the spectral width at the half maximum points, $\Delta\nu$. Using Eq. (2.34) and Eq. (2.35) the peak value of σ becomes

$$\sigma_0 = \frac{A c^2}{4\pi^2 \nu_0^2 \Delta\nu} \quad (2.36)$$

The stimulated emission cross-section for metastable states can now be calculated if A and $\Delta\nu$ are available. Using $\nu_0 = 6 \times 10^{14}$ Hz and $\Delta\nu = 3 \times 10^9$ Hz rough estimates of σ for two different types of metastable states in Fig. 1a and 1b yield the following results. For case (a), A ranges from 10^7 to 10^2 sec^{-1} , which yields a range of σ from 10^{-13} to 10^{-18} cm^2 . For case (b) A is on the order of 10^3 sec^{-1} for (M1) emission and 1 sec^{-1} for (E2) emission and the corresponding values of σ are 10^{-17} and 10^{-20} cm^2 .

Atomic iodine is an example of the case (b), and the $^2P_{1/2} - ^2P_{3/2}$ magnetic dipole emission cross-section has a maximum value of $1.78 \times 10^{-18} \text{ cm}^2$.¹⁰ Using Eq.(2.31b) the superfluorescence condition for a 1 meter gain medium gives Δn on the order of 10^{17} cm^{-3} which is a typically observed inversion density achieved in a flashlamp pumped photo-dissociation iodine laser.¹⁰ In practice superfluorescence

can be suppressed by an order of magnitude by reducing the cross-section with line broadening.²⁷

An example of a metastable system belonging to case (a) of Fig. 1 is the $1_u - 0_g^+$ bound-continuum transition of Hg_2 . Recent experiments on the Hg_2 metastable system showed that $\sigma_0 \Delta n$ is $2.5 \pm 1.3 \times 10^{-6} \text{ cm}^{-1}$ at 335 nm with a total inversion density of $6 \pm 3 \times 10^{14} \text{ cm}^{-3}$. The data suggest a superfluorescence inversion density on the order of 10^{19} cm^{-3} , but stimulated emission appears to be prevented by a competing transition to the upper states of the molecule.²

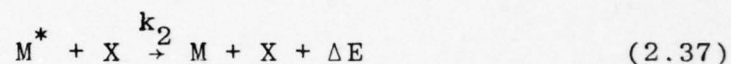
In summary, superfluorescence depletion of population inversion suggests a limit on the metastable state inversion density at around 10^{18} to 10^{19} cm^{-3} for a 1 meter gain medium. This inversion density corresponds to an energy storage capacity on the order of 1 kilojoule per liter in an excited vapor of metastable species.

4. Non-Radiative Loss Mechanisms

Collisional effects on the metastable lifetime become significant at vapor densities of greater than 10^{16} cm^{-3} which is the lower limit of energy storage density considered for laser applications. Reactions involving two- and three-body collisions can significantly reduce the storage duration and place a practical limit on the energy capacity. This section examines collisional deactivation mechanisms and

rates from experimental data in order to derive realistic energy storage characteristics. This includes several key findings from a recent experimental analysis of Hg_2 metastable states, which is presented in Appendix A.

The most common type of collisional deactivation is a two-body reaction involving an excited metastable species M^* and a "quenching" agent, X, which may be an atom or a molecule. The reaction is described by



The parameter k_2 is the two-body reaction rate constant which determines the decay rate of M^* according to

$$\frac{d}{dt} [M^*] = -k_2 [M^*] [X] \quad (2.38)$$

The rate constant can be expressed as a product of the effective quenching cross-section, σ_Q^2 , and the radiative collision speed.²⁸

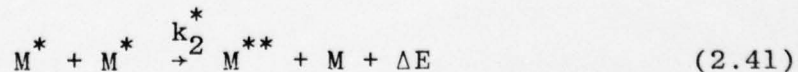
$$k_2 = \sigma_Q^2 \left[\frac{8\pi RT}{m} \right]^{\frac{1}{2}}$$

where R is the gas constant ($8.3143 \times 10^7 \text{ erg}\cdot\text{K}^{-1}\cdot\text{mole}^{-1}$), T is the absolute temperature, and m is the reduced mass of the collision partners given in units of $\text{grams}\cdot\text{mole}^{-1}$.

$$m = \frac{m_M m_X}{(m_M + m_X)} \quad (2.40)$$

At $T = 300^\circ\text{K}$ typical values of collision speed range from $10^4 \text{ cm}\cdot\text{sec}^{-1}$ for heavy diatomic molecules to $10^5 \text{ cm}\cdot\text{sec}^{-1}$ for light atoms and molecules. Since σ_Q^2 is typically on the order of molecular dimensions, the rate constant, k_2 is on the order of 10^{-12} to $10^{-10} \text{ cm}^3\cdot\text{sec}^{-1}$. Experimental values of quenching cross-sections have been measured for many atomic metastable species in photochemical reactions. In particular quenching of the metastable $\text{Hg}(^3\text{P}_{0,1})$ atoms by various collision partners has been investigated extensively.^{28,29} Some of the representative measured cross-sections for $\text{Hg}(^3\text{P}_1)$ are 6 \AA^2 for H_2 , 0.19 \AA^2 for N_2 , and $\sim 40 \text{ \AA}^2$ for unsaturated hydrocarbons.

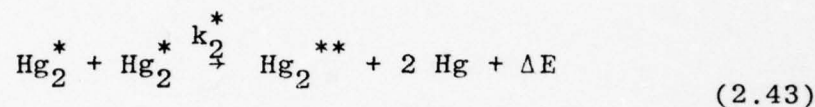
At high densities of excited metastable species two-body collisional deactivation can occur without any foreign quenching agent. The process involves a reaction of two metastable species which yields a highly excited state and a ground state according to



and

$$\frac{d}{dt} [M^*] = - k_2^* [M^*]^2 \quad (2.42)$$

Experiments with optically pumped metastable Hg_2 states showed that the above mechanism is the dominant decay process at Hg_2^* densities greater than 10^{15} cm^{-3} . The reaction is assumed to be

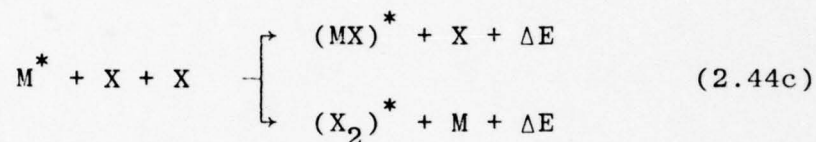
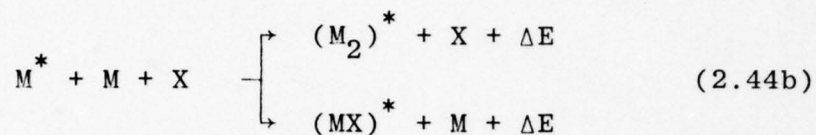


The measured rate constant was $k_2^* \approx (2 \pm 1) \times 10^{-10} \text{ cm}^3\text{-sec}^{-1}$ with the corresponding cross-section of $\sigma^2 \approx (2.5 \pm 1.3) \times 10^{-15} \text{ cm}^2$ or $25 \pm 13 \text{ \AA}^2$. This value is comparable to the mutual collisional deactivation rate for atomic Hg metastable states.³⁰

The reaction rate, k_2^* , can be much smaller than the gas kinetic rate if the reaction in Eq.(2.41) is endothermic. This may occur for atomic metastable states that have less than half the energy of the next higher excited state. The metastable $^2P_{1/2}$ state of atomic iodine is an example of this case, and the mutual two-body collisional deactivation rate can be expected to be smaller than the gas kinetic rate.

At densities greater than 10^{17} cm^{-3} three-body collisions contribute significantly to metastable decay rate. The primary mechanism is molecular formation involving

metastable species and collision partners in various reactions given by



The corresponding rate equations are given by

$$\frac{d}{dt}[M^*] = -k_3^a [M]^2 [M^*] \quad (2.45a)$$

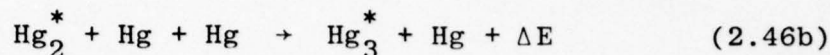
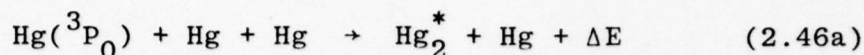
$$\frac{d}{dt}[M^*] = -k_3^b [M][X][M^*] \quad (2.45b)$$

$$\frac{d}{dt}[M^*] = -k_3^c [X]^2 [M^*] \quad (2.45c)$$

where k_3 is the rate constant which is typically on the order of 10^{-34} to 10^{-31} $\text{cm}^6\text{-sec}^{-1}$.

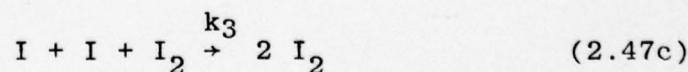
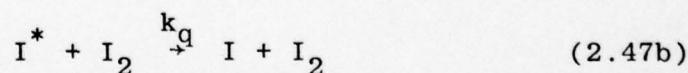
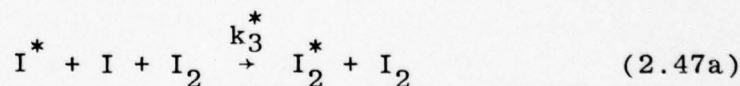
The metastable states of atomic and molecular mercury provide examples of three-body collisions leading to molecular

formation in the following reactions.^{31,32}



The dimer formation rate constant has been measured to be $k_3 \approx 1.55 \times 10^{-31} \text{ cm}^6\text{-sec}^{-1}$.³¹ At atmospheric densities of Hg ($\sim 10^{19} \text{ cm}^{-3}$) the three-body collisional decay rate of Hg(³P₀) is on the order of 10^7 sec^{-1} which is some five orders of magnitude faster than the measured decay rate at low pressures.

The metastable ²P_{1/2} iodine atoms also form molecules by three-body collisions with various partners. Interest in the atomic iodine laser has led to extensive study of the reactions and rate measurements. Some of the inherent reactions are given by¹⁰



The measured rate constants are $k_3^* = 4.3 \times 10^{-32} \text{ cm}^6\text{-sec}^{-1}$ and $k_q = 1.3 \times 10^{-14} \times \exp(1650/T) \text{ cm}^3\text{-sec}^{-1}$ for the excited atoms.

For the ground state atoms the molecular recombination rate constant is given by $k_3 = 1.1 \times 10^{-15} \times T^{-5.9} \text{ cm}^6\text{-sec}^{-1}$.

At $T = 300 \text{ K}$, the bimolecular quenching rate constant, k_q , is $3.2 \times 10^{-12} \text{ cm}^3\text{-sec}^{-1}$, and the ground state recombination rate constant is given by $k_3 = 2.7 \times 10^{-30} \text{ cm}^6\text{-sec}^{-1}$. These rate constants suggest that the metastable lifetime becomes sub-microsecond at vapor densities on the order of 10^{18} cm^{-3} .

In summary collisional deactivation of metastable states becomes a dominant loss mechanism at vapor densities of interest in high power laser applications. In particular mutual two-body collisional deactivation of excited metastable species, as illustrated by the Hg_2 system, suggests a limiting density for a practical storage duration. Since storage times of 100 nanosecond or longer are desirable, the measured bimolecular rate constant suggests a maximum metastable state density on the order of 10^{17} cm^{-3} . In terms of photon energy in the visible spectrum this density is equivalent to an optical energy storage capacity of about 50 joules per liter. This storage limitation is likely to be present in many atomic and molecular systems as an inherent property associated with the mutual two-body quenching. Some atomic systems, such as the metastable iodine atoms, are not density limited by mutual metastable state deactivation. For these systems molecular formation and two-body quenching due to the formed molecules ultimately limit the storage lifetime and capacity.

5. Scaling

The results of Sections C.3 and C.4 suggest that energy storage can be increased by increasing the volume of the inverted medium. However, to prevent the depletion of population inversion the single pass net gain must be reduced in order to suppress superfluorescence. In practice with CO₂ lasers distributed losses due to saturable absorber provide a net attenuation for small signal levels.³³ At high input intensities absorption saturates, and the medium attains a net gain for large signal amplification and energy extraction.

Alternatively, the single pass loss can be made greater than the gain at all signal levels and prevent superfluorescence altogether. This eliminates stimulated one photon emission, but leaves a possibility for stimulated two-photon emission at two frequencies for which the medium is transparent. One possible system might consist of an inverted metastable system in which two-photon emission is allowed followed by a non-inverted two-level system with the same energy difference but coupled only by an electric dipole transition. Since two-photon transitions are not allowed for the non-inverted species, stimulated emission may be amplified through the combined system. This unique property of two photon transitions is an attractive feature for a large scale system and a motivation for investigating theoretical and experimental aspects of two-photon lasers.

In summary, population inversion of metastable states in a vapor system provides a potential optical energy storage medium for high power laser applications. The energy storage lifetime and capacity are limited by superfluorescence inversion depletion and non-radiative loss mechanisms. Both theoretical and experimental studies on the metastable decay properties indicate a maximum realistic inversion density of 10^{17} to 10^{18} cm^{-3} for vapor systems in general. Scaling considerations for a fixed inversion density show that superfluorescence inversion depletion limits the dimensions of a one-photon gain medium. However, stimulated two-photon emission can occur in an inverted medium which has no net one-photon gain. By eliminating one-photon superfluorescence, energy storage scaling can be extended to two-photon extraction schemes which are discussed in Chapter III.

CHAPTER III

TWO PHOTON ENERGY EXTRACTION

A. INTRODUCTION

A recent demand for high power laser systems in laser fusion studies and photochemical applications has generated interest in laser amplifiers with large energy storage capacities.¹ Concurrently nonlinear optical extraction of stored energy has received attention as a method of generating high energy laser outputs.^{6,34} In particular stimulated two photon transition in an inverted medium has been suggested as a potential scheme for not only amplifying an input signal but also tailoring the pulse shape by the nonlinear gain.^{3-6,34,35}

The concept of a two photon laser differs from an ordinary laser medium in two respects. First, the two photon amplification occurs at two frequencies that do not coincide with the energy difference between the initial and the final states of the transition. The only restriction is that the photon energies and the transition energy are conserved. Second, the transition rates of two photon processes depend on the product of the field intensities in contrast to a linear relationship in one photon transitions. Figure 2

shows two photon processes between two levels which are separated by an energy $\hbar\omega_0$. Figure 2b shows two-photon emission (TPE) at $\hbar\omega_1$ and $\hbar\omega_2$ such that $\hbar\omega_1 + \hbar\omega_2 = \hbar\omega_0$ holds. The presence of radiation at ω_1 can also generate Raman scattering at ω_3 . In an inverted medium the transition energy and the incident photon energy sum to yield stimulated output at $\hbar\omega_3$. This process is the anti-Stokes Raman scattering (ASRS) shown in Fig. 2c. Since both TPE and ASRS involve optical energy extraction at a frequency distinct from the natural transition frequencies, the two photon processes are also interesting physical effects in themselves.

This chapter describes some of the theoretical aspects of two photon amplification and energy extraction in an inverted system. The following sections give a brief review of the theory and discuss the energy extraction properties of an ideal two photon gain medium including saturation effects.

B. THEORY

In the semiclassical perturbation theory two photon processes are described by nonlinear induced polarization of the medium and Maxwell's field equations which are driven by the polarizations. The nonlinear polarization is generated by the third-order susceptibility which can be derived

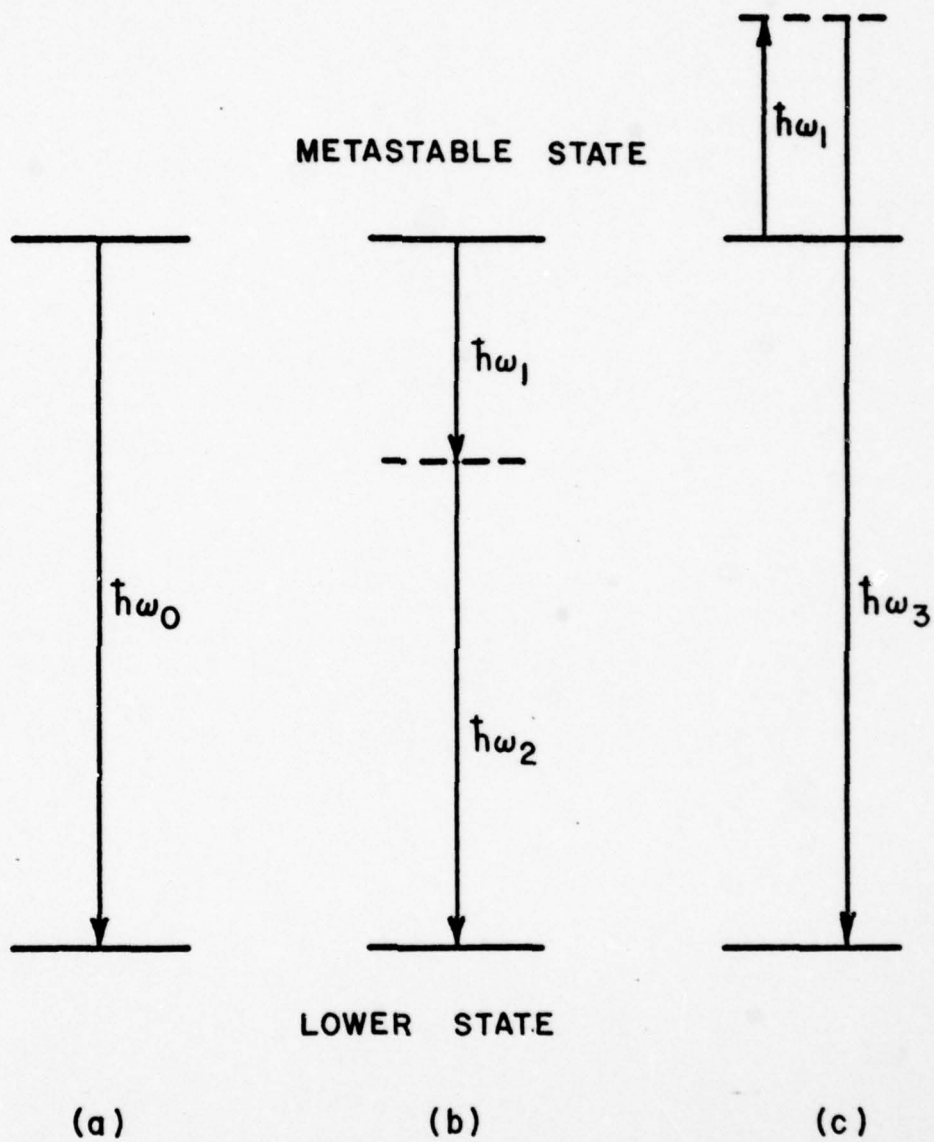


Fig. 2 -- One and two photon energy extraction schemes:
 (a) Ordinary one photon laser transition at ω_0 ;
 (b) stimulated TPE amplification at ω_1 and ω_2 ;
 (c) stimulated ASRS amplification at ω_3 .

from density matrix calculations using an electric dipole interaction hamiltonian. However, since two photon transitions involve actual transfer of population from an inverted level to a lower level, saturation of the medium must be taken into account. Accordingly the calculation must include equations for the population difference and the oscillation of the two-level system at the two photon resonance frequency.

This section briefly describes the derivation of the equations of motion for the two photon processes. The derivation closely follows the analysis of Carman,⁶ and considers the interaction of four electric fields in a two photon gain medium. Figure 3 shows a schematic two-level system with TPE and ASRS transitions considered here. The two levels are specified by the angular momentum quantum numbers, J and M. The magnetic substates are assumed to be degenerate. The intermediate states are assumed to be non-resonant so that real transitions cannot occur.

The electric fields consist of an input laser signal at ω_1 , TPE signal at ω_2 , ASRS signal at ω_3 , and another ASRS signal at ω_4 due to ω_2 . Higher order Raman transitions and other coherent wave mixing processes may occur, but they are neglected here for simplicity. The four fields are defined by

$$\vec{E}_\ell(\vec{r}, t) = \frac{1}{2} \hat{e}_\ell E_\ell \exp(ik_\ell z - i\omega_\ell t) + \text{C.C.} \quad (3.1)$$

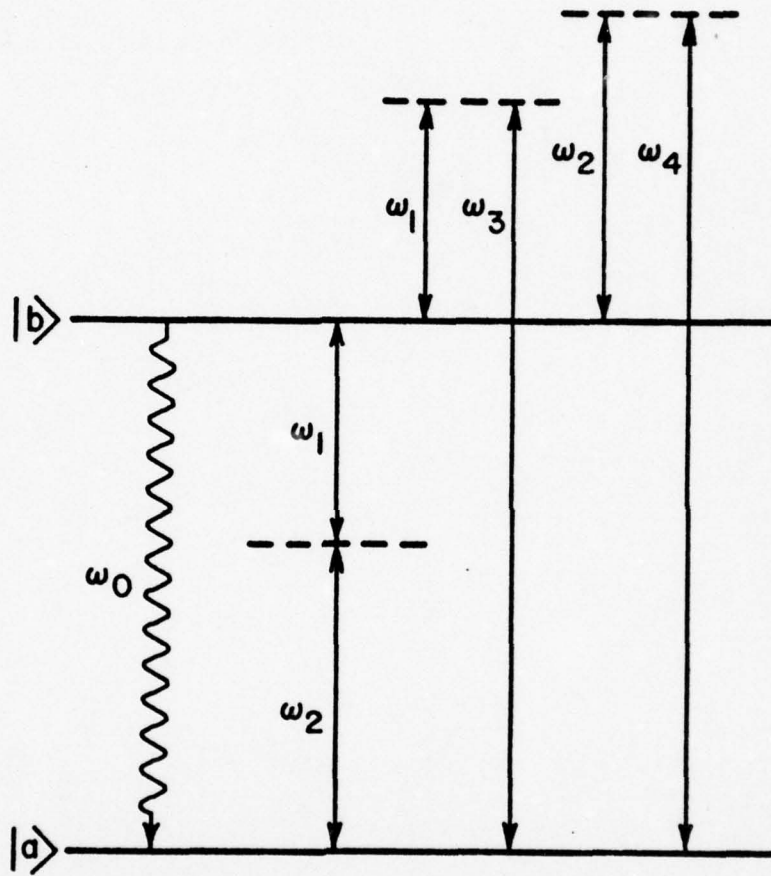


Fig. 3 -- Two-level system for two photon extraction analysis.

The oscillation of the two-level system is given by

$$Q(\vec{r}, t) = \frac{1}{2} q \exp(ik_0 z - i\omega_0 t) + \text{C.C.} \quad (3.2)$$

where q is the oscillation amplitude. The field frequencies and the wave vectors satisfy the following relations:

$$\omega_1 + \omega_2 = \omega_0, \quad k_1 + k_2 - k_0 \equiv \Delta k_{12} \quad (3.3a)$$

$$\omega_3 - \omega_1 = \omega_0, \quad k_3 - k_1 - k_0 \equiv \Delta k_{31} \quad (3.3b)$$

$$\omega_4 - \omega_2 = \omega_0, \quad k_4 - k_2 - k_0 \equiv \Delta k_{42} \quad (3.3c)$$

and

$$k_\ell = \frac{n_\ell \omega_\ell}{c} \quad (3.3d)$$

where n_ℓ is the refractive index of the medium at ω_ℓ .

The relationship between the electric fields and the two-level oscillation is established by a differential equation for Q .³⁶

$$\frac{\partial^2 Q}{\partial t^2} + \frac{2}{T_2} \frac{\partial Q}{\partial t} + \frac{1}{T_2^2} Q = - \frac{1}{\hbar^2} \langle [[Q_{\text{op}}, \mathcal{H}], \mathcal{H}] \rangle \quad (3.4)$$

where T_2 is the usual dephasing or transverse relaxation time, and \mathcal{H} is the hamiltonian containing an electric dipole interaction term, V , as given by

$$\mathcal{H} = \mathcal{H}_0 + V, \quad V = - \vec{\mu} \cdot \vec{E} \quad (3.5)$$

Evaluating the right-hand side of Eq.(3.4) using Eq.(3.2) and the slowly varying amplitude approximation yields

$$\frac{\partial q}{\partial t} + \frac{1}{T_2} q \approx -\left(\frac{i u}{4 \hbar}\right) \left[\phi \exp(ik_0 z - i\omega_0 t) + C.C. \right] \quad (3.6)$$

where u represents the relative population difference between the inverted state $|b\rangle$ and the lower state $|a\rangle$. The term ϕ contains the interaction of the electric fields and the two-level system and is given by

$$\phi = \alpha_{1,2}^* E_1 E_2 e^{i\Delta k_{12}z} + \alpha_{1,3}^* E_1 E_3 e^{i\Delta k_{31}z} + \alpha_{2,4}^* E_2 E_4 e^{i\Delta k_{42}z} \quad (3.7)$$

where α 's are the polarizability tensor components defined by the following expressions:

$$\alpha_{1,2} = \sum_k \left[\frac{(\mu_2^\dagger)_{ak} (\mu_1^\dagger)_{kb}}{\hbar(\omega_{kb} + \omega_1)} + \frac{(\mu_1^\dagger)_{ak} (\mu_2^\dagger)_{kb}}{\hbar(\omega_{kb} + \omega_2)} \right] \quad (3.8a)$$

$$\alpha_{1,3} = \sum_k \left[\frac{(\mu_3^\dagger)_{ak} (\mu_1)_{kb}}{\hbar(\omega_{kb} - \omega_1)} + \frac{(\mu_1)_{ak} (\mu_3^\dagger)_{kb}}{\hbar(\omega_{kb} + \omega_3)} \right] \quad (3.8b)$$

$$\alpha_{2,4} = \sum_k \left[\frac{(\mu_4^\dagger)_{ak} (\mu_2)_{kb}}{\hbar(\omega_{kb} - \omega_2)} + \frac{(\mu_2)_{ak} (\mu_4^\dagger)_{kb}}{\hbar(\omega_{kb} + \omega_4)} \right] \quad (3.8c)$$

where the summation over k denotes a sum over J_k and M_k and other intermediate state quantum numbers. The matrix

elements in Eqs.(3.8a), (3.8b), and (3.8c) are the usual dipole matrix elements of $\vec{\mu} \cdot \hat{\epsilon}_\ell \equiv \mu_\ell$ and $\vec{\mu} \cdot \hat{\epsilon}_\ell^* \equiv \mu_\ell^\dagger$.

The time dependence of the population difference is described by ³⁶

$$\frac{\partial u}{\partial t} + \frac{1}{T_1}(u - u_e) = \left(\frac{1}{i\hbar}\right) \langle [u_{op}, \mathcal{H}] \rangle \quad (3.9)$$

where $(1/T_1)$ is the longitudinal relaxation rate with which the population inversion returns to its equilibrium value, u_e , in the absence of the applied fields. Evaluation of the right-hand side of Eq.(3.9) gives

$$\frac{\partial u}{\partial t} + \frac{1}{T_1}(u - u_e) = \left(\frac{i}{2\hbar}\right) (q^* \phi - q \phi^*) \quad (3.10)$$

where q and ϕ are defined by Eqs.(3.6) and (3.7).

The nonlinear polarizations arise from the third-order terms in the density matrix and depend on the two-level oscillation and the applied electric fields through the polarizability tensor components. The nonlinear polarization has the form

$$\vec{P}_\ell^{NL}(\vec{r}, t) = \frac{1}{2} \hat{\epsilon}_\ell P_\ell^{NL} \exp(ik_\ell z - i\omega_\ell t) + C.C. \quad (3.11)$$

The amplitudes for ω_1 and ω_2 are given by

$$P_1^{NL} = N \left[\alpha_{1,2} E_2^* q \exp(-i\Delta k_{12} z) + \alpha_{1,3}^* E_3 q^* \exp(i\Delta k_{31} z) \right] \quad (3.12a)$$

and

$$P_2^{NL} = N \left[\alpha_{1,2} E_1^* q \exp(-i\Delta k_{12}z) + \alpha_{2,4}^* E_4 q^* \exp(i\Delta k_{42}z) \right] \quad (3.12b)$$

The ASRS polarization amplitudes are given by

$$P_3^{NL} = N \alpha_{1,3} E_1 q \exp(-i\Delta k_{31}z) \quad (3.12c)$$

and

$$P_4^{NL} = N \alpha_{2,4} E_2 q \exp(-i\Delta k_{42}z) \quad (3.12d)$$

The equation of motion that governs the growth of traveling-wave electric fields in a two photon gain medium is the wave equation derived from Maxwell's equations.³⁶

$$-\nabla^2 \vec{E} + \frac{a n}{c} \frac{\partial \vec{E}}{\partial t} + \frac{n^2}{c^2} \frac{\partial^2 \vec{E}}{\partial t^2} = - \frac{1}{\epsilon_0 c^2} \frac{\partial^2 P^{NL}}{\partial t^2} \quad (3.13)$$

where the driving term is the nonlinear polarization of Eq. (3.11). The refractive index, n , in Eq.(3.13) is the value in the absence of the applied fields. The attenuation parameter, a , is the reciprocal of the distance at which the field intensity decreases to e^{-1} of the initial value in the absence of gain. Under the slowly-varying amplitude approximation Eqs.(3.1), (3.11), and (3.13) yield the amplitude growth equation for each frequency component. The

results are given by the following equation:

$$\frac{1}{2 i k_{\ell}} \nabla_{\perp}^2 E_{\ell} + \frac{\partial E_{\ell}}{\partial z} + \frac{n_{\ell}}{c} \frac{\partial E_{\ell}}{\partial t} + \frac{a_{\ell}}{2} E_{\ell} = \frac{i \omega_{\ell} P_{\ell}^{NL}}{2 n_{\ell} c \epsilon_0} \quad (3.14)$$

The first term on the left-hand side of Eq.(3.14) is the transverse Laplacian of the field amplitude. The nonlinear polarization amplitude, P_{ℓ}^{NL} , of Eqs.(3.12a) through (3.12d) drives the growth of the electric field in Eq.(3.14).

The electric field amplitude equations in Eq.(3.14) are coupled with the equations of motion for the two-level oscillation in Eq.(3.6) and the population difference in Eq. (3.10) through the nonlinear polarization amplitudes in Eqs. (3.12a) through (3.12d). This system of coupled differential equations constitutes a general description of the TPE and ASRS processes considered here. Unfortunately these equations cannot be solved analytically and require numerical methods^{34,35} to study the problem of two photon pulse amplification and energy extraction. Nevertheless, certain approximations in the coupled equations lead to a simplified set of equations which help to illustrate the first-order effects of a two photon gain medium. This includes pulse amplification and energy extraction in the unsaturated and saturated regimes. The approximations that lead to analytical expressions for these properties are discussed in the following sections.

C. TWO PHOTON AMPLIFICATION

A recent theoretical analysis of Raman scattering in the transient response regime ³⁷ indicates that the nonlinear gain decreases roughly proportionally with pulse length for pulse length shorter than the dephasing time. This evidence suggests that the efficient use of a two photon gain medium should be considered with relatively long pulses. However, the pulse must be short compared to the lifetime of the population inversion in order to minimize losses due to decay mechanisms. These operating restrictions imply an optimum condition for the two photon laser pulse length, τ :

$$T_2 \ll \tau \ll T_1 \quad (3.15)$$

The above relation also implies that steady-state approximation may be applicable in Eq.(3.6). Thus, the two-level oscillation amplitude, q , may be considered as a slowly-varying quantity provided that severe pulse shortening does not occur during amplification.

The steady-state approximation in Eq.(3.6) and the pulse length requirement in Eq.(3.15) significantly simplify the two photon field equations in Eq.(3.10) and Eq.(3.14). Furthermore, if the spatial and temporal characteristics of the two photon pulse change significantly more slowly than the amplitude growth, then Eq.(3.14) reduces to the following

equation:

$$\frac{\partial E_\ell}{\partial z} + \frac{1}{2} a_\ell E_\ell \approx \frac{i \omega_\ell P_\ell^{\text{NL}}}{2 n_\ell c \epsilon_0} \quad (3.16)$$

where

$$P_1^{\text{NL}} = \left(\frac{N u T_2}{4 i \hbar} \right) \left[\alpha_{1,2} E_2^* \phi \exp(-i\Delta k_{12} z) - \alpha_{1,3}^* E_3 \phi^* \exp(i\Delta k_{31} z) \right] \quad (3.17a)$$

$$P_2^{\text{NL}} = \left(\frac{N u T_2}{4 i \hbar} \right) \left[\alpha_{1,2} E_1^* \phi \exp(-i\Delta k_{12} z) - \alpha_{2,4}^* E_4 \phi^* \exp(i\Delta k_{42} z) \right] \quad (3.17b)$$

$$P_3^{\text{NL}} = \left(\frac{N u T_2}{4 i \hbar} \right) \alpha_{1,3} E_1 \phi \exp(-i\Delta k_{31} z) \quad (3.17c)$$

$$P_4^{\text{NL}} = \left(\frac{N u T_2}{4 i \hbar} \right) \alpha_{2,4} E_2 \phi \exp(-i\Delta k_{42} z) \quad (3.17d)$$

The population difference equation is now given by

$$\frac{\partial u}{\partial t} \approx - \frac{u T_2 |\phi|^2}{4 \hbar^2} \quad (3.18)$$

The nonlinear polarization amplitudes in Eqs.(3.17a) through (3.17d) contain contributions from both stimulated and coherent mixing effects. For example, Eq.(3.17a)

gives

$$\begin{aligned}
 P_1^{NL} = \left(\frac{N u T_2}{4 i \hbar} \right) & \left[|\alpha_{1,2}|^2 |E_2|^2 E_1 - |\alpha_{1,3}|^2 |E_3|^2 E_1 \right. \\
 & + \alpha_{1,2} \alpha_{2,4}^* E_2^* E_2^* E_4 \exp[i(\Delta k_{42} - \Delta k_{12}) z] \\
 & \left. - \alpha_{1,3}^* \alpha_{2,4} E_2 E_3 E_4^* \exp[i(\Delta k_{31} - \Delta k_{42}) z] \right]
 \end{aligned}
 \tag{3.19}$$

One can also express the nonlinear polarization in terms of the third-order susceptibility $\chi^{(3)}$. In MKS units Eq.(3.19) becomes

$$\begin{aligned}
 P_1^{NL} = \epsilon_0 \chi_1^{TPE} |E_2|^2 E_1 + \epsilon_0 \chi_1^{ASRS} |E_3|^2 E_1 \\
 + \epsilon_0 \chi_{1,2,2,4}^{(3)} E_2^* E_2^* E_4 \exp[i(\Delta k_{42} - \Delta k_{12}) z] \\
 + \epsilon_0 \chi_{1,3,2,4}^{(3)} E_2 E_3 E_4^* \exp[i(\Delta k_{31} - \Delta k_{42}) z]
 \end{aligned}
 \tag{3.20}$$

where,

$$\chi_1^{TPE} = \left(\frac{N u T_2}{4 i \hbar \epsilon_0} \right) |\alpha_{1,2}|^2, \tag{3.21a}$$

$$\chi_1^{ASRS} = - \left(\frac{N u T_2}{4 i \hbar \epsilon_0} \right) |\alpha_{1,3}|^2, \tag{3.21b}$$

$$\chi_{1,2,2,4}^{(3)} = \left(\frac{N u T_2}{4 i \hbar \epsilon_0} \right) \alpha_{1,2} \alpha_{2,4}^*, \tag{3.21c}$$

and

$$\chi_{3,1,2,4}^{(3)} = -\left(\frac{N u T_2}{4 i \hbar \epsilon_0}\right) \alpha_{1,3}^* \alpha_{2,4} \quad (3.21d)$$

The first two terms in Eq.(3.19) and Eq.(3.20) are independent of wave vector and represent the stimulated processes. The latter two terms containing $\chi_{1,2,2,4}^{(3)}$ and $\chi_{1,3,2,4}^{(3)}$ correspond to four-wave mixing processes, and they oscillate in space unless the wave vector mismatch vanishes. Equation (3.19) also indicates that the stimulated terms can yield either gain or loss depending on the field amplitudes at ω_2 and ω_3 .

The nonlinear polarization for the ASRS field at ω_3 also illustrates the contribution from stimulated and mixing processes. Eq.(3.17c) gives

$$\begin{aligned} P_3^{NL} = & \epsilon_0 \chi_3^{ASRS} |E_1|^2 E_3 \\ & + \epsilon_0 \chi_{3,1,1,2}^{(3)} E_1 E_1 E_2 \exp[i(\Delta k_{12} - \Delta k_{31})z] \\ & + \epsilon_0 \chi_{3,1,2,4}^{(3)} E_1 E_2^* E_4 \exp[i(\Delta k_{42} - \Delta k_{31})z] \end{aligned} \quad (3.22)$$

where,

$$\chi_3^{ASRS} = \chi_1^{ASRS}^* \quad (3.23a)$$

and the four-wave mixing susceptibilities are given by

$$\chi_{3,1,1,2}^{(3)} = \left(\frac{N u T_2}{4 i \hbar \epsilon_0} \right) \alpha_{1,3} \alpha_{1,2}^* \quad (3.23b)$$

and

$$\chi_{3,1,2,4}^{(3)} = \chi_{1,3,2,4}^{(3)*} \quad (3.23c)$$

An important aspect of Eq.(3.22) is that the ASRS field at ω_3 can be generated by ω_1 and ω_2 through four-wave mixing. This means that a TPE amplifier can generate and amplify ASRS signals at ω_3 and ω_4 . If the ASRS fields are allowed to grow at the expense of TPE field amplitudes, the ASRS process can eventually dominate and terminate TPE amplification. For energy extraction such competing processes are undesirable, since the efficiency depends not on the stored energy but on the photon flux at ω_1 or ω_2 .

If the coherent wave mixing processes can be neglected, then the field equations in Eq.(3.16) can be converted into intensity growth equations with intensity gain coefficients, δ^{TPE} and δ^{ASRS} . The growth of the ASRS fields is given by

$$\frac{\partial I_3}{\partial z} + a_3 I_3 = \delta_3^{\text{ASRS}} I_1 I_3 \quad (3.24a)$$

and

$$\frac{\partial I_4}{\partial z} + a_4 I_4 = \delta_4^{\text{ASRS}} I_2 I_4 \quad (3.24b)$$

The intensity equations for ω_1 and ω_2 are given by

$$\frac{\partial I_1}{\partial z} + a_1 I_1 = \delta_1^{\text{TPE}} I_1 I_2 - \delta_1^{\text{ASRS}} I_3 I_1 \quad (3.24c)$$

and

$$\frac{\partial I_2}{\partial z} + a_2 I_2 = \delta_2^{\text{TPE}} I_1 I_2 - \delta_2^{\text{ASRS}} I_4 I_2 \quad (3.24d)$$

The intensity gain coefficients in Eq.(3.24) are defined by

$$\begin{aligned} \delta_2^{\text{TPE}} &= \left(\frac{\omega_2}{\omega_1}\right) \delta_1^{\text{TPE}} \\ &= \frac{N u \omega_2 |\alpha_{1,2}|^2}{\Gamma n_1 n_2 \hbar \epsilon_0^2 c^2} \end{aligned} \quad (3.25)$$

$$\begin{aligned} \delta_1^{\text{ASRS}} &= \left(\frac{\omega_1}{\omega_3}\right) \delta_3^{\text{ASRS}} \\ &= \frac{N u \omega_1 |\alpha_{1,3}|^2}{\Gamma n_1 n_3 \hbar \epsilon_0^2 c^2} \end{aligned} \quad (3.26)$$

and

$$\begin{aligned} \delta_2^{\text{ASRS}} &= \left(\frac{\omega_2}{\omega_4}\right) \delta_4^{\text{ASRS}} \\ &= \frac{N u \omega_2 |\alpha_{2,4}|^2}{\Gamma n_2 n_4 \hbar \epsilon_0^2 c^2} \end{aligned} \quad (3.27)$$

In the above definitions the FWHM transition frequency width, Γ (radian-second⁻¹), has been substituted for $(2/T_2)$.

The intensity gain coefficients can also be expressed in terms of the TPE and ASRS cross-sections. The Raman scattering cross-section at ω_j due to ω_i is defined by the following formula which includes the degeneracy of the magnetic states of the initial and final states.^{38,39}

$$\left(\frac{d\sigma}{d\Omega}\right)_{i,j} = \frac{\omega_i \omega_j^3}{(4\pi \epsilon_0)^2 c^4} \frac{1}{2J_b + 1} \sum_{M_b} \sum_{M_a} |\alpha_{i,j}|^2 \quad (3.28)$$

The TPE cross-section can be defined in the same way. A direct substitution of Eq.(3.28) into Eqs.(3.25), (3.26), and (3.27) yields the desired relations in terms of $\lambda_\ell = 2\pi/k_\ell$.

$$\delta_2^{\text{TPE}} = 4 \lambda_2^2 \frac{N u}{\Gamma \hbar \omega_1} \left(\frac{d\sigma}{d\Omega}\right)_{1,2} \quad (3.29)$$

$$\delta_1^{\text{ASRS}} = 4 \lambda_1^2 \frac{N u}{\Gamma \hbar \omega_3} \left(\frac{d\sigma}{d\Omega}\right)_{3,1} \quad (3.30)$$

$$\delta_2^{\text{ASRS}} = 4 \lambda_2^2 \frac{N u}{\Gamma \hbar \omega_4} \left(\frac{d\sigma}{d\Omega}\right)_{4,2} \quad (3.31)$$

Since $(d\sigma/d\Omega)$ is an experimentally measured quantity, Eqs.(3.29), (3.30), and (3.31) provide useful relations for δ^{TPE} and δ^{ASRS} . If $(d\sigma/d\Omega)$ data are not available, approximate values may be calculated using Eq.(3.28). Appendices C and D describe useful techniques for evaluating the summation in Eq.(3.28).

D. ENERGY EXTRACTION

The important parameters that characterize a two photon amplifier are energy storage, intensity gain, and extraction efficiency. These quantities are related by a system of coupled differential equations derived in Section C. The equations are nonlinear, and a general analytical solution cannot be obtained even in the steady-state regime.

However, the equations are solvable under certain conditions and approximations. For example, if linear absorption, four-wave mixing, and medium saturation can be neglected, a proper choice of initial conditions on the field intensities provide the first-order approximation for the TPE or ASRS process. This approximation describes the unsaturated regime.

The intensity equations in the unsaturated TPE case are

$$\frac{\partial I_1}{\partial z} = \delta_1^{\text{TPE}} I_1 I_2 \quad (3.32a)$$

and

$$\frac{\partial I_2}{\partial z} = \delta_2^{\text{TPE}} I_1 I_2 \quad (3.32b)$$

where $I_3 = I_4 = 0$ is assumed initially. The exact solutions to Eqs.(3.32a) and (3.32b) are

$$\frac{I_1(z)}{I_1(0)} = \frac{(1 - \rho)(1 + \rho e^A)}{(1 - \rho e^A)} \quad (3.33a)$$

and

$$\frac{I_2(z)}{I_2(0)} = \frac{(1 - \rho) e^A}{(1 - \rho e^A)} \quad (3.33b)$$

where

$$\rho = \frac{\omega_1}{\omega_2} \frac{I_2(0)}{I_1(0)} \quad (3.34)$$

and

$$A = \delta_2^{\text{TPE}} I_1(0) z (1 - \rho) \quad (3.35)$$

The solutions show that when $I_2(0) \ll I_1(0)$, the intensity at ω_2 grows exponentially, which agrees with Carman's result.⁶

The unsaturated ASRS intensity growth can be solved similarly using

$$\frac{\partial I_1}{\partial z} = - \delta_1^{\text{ASRS}} I_1 I_3 \quad (3.36a)$$

and

$$\frac{\partial I_3}{\partial z} = + \delta_3^{\text{ASRS}} I_1 I_3 \quad (3.36b)$$

where $I_2(0) = I_4(0) = 0$ is assumed. The exact solutions to Eqs.(3.36a) and (3.36b) are

$$\frac{I_1(z)}{I_1(0)} = \frac{(1 + \zeta)}{(1 + \zeta e^B)} \quad (3.37a)$$

and

$$\frac{I_3(z)}{I_3(0)} = \frac{(1 + \zeta)}{(1 + \zeta e^B)} \quad (3.37b)$$

where

$$\zeta = \frac{\omega_1}{\omega_3} \frac{I_3(0)}{I_1(0)} \quad (3.38)$$

and

$$B = \delta_3^{\text{ASRS}} I(0) z (1 + \zeta) \quad (3.39)$$

For a small input signal at ω_3 Eq.(3.37b) reduces to an exponential growth provided that saturation remains negligible.

The analytical solutions for the unsaturated case describe the initial growth behavior in which a very small amount of the stored energy is extracted. However, a two photon amplifier must operate in the saturated regime for efficient energy extraction. Thus, analytical intensity growth formulas including saturation effects are desirable. As mentioned earlier, the coupled nonlinear equations for the fields and the medium are not generally solvable. To alleviate this difficulty one can consider the saturation problem for the special case of an ideal TPE amplifier.

An ideal TPE gain medium may be considered to have no linear absorption and negligible nonlinear gain coefficient for the competing ASRS processes. This also implies that four-wave mixing terms do not contribute significantly. These conditions are hypothetical, but they simplify the equations to a point where analytical solutions including saturation can be obtained. Of course the analytical

solutions are only solutions to an approximate system of equations and are subject to the validity of certain assumptions. Nevertheless, the analytical expressions can be helpful in studying the approximate saturation characteristics of an ideal TPE amplifier.

The equations that describe an ideal TPE amplifier are Eqs.(3.22a) and (3.22b) and

$$\frac{\partial u}{\partial t} = - \frac{u T_2 |\alpha_{1,2}|^2}{4 \hbar^2} |E_1|^2 |E_2|^2 \quad (3.40)$$

where Eq.(3.40) arises from Eqs.(3.15) and (3.18) and the following conditions:

$$|\alpha_{1,3}|^2 \ll |\alpha_{1,2}|^2 \quad ; \quad |\alpha_{2,4}|^2 \ll |\alpha_{1,2}|^2 \quad (3.41)$$

If the field intensities are divided by the respective photon energy, the equations are transformed into photon flux equations.

$$\frac{\partial x_1}{\partial z} = \beta x_1 x_2 u \quad , \quad (3.42a)$$

$$\frac{\partial x_2}{\partial z} = \beta x_1 x_2 u \quad , \quad (3.42b)$$

and

$$\frac{\partial u}{\partial z} = \theta x_1 x_2 u \quad , \quad (3.42c)$$

where $x_i = I_i / \hbar \omega_i$. The parameters β and θ are given by

$$\theta = \frac{2 \omega_1 \omega_2 |\alpha_{1,2}|^2}{\Gamma n_1 n_2 c^3 \epsilon_0^2} \quad (3.43)$$

and

$$\beta = \frac{1}{2} N c \theta \quad (3.44)$$

Equations (3.42a) and (3.42b) indicate that the photon flux at ω_1 and ω_2 must grow simultaneously from the initial values, x_1^0 and x_2^0 , respectively. Mathematically,

$$x_1 = x_1^0 + x \quad , \quad (3.45a)$$

$$x_2 = x_2^0 + x \quad , \quad (3.45b)$$

and

$$\frac{\partial x_1}{\partial z} = \frac{\partial x_2}{\partial z} = \frac{\partial x}{\partial z} \quad (3.45c)$$

Equations (3.45c) and (3.42c) can be combined to obtain an equation for u in terms of x :

$$u = u_0 \left(1 - \frac{x}{x_0}\right) \quad (3.46)$$

where u_0 is the initial value, and $x_0 = \frac{1}{2} Nu_0 c$ is the maximum photon flux that can be extracted from the medium. Therefore, (x/x_0) in Eq.(3.46) corresponds to the extraction efficiency. Substituting Eqs.(3.45) and (3.46) into Eq.(3.42) yields an equation for the extraction efficiency, ξ :

$$\int_0^\xi \theta dz = \frac{1}{x_0^2} \int_0^\xi \frac{d\xi'}{(\xi' + r_1)(\xi' + r_2)(1 - \xi')} \quad (3.47)$$

where the initial values of photon flux at ω_1 and ω_2 are normalized to x_0 according to

$$r_1 = \frac{x_1^0}{x_0} ; \quad r_2 = \frac{x_2^0}{x_0} \quad (3.48)$$

Direct integration of Eq.(3.47) leads to a relationship between the extraction efficiency and the various parameters:

$$G(1+r_1)(1+r_2) = \left(\frac{1+r_1}{r_1-r_2} \right) \ln \left[1 + \frac{\xi}{r_2} \right] - \ln(1-\xi) - \left(\frac{1+r_2}{r_1-r_2} \right) \ln \left[1 + \frac{\xi}{r_1} \right] \quad (3.49)$$

where $G = \theta \ell x_0^2$ is a dimensionless parameter that determines the gain of the amplifier. A quick check of Eq.(3.49) at the

unsaturated limit ($\xi \ll 1$) shows that the equation indeed reduces to Eq.(3.33b). Equation (3.49) can also describe the degenerate TPE case ($\omega_1 = \omega_2$) after a slight mathematical manipulation. The formula for this special case is given by

$$G(1+r)^2 = \frac{\xi(1+r)}{r^2(1+\frac{\xi}{r})} + \ln \left[\frac{1+\frac{\xi}{r}}{1-\xi} \right] \quad (3.50)$$

The relations derived in Eqs.(3.49) and (3.50) constitute an approximate description of the saturation characteristics of an ideal TPE amplifier operating in the steady-state regime. The next step is to determine the parameters that optimize the performance of the amplifier under certain initial conditions. The performance may be evaluated on the basis of the extraction efficiency and the amplification factor, \mathcal{A} , which is defined as the ratio of the output energy to the input energy at the same frequency. Ideally a near unity extraction efficiency and a large amplification factor are desirable.

Efficient extraction ($\xi \lesssim 1$) and large amplification factors for both TPE frequencies require $r_1 \ll \xi$ and $r_2 \ll \xi$. If $r_1 \gtrsim r_2$, Eq.(3.49) simplifies to

$$\xi \approx 1 - e^{-G \left(\frac{r_1}{r_2} \right)^{\left(\frac{1}{r_1 - r_2} \right)}} \quad (3.51)$$

Thus, efficient extraction requires $G \gg 1$. Conversely,

if $G < 1$ efficient extraction may not be possible with large amplification factors.

In another mode of operation TPE extraction uses an intense "trigger" field at ω_1 in order to achieve $\mathcal{A}_2 \gg 1$ and $\xi \lesssim 1$. In this case r_1 is at least one and possibly much larger. These conditions reduce Eq.(3.49) to

$$\xi \approx r_2 \left[\frac{1 - \exp(-Gr_1)}{r_2 + \exp(-Gr_1)} \right] \quad (3.52)$$

The corresponding amplification factor is given by

$$\mathcal{A}_2 \equiv 1 + \frac{\xi}{r_2} \quad (3.53a)$$

or

$$\mathcal{A}_2 \approx \frac{1}{r_2 + \exp(-Gr_1)} \quad (3.53b)$$

The expressions for ξ and \mathcal{A}_2 suggest that if $Gr_1 \ll 1$ high extraction efficiencies are not possible with $\mathcal{A}_2 \gg 1$ because $r_2 \ll 1$ must hold. On the other hand, if $Gr_1 > 1$ such that $\exp(-Gr_1) \lesssim r_2 \ll 1$, then reasonable extraction efficiencies can be expected. Therefore, the "trigger" pulse at ω_1 with $r_1 \gg 1$ can operate a TPE amplifier with $G < 1$ and still achieve high extraction efficiency and amplification at ω_2 . Figures 4 and 5 illustrate the behavior

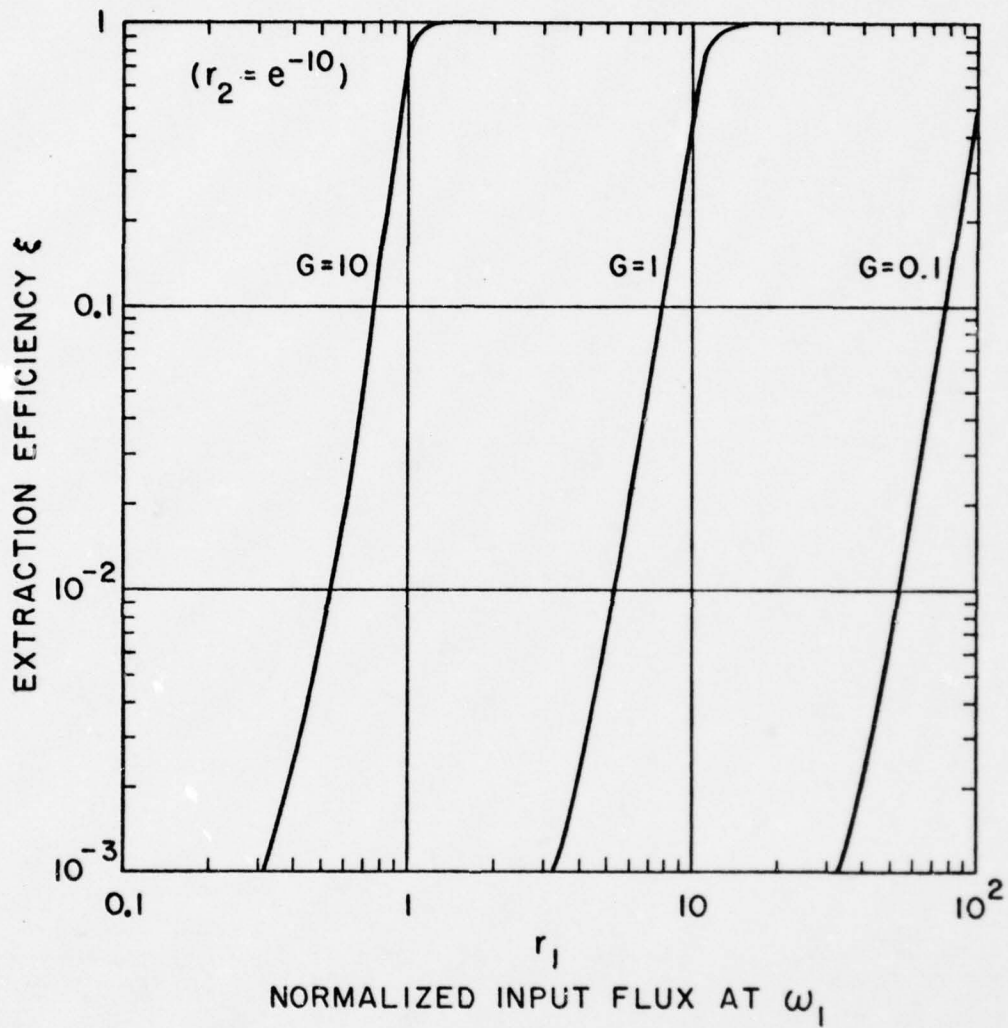


Fig. 4 -- Ideal TPE amplifier extraction efficiency vs. normalized input (trigger) photon flux at ω_1 for $r_2 = \exp(-10)$.

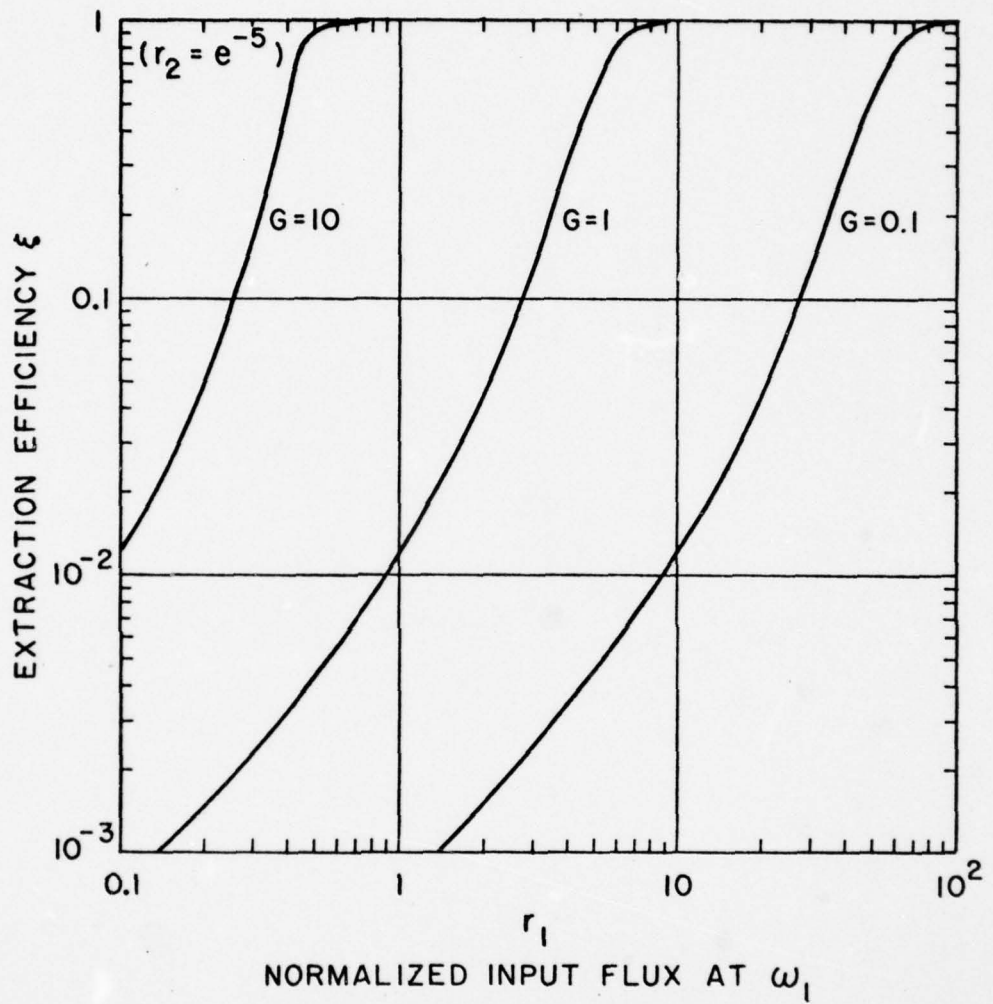


Fig. 5 -- Ideal TPE amplifier extraction efficiency vs. normalized input (trigger) photon flux at ω_1 for $r_2 = \exp(-5)$.

of ξ as a function of r_1 at various values of G .

Figure 4 assumes $r_2 = \exp(-10)$, and Fig. 5 uses $r_2 = \exp(-5)$.

A third method of energy extraction involves degenerate TPE amplification. The saturation behavior as given by Eq.(3.50) differs from the non-degenerate case. The amplification factor for the degenerate case is defined by

$$\mathcal{A} \equiv 1 + \frac{\xi}{r} \quad (3.54)$$

For small input intensities, $r \ll 1$, efficient extraction requires

$$G \approx \frac{\xi}{r} - \ln(1 - \xi) \quad (3.55)$$

This implies that $G \gg 1$ is necessary in order to achieve a large amplification factor. On the other hand, $r \gg 1$ in Eq.(3.50) leads to

$$\xi \approx 1 - \exp(-Gr^2) \quad (3.56)$$

Thus, extraction efficiencies near unity can be achieved with $G \ll 1$. However, the amplification factor may be very close to unity, since $\xi \ll r$. Therefore, experimentally the degenerate TPE extraction is not very interesting if $G < 1$. Furthermore, small values of G may pose detection problems which would make a demonstration of TPE amplification difficult.

Figure 6 gives a plot of ξ as a function of r at various values of G . The dashed lines indicate the values of $\mathcal{A} - 1$. For example, if $G = 0.1$, $r = 1$ yields $\xi \approx 0.1$ and an amplification factor of $\mathcal{A} = 1.1$. However, if $G = 10^{-3}$ and $r = 10^2$, then the extraction efficiency is near unity; but, the relative change in the field intensity after amplification is only one part in 10^2 . The graphs in Fig. 6 suggest that the best performance is obtained when the operating point lies in the upper left corner where $G > 1$, $r < 1$, and $\mathcal{A} > 1$.

In all three modes of operation of a TPE amplifier the parameter G plays an important role with respect to the performance characteristics. Since large values of G are desirable in all cases, one must optimize parameters that govern G . From the definition of G and Eqs.(3.25) and (3.43) a formula for G is given by

$$G = \delta_2^{\text{TPE}} \hbar \omega_1 x_0 \ell \quad (3.57)$$

where

$$x_0 = \frac{1}{2} N u_0 c \quad (3.58)$$

In Eq.(3.57) δ_2^{TPE} is the unsaturated intensity gain coefficient given by Eq.(3.25), and ℓ is the length of the gain medium. The quantity x_0 is the maximum photon flux that can be extracted from the medium, and $\hbar \omega_1 x_0$ corresponds to the intensity of the trigger field at which $r_1 = 1$.

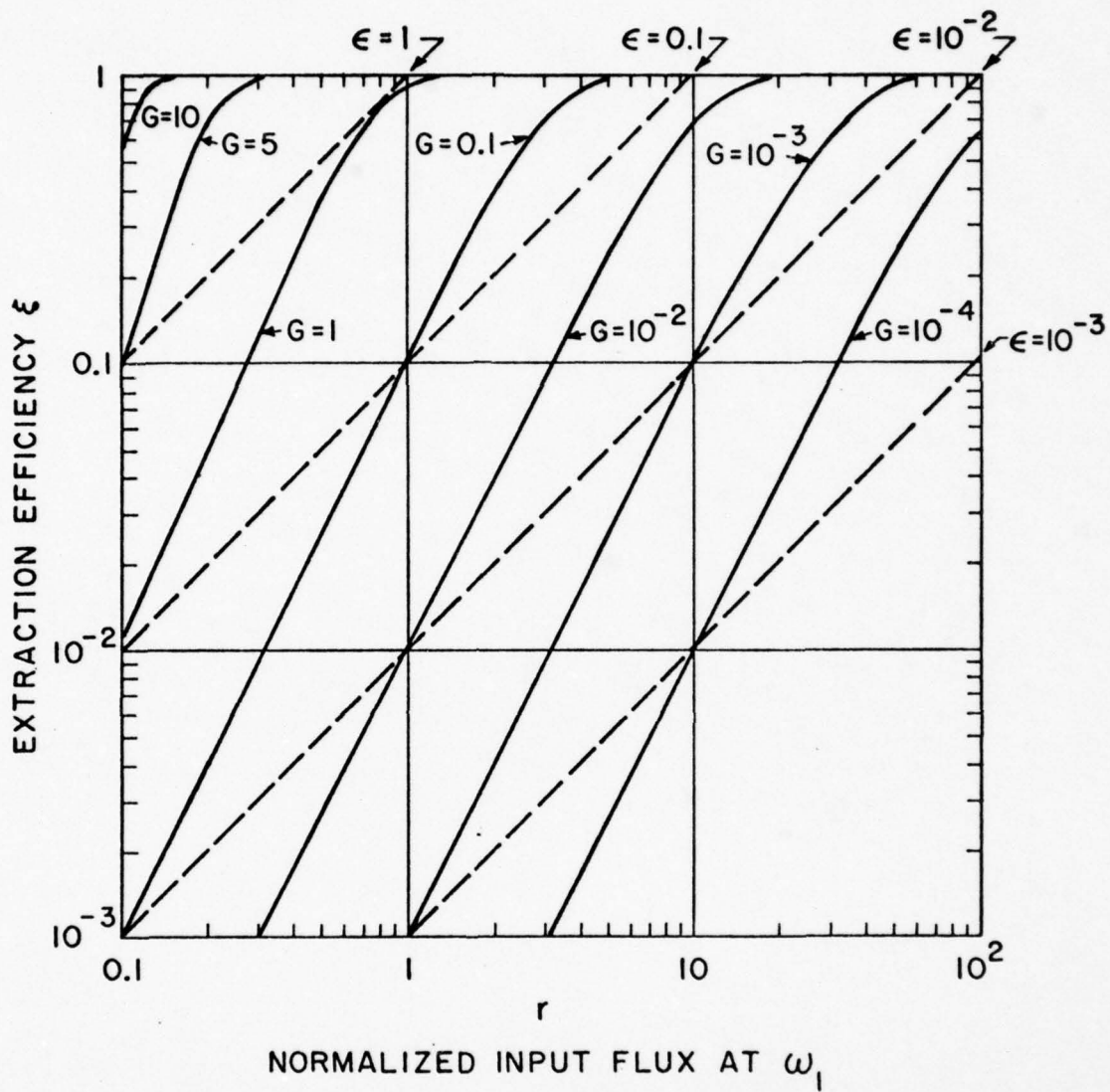


Fig. 6 -- Ideal degenerate ($\omega_1 = \omega_2$) TPE amplifier extraction efficiency vs. normalized input photon flux. Energy amplification factor is given by $\mathcal{A} = 1 + \epsilon$.

Since both δ_2^{TPE} and x_0 are proportional to the inversion density, Nu_0 , G varies as $(Nu_0)^2 \ell$. Therefore, the inversion density and amplifier length should be maximized in order to achieve the largest possible values of G . Table I shows typical calculated values of G based on $\ell = 100$ cm and $\delta_2^{\text{TPE}} = 10^{-6}$ cm/MW at $Nu_0 = 10^{16}$ cm $^{-3}$. This value of δ_2^{TPE} is a realistic order of magnitude estimate which is discussed in more detail in Chapter IV.

The significance of the numerical estimates of G in Table I is that realistic conditions exist for an efficient TPE amplifier. From the discussion of energy storage capacity in Chapter II population inversion densities in the range of 10^{17} to 10^{18} cm $^{-3}$ may be achieved under optimum conditions. This suggests that the values of G in the range of 1 to 10 are possible and that the amplified field intensities may reach on the order of 10^9 W/cm 2 with a high extraction efficiency. For inversion densities in the range of 10^{16} to 10^{17} cm $^{-3}$ G rapidly decreases to much less than unity. However, efficient extraction and TPE amplification of the complementary field at ω_2 are still feasible provided that the trigger intensities with $I_1(0) \gg \hbar \omega_1 x_0$ are available. Under these conditions the field intensity at ω_2 may be amplified to greater than 10^7 W/cm 2 . In the case of a degenerate TPE amplifier $G > 1$ is a necessary condition for efficient extraction and amplification. Hence, inversion densities in the range of 10^{17} to 10^{18} cm $^{-3}$ are required.

Table I

IDEAL TPE AMPLIFIER PARAMETERS

$N u_o$ (cm^{-3})	ℓ (cm)	δ_2^{TPE} (cm/MW)	G	x_o ($\text{cm}^{-2}\text{-sec}^{-1}$)	$\hbar\omega_1 x_o^*$ (MW/ cm^2)
10^{16}	100	10^{-6}	1.5×10^{-3}	1.5×10^{26}	15
10^{17}	100	10^{-5}	0.15	1.5×10^{27}	150
10^{18}	100	10^{-4}	15	1.5×10^{28}	1500

* Calculations based on a trigger field wavelength of $2\mu\text{m}$.

The discussion of an ideal TPE amplifier so far has assumed that the competing ASRS processes are negligible due to the conditions of Eq.(3.41). However, in real cases such conditions may not be easily satisfied. Figures 7a and 7b show schematic level diagrams for a two photon amplifier. If the intermediate states lie below the upper state as in Fig. 7b, the detuning, Δ_{12} , favors the TPE process. However, superfluorescent decay to the intermediate states can quickly deplete the energy stored in the upper state. Thus, a level structure of the type in Fig. 7b is not desirable. On the other hand, if the intermediate states lie above the upper state as in Fig. 7a, the detuning, Δ_{13} , may favor the ASRS processes by the near-resonance enhancement. For an ASRS amplifier this condition is advantageous, but such a level arrangement may prevent TPE amplification. A possible way of overcoming the ASRS enhancement is to pick ω_1 such that destructive interference among the intermediate states diminishes the ASRS gain.⁴⁰

In summary, this chapter briefly reviewed the theory of two photon energy-extraction from an inverted metastable system. The coupled differential equations that govern the growth and evolution of the optical fields and the medium have been treated in the steady-state regime in order to describe the optimum pulse lengths. An approximate description of the saturation characteristics of an ideal TPE amplifier was considered for pulse lengths for which $T_2 \ll \tau$

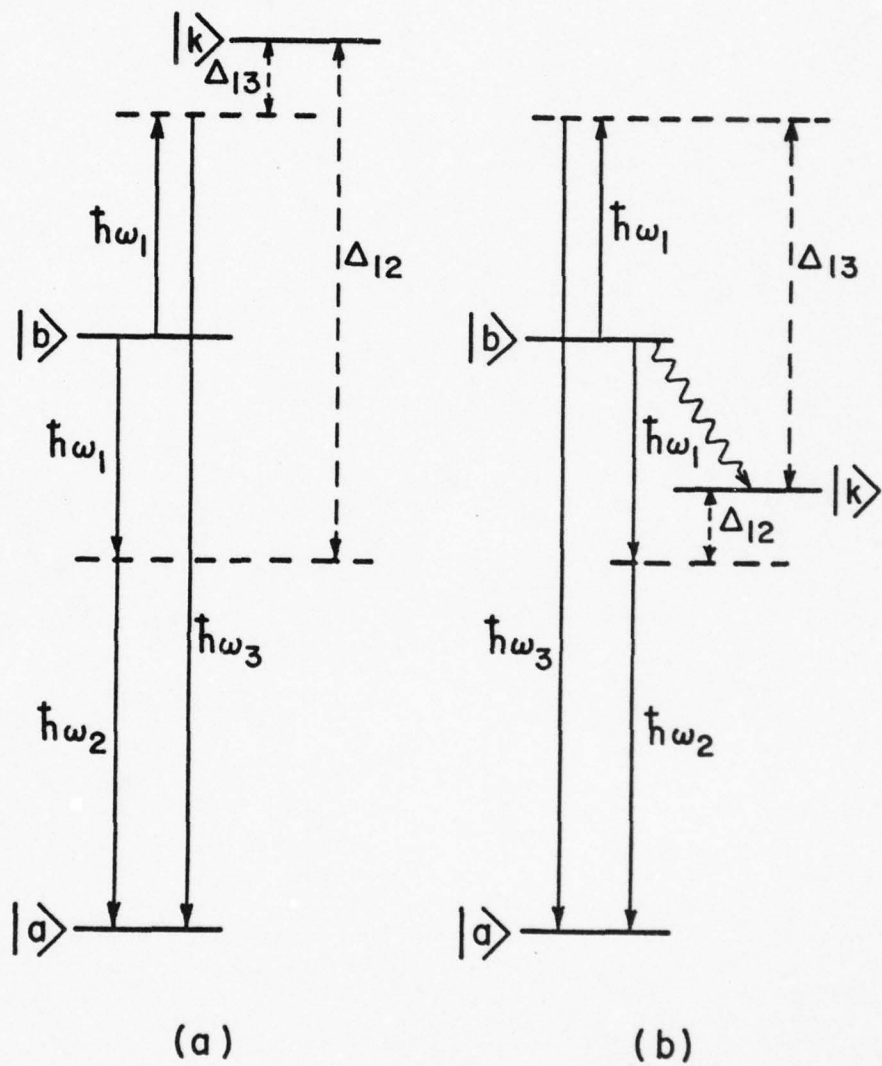


Fig. 7 -- Energy level structure for two photon gain medium: (a) Intermediate states $|k\rangle$ above the energy storage, state $|b\rangle$; (b) intermediate states $|k\rangle$ below $|b\rangle$ in which radiative decay from $|b\rangle$ to $|k\rangle$ is allowed.

and $\tau \ll T_1$ are satisfied. In the absence of competing processes and severe pulse distortion the solution to a simplified set of coupled equations led to analytical relations between the extraction efficiency and the TPE gain parameter G . The numerical estimates of G showed that efficient TPE energy extraction and amplification are possible with population inversion densities achievable in a vapor medium consisting of excited metastable species. For inversion densities on the order of 10^{17} to 10^{18} cm^{-3} the calculations suggested that amplified intensities on the order of 10^9 W/cm^2 with high extraction efficiencies are feasible in an ideal TPE amplifier. Although a brief consideration of energy level structure did not suggest an ideal TPE amplifier the analytical saturation behavior may provide a helpful guide for studying more realistic systems in the future.

CHAPTER IV

PROPOSED SYSTEMS AND FEASIBILITY ANALYSIS

A. INTRODUCTION

An atomic or molecular metastable species for a potential two photon gain medium must satisfy a number of requirements on the radiative and non-radiative decay properties as well as energy level structure for population inversion. A careful survey of the periodic table shows that not many neutral atoms have an energy level structure that permits energy storage and population inversion. Moreover, in many of these candidates high densities of metastable states are difficult to achieve experimentally. For example, high temperatures are required to generate a sufficient vapor pressure in some metal vapor systems. Light elements tend to form molecules readily. These physical and chemical properties further reduce the number of potential candidates to only a few neutral atomic and molecular species.

A potential two photon gain medium selected from the above considerations is also subject to certain bounds imposed by the optical properties of the medium as shown in a recent feasibility analysis by Carman.⁶ The study indicates that general considerations of the optical properties lead to several

constraints on the optical intensities and pulse lengths as well as device dimensions and inversion densities.

This chapter illustrates some of the properties of two proposed atomic systems for potential active media using two photon extraction schemes. The first system is an anti-Stokes Raman frequency up-converter in neutral atomic mercury which is described in detail in Appendix E. The second system is a two photon amplifier based on population inversion in atomic iodine. For each system a brief feasibility analysis is presented in terms of experimental requirements.

B. ATOMIC MERCURY ASRS FREQUENCY UP-CONVERTER

1. Population Inversion and Storage Mechanism

The low lying excited states of neutral atomic mercury are the metastable $6^3P_{0,1,2}^o$ states and the resonance $6^1P_1^o$ state. The singlet state lies higher than the triplet states and radiatively couples to the 6^1S_0 ground state with a 185 nm resonance line as shown in Fig. 8. The transition has a near unity oscillator strength and exhibits radiation imprisonment (trapping) effects even at modest atomic vapor densities.⁴¹ The radiation imprisonment increases the apparent radiative lifetime of the resonance state since the radiation diffuses out from an excited region by a repeated

MERCURY ENERGY LEVELS

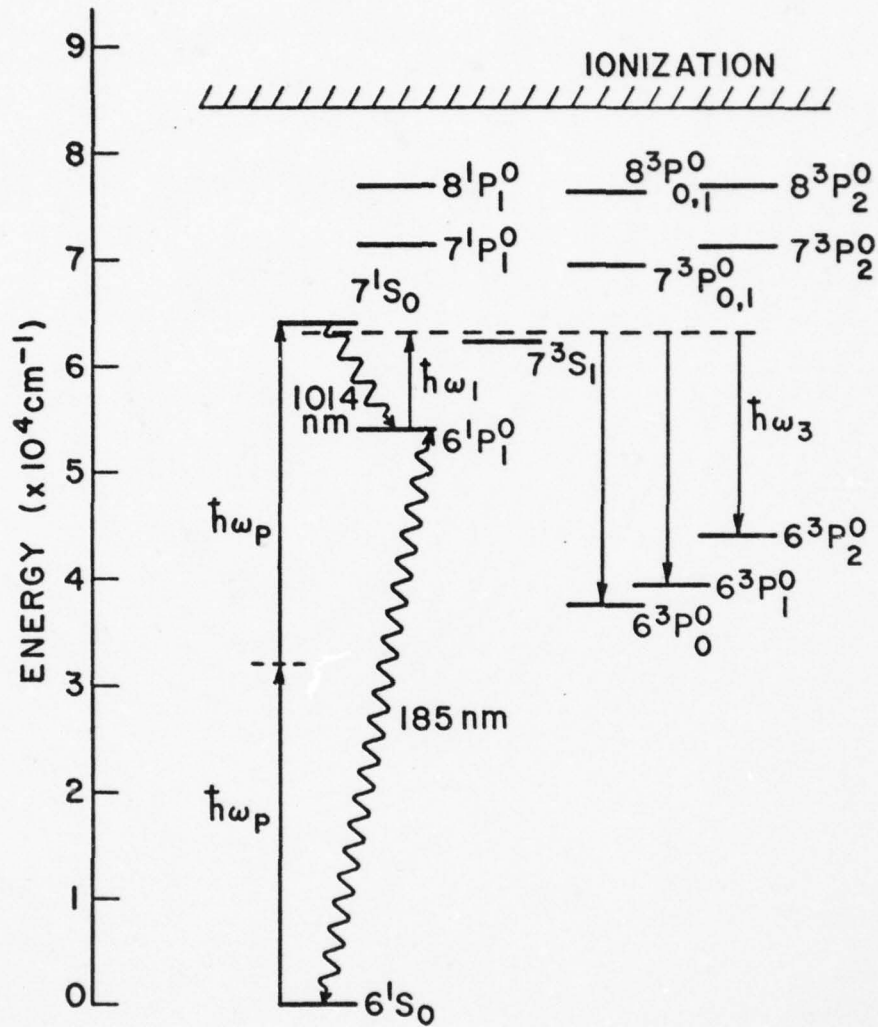


Fig. 8 -- Abbreviated energy level diagram of atomic mercury for ASRS amplifier. The radiation trapped 185 nm transition gives energy storage in the 6¹P₁ state.

process of emission and absorption. According to experiments and a theory developed by Holstein⁴² an increase in the radiative decay by several orders of magnitude is not uncommon for resonance transitions.²⁸ This radiative property of the resonance states suggests their natural tendency to store energy in a volume of excited vapor with an effective lifetime on the order of microseconds.

The energy stored in the radiatively trapped $6^1P_1^0$ state may lead to population inversion with respect to the triplet states under certain conditions. Since $6^1P_1^0$ and $6^3P_J^0$ states have the same parity and a different multiplicity, only inter-system magnetic dipole and electric quadrupole transitions can contribute to one photon decay from $6^1P_1^0$ to $6^3P_J^0$. These transitions are only very weakly allowed because both a higher order multipole process and a departure from the L-S coupling are involved. In contrast two photon transitions between $6^1P_1^0$ and $6^3P_J^0$ only require an intermediate state which is coupled to both states by an allowed transition and an intercombination transition. Since intercombination transitions in mercury are relatively strong, a population inversion in the $6^1P_1^0 - 6^3P_J^0$ system is a potential two photon gain medium. The details of this proposed system are discussed in Appendix E. The following section describes recent two photon gain calculations.

2. Two Photon Gain Calculations

The calculation of two photon gain in mercury involves evaluating all relevant matrix elements for intermediate states in the intermediate angular momentum coupling scheme. However, in practice, such calculations may be simplified for frequencies that are close to the one-photon transition frequency of an intermediate state. The near-resonance condition not only reduces the number of intermediate states to just a few, but also enhances the two photon gain. Experimentally such near-resonance enhancement in nonlinear optical processes has been observed in two-photon absorption,⁴³ Raman scattering,^{44,45} third harmonic generation,⁴⁶ and four-wave mixing processes.⁴⁷ This section illustrates the use of computational methods described in Appendices C and D in calculating the ASRS cross-sections in Hg within the near-resonance approximation.

The energy level structure of mercury as shown in Fig. 8 has two major contributions to the two photon gain from the 7^1S_0 and 7^3S_1 states lying above the $6^1P_1^0$ state. Due to the positions of the intermediate states anti-Stokes Raman scattering dominates over two-photon emission. In particular the ASRS cross-section may be expected to increase dramatically for frequencies close to the $6^1P_1^0 - 7^1S_0$ ($\lambda = 1014$ nm) and $6^1P_1^0 - 7^3S_1$ ($\lambda = 1207$ nm) transitions due to the near-resonance enhancement.

The ASRS cross-section, $(d\sigma/d\Omega)$, for the $6^1P_1^0 - 6^3P_J^0$ transitions can be calculated from Eq.(3.28). Using the near-resonance approximation for the two intermediate states a simplified formula is given by

$$\left(\frac{d\sigma}{d\Omega}\right)_{\text{ASRS}} = \frac{\omega_1 \omega_3^3}{3c^4} \sum_m \left| \sum_k R_k \left[\frac{S_p}{\hbar(\omega_{kb} - \omega_1)} + \frac{(-1)^p S_{-p}}{\hbar(\omega_{kb} + \omega_3)} \right] \right|^2 \quad (4.1)$$

where the summation over the intermediate states, $|k\rangle$, includes contributions from the 7^3S_1 and the 7^1S_0 states. Various parameters in Eq.(4.1) are given by the following expressions using the abbreviations, $|t\rangle$ and $|s\rangle$, to represent the triplet and the singlet intermediate states, respectively. The upper level is denoted by $|b\rangle = |6^1P_1^0\rangle$; the lower levels are represented by $|a\rangle = |6^3P_J^0\rangle$, where J is equal to 0, 1, or 2. The reduced matrix element products are given by

$$R_k = \langle a || \vec{u} || k \rangle \langle b || \vec{u} || k \rangle^* \quad (4.2)$$

where $k = s$ or $k = t$. The $3j$ symbol factors, S_p and S_{-p} , are defined by

$$S_p = \begin{pmatrix} 1 & 1 & J_k \\ -m & 0 & m \end{pmatrix} \begin{pmatrix} J & 1 & J_k \\ -m-p & p & m \end{pmatrix} \quad (4.3a)$$

and

$$S_{-p} = \begin{pmatrix} 1 & 1 & J_k \\ -m & -p & m+p \end{pmatrix} \begin{pmatrix} J & 1 & J_k \\ -m-p & 0 & m+p \end{pmatrix} \quad (4.3b)$$

where $J_s = 0$ and $J_t = 1$. The intermediate state transition energies are

$$\hbar \omega_{sb} = E_s - E_b = 9859 \text{ cm}^{-1} \quad (4.4a)$$

and

$$\hbar \omega_{tb} = E_t - E_b = 8282 \text{ cm}^{-1} \quad (4.4b)$$

The near-resonance approximation in Eq.(4.1) assumes that the incident frequency, ω_1 , is close to ω_{sb} or ω_{tb} . The ASRS frequency, ω_3 , is shifted up by 10027 cm^{-1} for $J = 2$, 14657 cm^{-1} for $J = 1$, and 16424 cm^{-1} for $J = 0$. The ASRS cross-sections for the polarized ($p = 0$) and depolarized ($p = -1$) cases can be computed by evaluating Eqs.(4.3a) and (4.3b) with a proper value of p .

The numerical values of R_k can be obtained from experimental data⁴⁸⁻⁵⁰ according to a procedure described in Appendix D. The values of R_k for mercury are listed in Table II, and the relative signs are determined from the mixing coefficients of the $6^1P_1^0$, $6^3P_1^0$, 6^1D_2 , and 6^3D_2 states in the intermediate coupling scheme. The following coefficients are used

Table II

THE VALUES OF R_k FOR MERCURY

$ a\rangle$	$ k\rangle$	sign	R_k $(ea_0)^2$	$\hbar \omega_{kb}$ (cm^{-1})
$6^3P_2^o$	6^3D_1	\pm	0.2	17265
	7^3S_1	\pm	13.0	8282
	6^3D_2	+	5.3	17327
	6^1D_2	-	4.0	17264
$6^3P_1^o$	6^1S_0	-	1.2	-54069
	7^1S_0	-	2.4	9859
	6^3D_1	\pm	0.6	17267
	7^3S_1	+	8.9	8282
	6^3D_2	+	7.8	17327
	6^1D_2	-	6.5	17264
$6^3P_0^o$	6^3D_1	\pm	0.7	17267
	7^3S_1	\pm	5.6	8282

 \pm indicates undetermined relative sign.

to describe the perturbed wave functions:^{51,52}

$$|6^1P_1^0\rangle_I = \alpha|6^1P_1^0\rangle_{LS} + \beta|6^3P_1^0\rangle_{LS} \quad (4.5a)$$

$$|6^3P_1^0\rangle_I = \alpha|6^3P_1^0\rangle_{LS} - \beta|6^1P_1^0\rangle_{LS} \quad (4.5b)$$

$$\alpha = 0.9849, \quad \beta = -0.1732 \quad (4.5c)$$

$$|6^1D_2\rangle_I = \alpha'|6^1D_2\rangle_{LS} + \beta'|6^3D_2\rangle_{LS} \quad (4.6a)$$

$$|6^3D_2\rangle_I = \alpha'|6^3D_2\rangle_{LS} - \beta'|6^1D_2\rangle_{LS} \quad (4.6b)$$

$$\alpha' = 0.8067, \quad \beta' = 0.5909 \quad (4.6c)$$

The ASRS cross-sections obtained from Eq.(4.1) through Eq.(4.4) and Table II are plotted in Figs. 9, 10, and 11 as a function of the incident photon energy. The solid and the dashed curves represent $(d\sigma/d\Omega)$ for the polarized (\parallel) and depolarized (\perp) cases, respectively. The solid vertical lines and the states labeled above correspond to the intermediate states. The dashed vertical lines indicate the frequencies at which two-photon absorption (TPA) resonances are expected, and the states labeled above each line indicate the final states in TPA. The graphs of $(d\sigma/d\Omega)$ clearly illustrate the near-resonance enhancement of the cross-section as the incident frequency approaches the transition frequencies of the intermediate states. The frequency difference from the resonance is greater than 50 cm^{-1} in

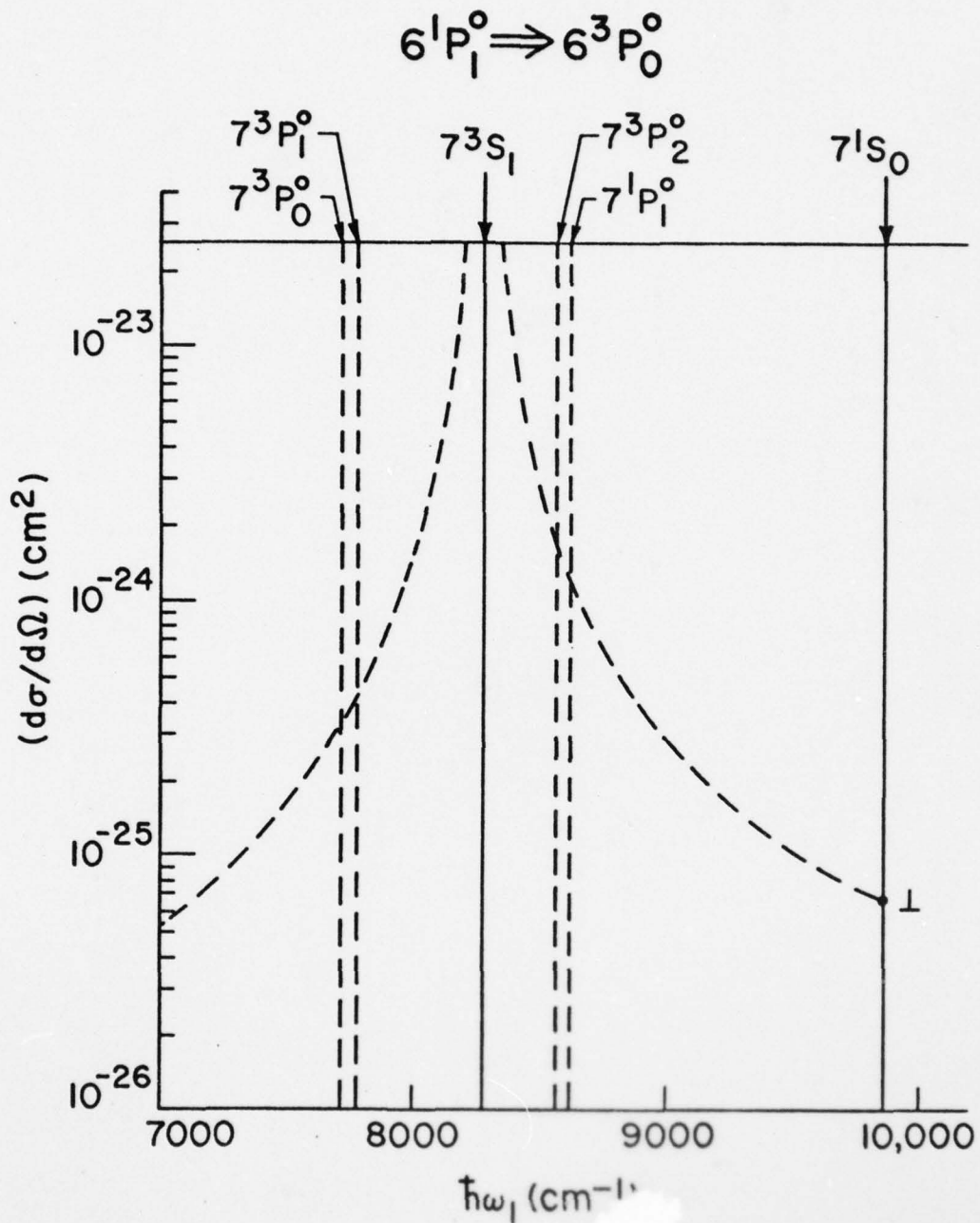


Fig. 9 -- ASRS cross-section vs. incident (trigger) photon energy $\hbar\omega_1$ for the Hg ($6^1P_1^0 \rightarrow 6^3P_0^0$) transition. Only depolarized (1) Raman scattering yields non-vanishing cross-section.

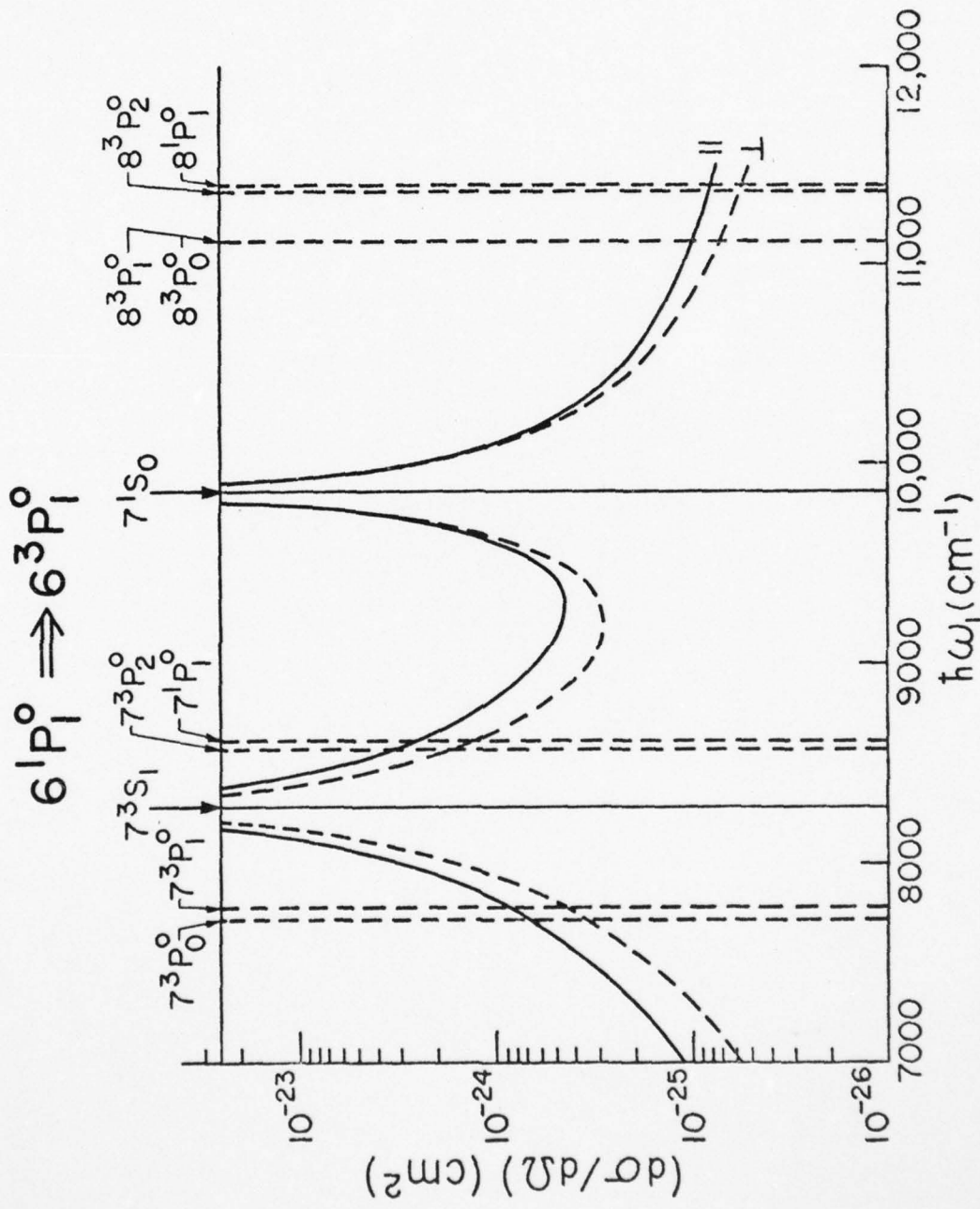


Fig. 10 -- ASRS cross-section vs. incident photon energy $\hbar\omega_1$ for the Hg ($6^1P_1^0 \Rightarrow 6^3P_1^0$) transition.

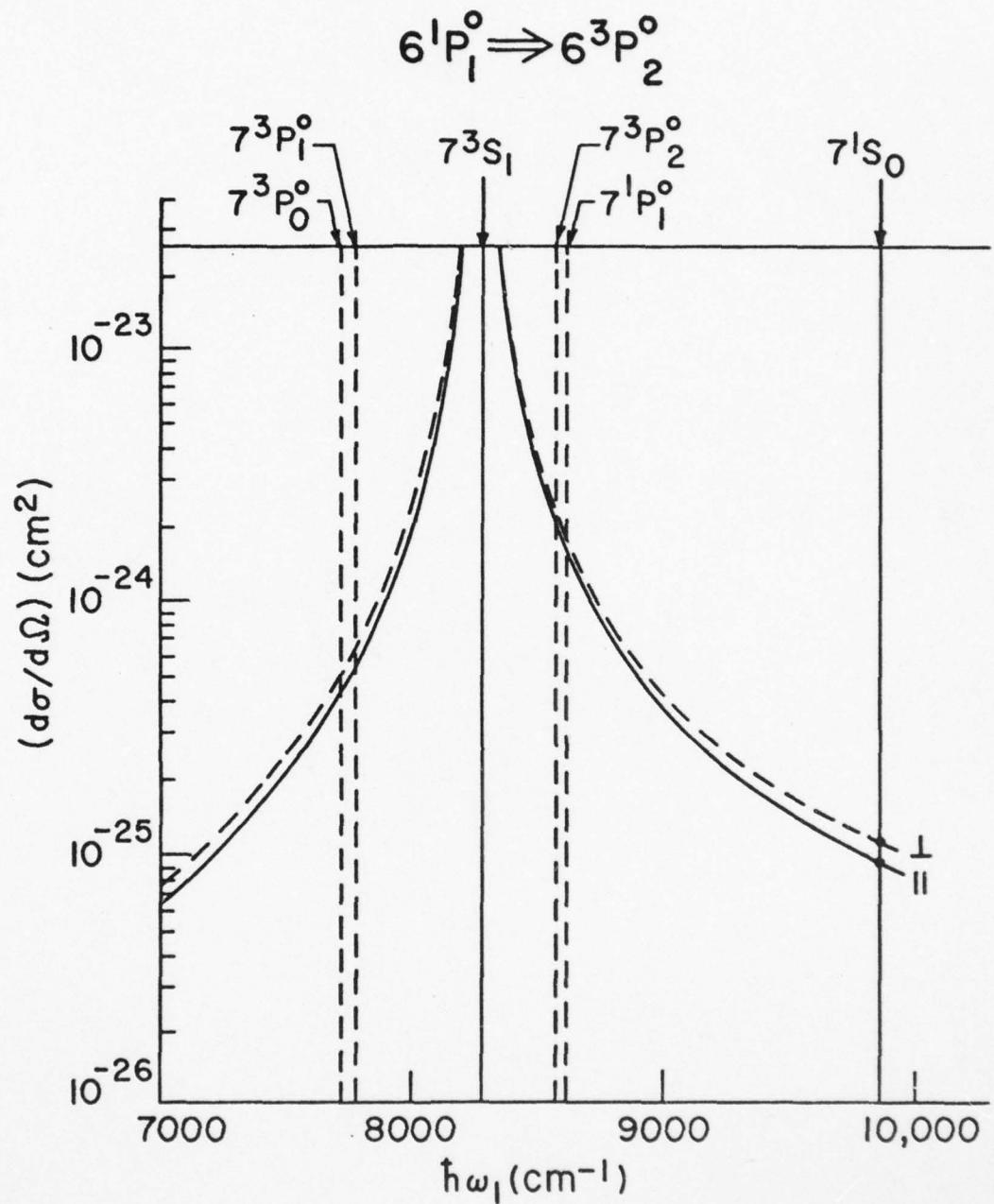


Fig. 11 -- ASRS cross-section vs. incident (trigger) photon energy $\hbar\omega_1$ for the Hg ($6^1P_1^0 \Rightarrow 6^3P_2^0$) transition. Polarized (||) and depolarized (\perp) scattering have comparable cross-sections.

these graphs, since smaller detuning must be properly described by resonance Raman and resonance fluorescence phenomena. However, it is interesting to note that both Fig. 9 and Fig. 11 show no enhancement from the 7^1S_0 state. This behavior is due to the angular momentum restrictions even though the incident photon has an absorption resonance at the transition frequency.

The polarization dependence of $(d\sigma/d\Omega)$ also reveals interesting results in Fig. 9 and Fig. 10. In Fig. 9 the Raman transition is only permitted for the depolarized case. The polarized case leads to $(d\sigma/d\Omega) = 0$ identically. This arises from the property of the $3j$ symbol factors in Eq. (4.3). Figure 10 shows the behavior of $(d\sigma/d\Omega)$ when two intermediate states can contribute significantly. The calculation reveals that the two states do not interfere with each other. Instead, the states simply contribute independently so that no cancellation of terms in Eq.(4.1) occurs. This behavior also results from the $3j$ symbol factors.

The ASRS cross-sections for $1.064 \mu\text{m}$ and $10.6 \mu\text{m}$ input wavelengths are summarized in Table III. The calculations for the $10.6 \mu\text{m}$ case include additional contributions from the 6^1S_0 , 6^1D_2 , 6^3D_2 , and 6^3D_1 states, but these terms are found to be small compared to the value obtained from the near-resonance approximation using Eq.(4.1). As expected the ASRS cross-sections at $10.6 \mu\text{m}$ are on the order of 10^{-28} cm^2 compared to 10^{-25} cm^2 at $1.064 \mu\text{m}$.

Table III

$(d\sigma/d\Omega)_{\text{ASRS}}$ AT 1.064 μm AND 10.6 μm
 FOR Hg ($6^1P_1^o \Rightarrow 6^3P_J^o$)

λ_1 (μm)	$ a\rangle$	λ_3 (μm)	$(d\sigma/d\Omega)_{\text{ASRS}}$ (cm^2)	Polarization
1.064	$6^3P_2^o$	0.5148	1.6×10^{-25}	
	$6^3P_1^o$	0.4157	4.6×10^{-25}	
	$6^3P_0^o$	0.3873	1.3×10^{-25}	⊥
10.6	$6^3P_2^o$	0.9116	1.4×10^{-28}	
	$6^3P_1^o$	0.6410	3.4×10^{-28}	
	$6^3P_0^o$	0.5758	4.5×10^{-29}	⊥

AD-A050 075

STANFORD UNIV CALIF EDWARD L GINZTON LAB
ENERGY STORAGE AND TWO-PHOTON EXTRACTION FROM METASTABLE STATES--ETC(U)
NOV 77 H KOMINE
GL-2753

F/G 20/5

F44620-74-C-0039

NL

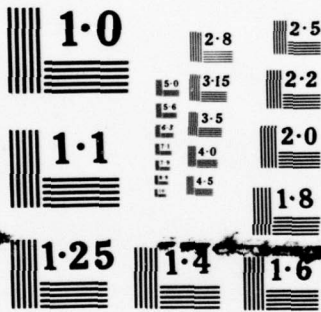
UNCLASSIFIED

AFOSR-TR-78-0077

2 OF 2
ADA
050075



END
DATE
FILMED
4 -78
DDC



NATIONAL BUREAU OF STANDARDS
MICROCOPY RESOLUTION TEST CHART

The cross-sections for TPE in the Hg ($6^1P_1^0 - 6^3P_J^0$) system can be calculated from Eq.(3.28) employing the same approximations used in the ASRS case. Unlike the ASRS case the energy level structure does not allow TPE resonance enhancement. Consequently the cross-sections are comparable to the non-resonant ASRS for the 10.6 μm input wavelength. The TPE cross-sections listed in Table IV suggest that the typical values for the TPE process in atomic systems are on the order of 10^{-29} to 10^{-28} cm^2 .

3. Experimental Requirements

The calculated curves of $(d\sigma/d\Omega)$ suggest that the ASRS gain enhancement is favorable for input wavelengths near 1 μm . From Table III the value of $(d\sigma/d\Omega)$ at 1.064 μm is equal to 4.6×10^{-25} cm^2 for the polarized case. Using Eqs.(3.26) and (3.30) the above cross-section yields an unsaturated ASRS gain coefficient of 9×10^{-3} cm/MW assuming that the linewidth is 0.1 cm^{-1} and the inversion density is 10^{16} cm^{-3} . Thus an input intensity of 100 MW/cm^2 at 1.064 μm yields an exponential gain of e^9 in a 10 cm length at the ASRS wavelength of 0.4157 μm . The results of the ASRS and TPE gain calculations are summarized in Table V. These estimates show that the ASRS infrared up-conversion in the Hg system may be demonstrated if the assumed population inversion density can be realized.

One possible method of achieving population inversion

Table IV

$(d\sigma/d\Omega)_{\text{TPE}}$ AT 1.064 μm AND 10.6 μm
 FOR Hg ($6^1P_1^o \Rightarrow 6^3P_J^o$)

λ_1 (μm)	$ a\rangle$	λ_2 (μm)	$(d\sigma/d\Omega)_{\text{TPE}}$ (cm^2)	Polarization
1.064	$6^3P_2^o$	15.94	2.0×10^{-31}	
	$6^3P_1^o$	1.902	7.1×10^{-29}	
	$6^3P_0^o$	1.423	2.3×10^{-31}	\perp
10.6	$6^3P_2^o$	1.101	5.8×10^{-29}	
	$6^3P_1^o$	0.7292	1.7×10^{-28}	
	$6^3P_0^o$	0.6460	1.5×10^{-29}	\perp

Table V

TWO PHOTON GAIN COEFFICIENTS* AT 1.064 μm AND 10.6 μm
 FOR Hg ($6^1P_1^o \rightarrow 6^3P_J^o$)

λ_1 (μm)	$ a\rangle$	δ_3^{ASRS} (cm/MW)	δ_2^{TPE} (cm/MW)	Polarization
1.064	$6^3P_2^o$	4.8×10^{-3}	5.8×10^{-6}	
	$6^3P_1^o$	9.0×10^{-3}	2.9×10^{-5}	
	$6^3P_0^o$	2.2×10^{-3}	5.3×10^{-8}	\perp
10.6	$6^3P_2^o$	1.3×10^{-4}	8.0×10^{-5}	
	$6^3P_1^o$	1.6×10^{-4}	1.0×10^{-4}	
	$6^3P_0^o$	1.7×10^{-5}	6.9×10^{-6}	\perp

* Evaluated with $Nu_o = 10^{16} \text{ cm}^{-3}$ and $\Gamma = 0.1 \text{ cm}^{-1}$.

in the mercury system involves optical pumping of the ground state atoms to the 7^1S_0 state by two-photon absorption followed by a radiative decay to the $6^1P_1^0$ level. This pumping scheme is shown in Fig. 8. The required TPA photon energy corresponds to 312.85 nm radiation, and the TPA cross-section is estimated to be $2.7 \times 10^{-20} \text{ cm}^2$ at an input intensity of 1 MW/cm^2 assuming a linewidth of 0.1 cm^{-1} . If the ground state density is 10^{17} cm^{-3} , 50 percent absorption in a 1 meter length cell requires an intensity of 3.7 MW/cm^2 . In order to achieve an inversion density of 10^{16} cm^{-3} using a pump beam area of 10^{-2} cm^2 the pump pulse must have at least 25 mJ at 312.85 nm in less than 0.67 microsecond. The use of shorter pulses increases the pump intensity, and greater than 50% absorption can be expected. However, the energy requirement can be relaxed by a factor of two at most. Furthermore, higher intensities may cause other nonlinear effects and reduce the TPA pumping efficiency.

The TPA optical pumping method is not an energy efficient process for creating a two photon gain medium, since it requires another laser for a pump source. However, it represents one possible approach in an effort to demonstrate the ASRS and TPE processes. Currently the requirement of 25 mJ of tunable ultraviolet laser output presents a major experimental problem. A high power dye laser system with second harmonic generation may provide a solution in the future.

C. ATOMIC IODINE TPE AND ASRS AMPLIFIER

1. Iodine System

Carman⁶ has investigated two photon energy extraction schemes using the metastable state of atomic iodine. The system was proposed by Vinogradov and Yukov⁸ based on a population inversion obtained between the $^2P_{1/2}$ metastable level and the $^2P_{3/2}$ ground state. Carman and Lowdermilk⁵³ have reported an observation of an anti-Stokes Raman gain in a flashlamp pumped active medium using an intense input beam of $1.064 \mu\text{m}$ radiation.

Figure 12 shows an abbreviated energy level diagram for atomic iodine. As indicated in the figure, two photon processes in iodine are far from being resonant for infrared and visible wavelength. According to Carman's analysis, the non-resonant character of the iodine system leads to two different modes of operation for optimum performance. One mode of operation is ASRS using a "trigger" photon energy which is small compared to the transition energy (7603 cm^{-1}). The long wavelength photon maximizes the energy gain per photon, since ASRS generates one photon for each absorbed trigger photon. In the second mode of operation the trigger photon energy is exactly equal to one half of the two-photon transition energy. Under this condition stimulated TPE dominates and the intensity growth is singular until saturation sets in. Since energy extraction by TPE is only limited by

IODINE ENERGY LEVELS

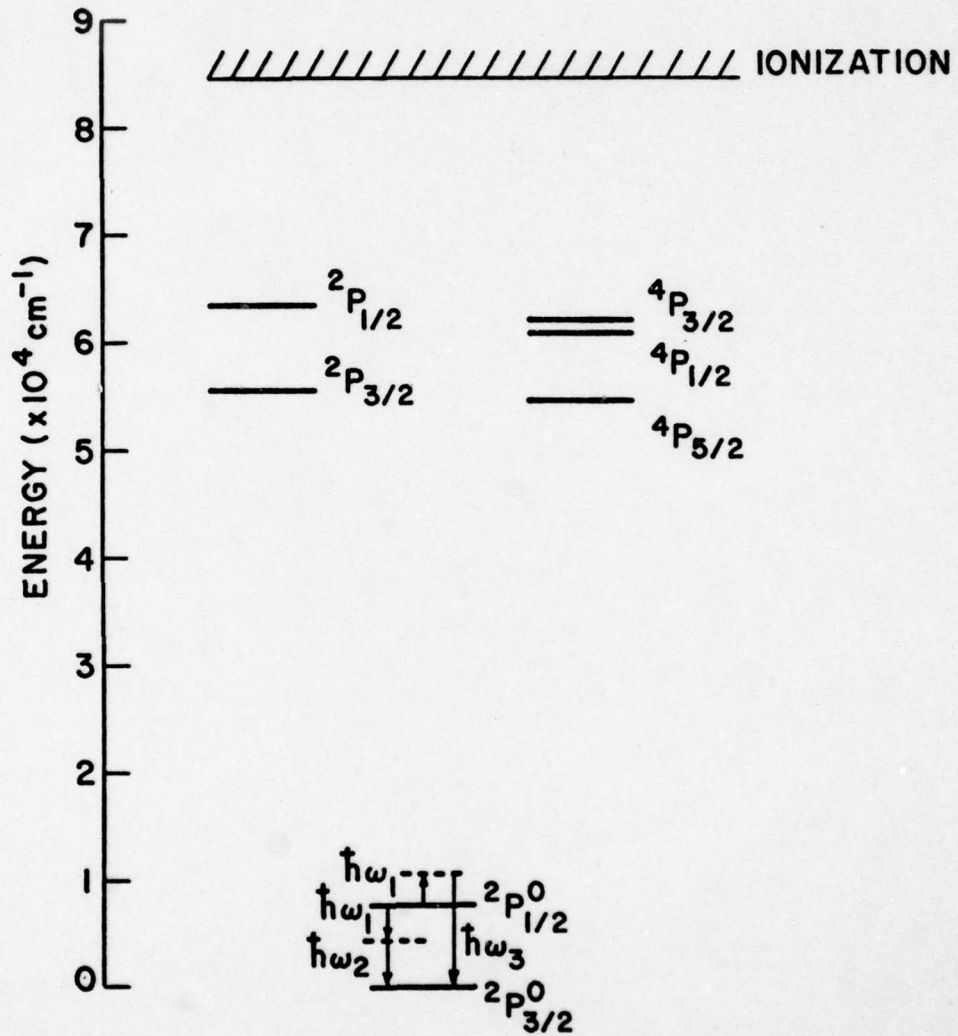


Fig. 12 -- Abbreviated energy level diagram of atomic iodine for TPE and ASRS amplifier.

the stored energy and not bounded by trigger intensity depletion which occurs in the ASRS process, the degenerate TPE extraction is considered more advantageous initially. However, four-wave mixing process also generates the ASRS signal which can eventually dominate over the TPE process.

One minor drawback of using the degenerate TPE process is that demonstrating a convincing evidence of stimulated TPE can be difficult experimentally. From the saturation characteristics of a degenerate TPE amplifier discussed in Chapter III a demonstration experiment requires a population inversion density in the range of 10^{17} to 10^{18} cm^{-3} in order to achieve significant signal amplification. The non-degenerate TPE amplification removes this experimental difficulty by amplifying a small injected signal at the complementary TPE frequency using an intense trigger field at ω_1 . However, before such experiments can be demonstrated the two-photon gain coefficient must be approximately determined in order to define experimental requirements. A semi-empirical procedure for calculating the non-resonant two photon gain coefficients is outlined in the next section.

2. Non-Resonant Two Photon Gain

The energy level structure of atomic iodine presents theoretical difficulties in calculating the non-resonant two photon gain coefficients due to a lack of knowledge of the relevant matrix elements. However, one can obtain rough

estimates of the cross-sections and the frequency dependence by considering a few intermediate states which are strongly coupled to the metastable state and the ground state. The formula for the cross-sections are given by Eq.(3.28), and the computational methods are given by Eqs.(C.20a) through (C.20e) in Appendix C.

The strongly coupled intermediate states are assumed to be the ${}^2P_{1/2}$ and ${}^2P_{3/2}$ states which lie at about $50,000 \text{ cm}^{-1}$ above the metastable ${}^2P_{1/2}^o$ state. For input photon energies much smaller than $50,000 \text{ cm}^{-1}$ the frequency dependence of the polarizability components in Eqs.(C.20a) and (C.20b) can be factored outside the summation over the intermediate states. Evaluating the $3j$ symbol factors for the polarized case yields the following approximate formulas for the cross-sections:

$$\left(\frac{d\sigma}{d\Omega}\right)_{1,2}^{\text{TPE}} \approx \frac{\omega_1 \omega_2^3}{16 \hbar^2 c^4} \left[\frac{1}{\omega + \omega_1} + \frac{1}{\omega + \omega_2} \right]^2 |R_k|^2 \quad (4.7)$$

and

$$\left(\frac{d\sigma}{d\Omega}\right)_{1,3}^{\text{ASRS}} \approx \frac{\omega_1 \omega_3^3}{16 \hbar^2 c^4} \left[\frac{1}{\omega - \omega_1} + \frac{1}{\omega + \omega_3} \right]^2 |R_k|^2 \quad (4.8)$$

where

$$|R_k|^2 = |\langle {}^2P_{3/2}^o || \vec{v} || {}^2P_{1/2} \rangle|^2 |\langle {}^2P_{1/2}^o || \vec{v} || {}^2P_{1/2} \rangle|^2 \quad (4.9)$$

The quantity ω in Eqs.(4.7) and (4.8) is the mean transition frequency between the intermediate states and the ${}^2P_{1/2}^o$ state. In deriving Eqs. (4.7), (4.8) and (4.9) the contributions from the ${}^2P_{1/2}$ and ${}^2P_{3/2}$ intermediate states are combined with the use of Eq.(D.9).

In TPE the frequency dependence can be simplified further since $\omega_1 \ll \omega$ and $\omega_2 \ll \omega$.

$$\left(\frac{d\sigma}{d\Omega}\right)_{1,2}^{\text{TPE}} \approx \left(\frac{\omega_1 \omega_2^3}{4 \hbar^2 c^4 \omega^2}\right) |R_k|^2 \quad (4.10)$$

Equations (3.43), (3.44), and (4.10) also lead to a simple expression for the photon flux gain coefficient given by

$$\beta \approx \omega_1 \omega_2 \left(\frac{N u_o}{\Gamma}\right) \left(\frac{8 \pi^2}{\hbar^2 \omega^2 c^2}\right) |R_k|^2 \quad (4.11)$$

Equation (4.11) shows that the photon flux gain coefficient peaks at the degenerate frequency $\omega_1 = \omega_2 = \omega_o/2$. For non-degenerate ($\omega_1 \neq \omega_2$) cases β decreases symmetrically about the peak. This behavior indicates that the maximum extraction rate per unit length occurs at the degenerate frequency.

The frequency dependence of $(d\sigma/d\Omega)$ in Eq. (4.8) gives a relationship between the reduced matrix element product term $|R_k|^2$ and the experimentally measurable scattering

cross-section. Therefore, accurate estimates of $(d\sigma/d\Omega)$ may be obtained once $|R_k|^2$ is determined from Eq.(4.10) using experimentally measured values of $(d\sigma/d\Omega)$ at certain frequencies. Unfortunately, such data are not available in the literature at the present time.

An alternative to the above semi-empirical method must rely on more approximations in Eq.(4.9). One approach consists of evaluating the reduced matrix elements in terms of the oscillator strength.³⁹ Equation (D.3) of Appendix D gives the relationship:

$$|\langle \gamma J \| \vec{\mu} \| \gamma' J' \rangle|^2 = (2J+1) f(\gamma J \rightarrow \gamma' J') (ea_0)^2 \left(\frac{R}{\bar{\nu}} \right) \quad (4.12)$$

where R is the Rydberg constant, and $\bar{\nu}$ is the transition frequency in cm^{-1} . For strongly coupled transitions the oscillator strengths are on the order of unity. This approximation yields the maximum value of $|R_k|^2$.

$$|R_k|_{\text{max}}^2 \approx 35(ea_0)^4 \quad (4.13)$$

The numerical computations of the ASRS and TPE cross-sections and the gain coefficients based on Eq.(4.13) are only rough estimates, but they provide an order of magnitude reference for experimental measurements as well as the largest values that can be expected. Table VI lists the approximate values of $(d\sigma/d\Omega)$ and δ at various wavelengths. The intensity

Table VI



($d\sigma/d\Omega$) AND INTENSITY GAIN COEFFICIENT δ^*

Anti-Stokes Raman Scattering (ASRS)			
$\lambda_1 (\mu\text{m})$	$\lambda_3 (\mu\text{m})$	($d\sigma/d\Omega$) (cm^2)	δ_3 (cm/MW)
10.6	1.17	2.9×10^{-30}	4.5×10^{-6}
2.63	0.877	2.9×10^{-29}	6.3×10^{-6}
1.91	0.778	5.9×10^{-29}	7.2×10^{-6}
1.064	0.588	2.6×10^{-28}	1.0×10^{-5}
0.532	0.379	2.5×10^{-27}	2.0×10^{-5}
0.355	0.279	1.5×10^{-26}	4.4×10^{-5}
0.266	0.221	1.0×10^{-25}	1.4×10^{-4}
Two-Photon Emission (TPE)			
$\lambda_1 (\mu\text{m})$	$\lambda_2 (\mu\text{m})$	($d\sigma/d\Omega$) (cm^2)	δ_2 (cm/MW)
10.6	1.50	1.6×10^{-30}	4.1×10^{-6}
2.60	2.66	1.2×10^{-30}	2.4×10^{-6}
1.91	4.24	3.9×10^{-31}	1.4×10^{-6}

* Calculated with $N_{u_0} = 10^{16} \text{ cm}^{-3}$ and $\Gamma = 0.1 \text{ cm}^{-1}$

gain coefficients are based on $N u_0 = 10^{16} \text{ cm}^{-3}$ and $\Gamma = 0.1 \text{ cm}^{-1}$. A comparison of the TPE cross-sections in Table VI for iodine and Table IV for mercury shows one to two orders of magnitude smaller values for the iodine system. The difference is partly due to a more pronounced non-resonant character in iodine, but the primary cause is the smaller TPE frequencies generated in the iodine system.

3. Experiment

The experimental studies on the iodine system included population inversion in the metastable state and several attempts to demonstrate superfluorescent anti-Stokes Raman scattering. Stimulated ASRS has not been observed yet, but the experimental results suggested improvements for future experiments.

The present experiment employed photolytic production of the metastable iodine atoms from n-iodoheptafluoropropane ($n\text{-C}_3\text{F}_7\text{I}$) molecules. The fourth harmonic of a Nd:YAG laser system provided the photolysis radiation at 266 nm which is near the peak of the $n\text{-C}_3\text{F}_7\text{I}$ absorption band. Figure 13 schematically shows the pumping method.

The experimental apparatus consisted of a 55 cm length cell filled with 10 to 20 torr of $n\text{-C}_3\text{F}_7\text{I}$. The cell was irradiated with a loosely focussed beam of 266 nm radiation using a 1 m focal length lens. The focal plane of the lens

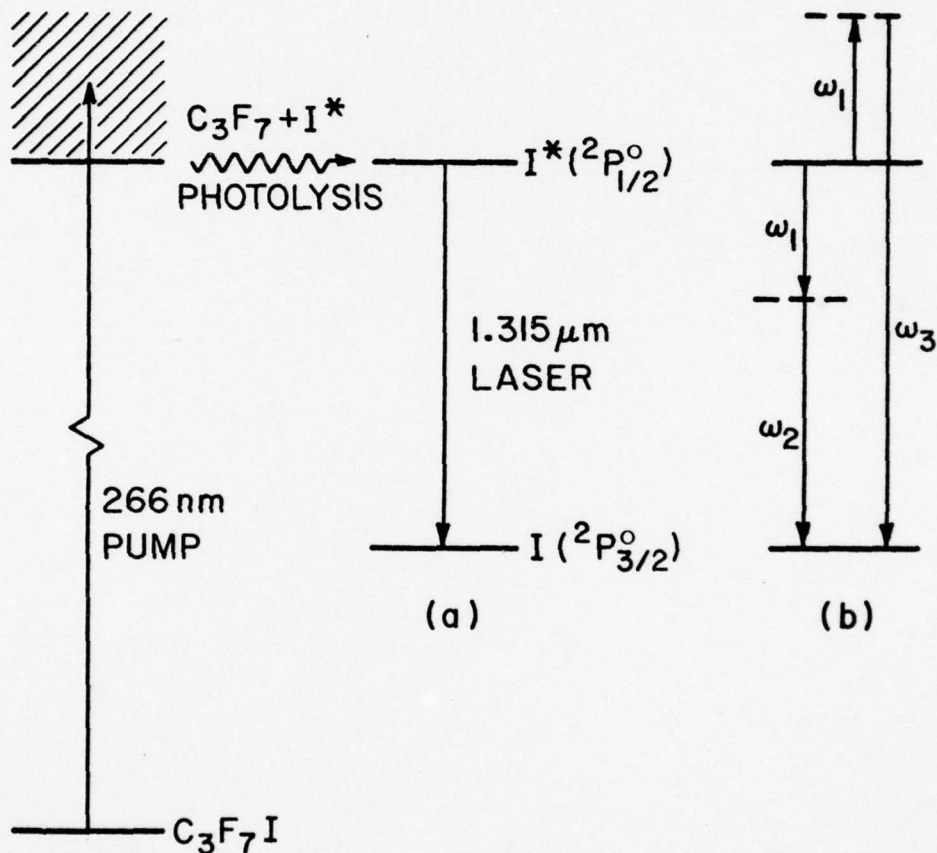


Fig. 13 -- Photolytic production of population inversion in atomic iodine system: (a) Photolysis of C_3F_7I with 266 nm radiation yields excited iodine atoms, and population inversion leads to optical gain at the 1.315 μm transition; (b) schematic TPE and ASRS amplification and energy extraction in the iodine system.

coincided with the midpoint of the cell, and the beam diameter at the cell windows was 1 mm. The cell absorbed all of pump radiation initially. However, a continued pumping with 5 nsec pulses of 266 nm radiation with energies of up to 5 mJ per pulse eventually exhausted the molecules after about 10^3 shots.

In order to verify population inversion an optical resonator cavity was set up to oscillate the atomic iodine transition at $1.315 \mu\text{m}$. Figure 13a indicates the observed transition. The cavity consisted of a 1m-curvature high reflectance mirror at $1.315 \mu\text{m}$ and a flat 95.3% reflectance mirror at $1.32 \mu\text{m}$ separated by 90 cm. The threshold pump energy was 0.67 mJ with an oscillation build-up time of about 200 nsec. At a pump energy of 1.9 mJ, the output energy was $67 \mu\text{J}$ indicating an energy conversion of 3.5 percent. Such small conversion efficiency was not surprising since no attempt was made to properly mode-match the pump beam to the resonator cavity.

The output energy measurements above threshold showed a conversion efficiency of 5.7 percent of the pump energy in excess of the threshold value. The photon conversion efficiency is obtained by multiplying the energy efficiency by the ratio of the pump photon energy to the $1.315 \mu\text{m}$ photon energy. The calculation yields a photon conversion of 28 percent. Since only half of the energy stored in the

inverted level is extracted out, the actual photolysis efficiency is 56 percent.

The population inversion densities achieved in the photolytically pumped medium may be estimated from the threshold inversion density. Since the round trip gain equals the loss at threshold, $\sigma \Delta n l \geq 5 \times 10^{-2}$ must hold. Using a cross-section of $1.78 \times 10^{-18} \text{ cm}^2$ and an interaction length of 10 cm, the threshold inversion density is $\Delta n \geq 3 \times 10^{15} \text{ cm}^{-3}$.

The inversion density can also be estimated from the threshold pump energy density and the photolysis efficiency. The calculation gives $\Delta n \approx 6 \times 10^{15} \text{ cm}^{-3}$ in a reasonable agreement with the above estimate. Therefore, a 2 mJ pump pulse creates a population inversion density of

$$\Delta n \approx 1.4 \pm 0.4 \times 10^{16} \text{ cm}^{-3} \quad . \quad (4.14)$$

In an attempt to observe stimulated ASRS in the inverted iodine system a trigger pulse of $\sim 500 \text{ MW/cm}^2$ at $1.064 \text{ } \mu\text{m}$ probed the 10 cm long excited region pumped by a 2 mJ pulse. Absence of superfluorescent signal signified that the intensity gain coefficient is less than $4 \times 10^{-3} \text{ cm/MW}$ at an inversion density of 10^{16} cm^{-3} . This result is consistent with the calculated value of $\delta \approx 4 \times 10^{-5} \text{ cm/MW}$ using a linewidth of 0.74 GHz. In another experiment, a trigger pulse of $\sim 150 \text{ MW/cm}^2$ at $0.532 \text{ } \mu\text{m}$ probed the

inverted medium. A negative result indicated that $\delta < 10^{-2}$ cm/MW which is consistent with the calculated $\delta \approx 0.8 \times 10^{-4}$ cm/MW.

The experimental data show that the single pass gain, $\delta I l$, must be increased by at least two orders of magnitude in order to verify the calculated values of δ . Since trigger intensities are limited to ~ 1 GW/cm², the inversion density and the interaction length must be increased. Realistic estimates of inversion density and length are $\Delta n \sim 10^{17}$ cm⁻³ and $l \sim 100$ cm for existing flashlamp pumped iodine laser amplifiers reported in the literature.¹⁰ These estimates suggest that a demonstration of superfluorescent ASRS output may be marginally feasible with the currently available technology. However, a demonstration of ASRS amplification of an injected signal appears to be much more probable.

Similarly, a stimulated TPE amplifier has a greater probability of a successful operation if an injected signal at the TPE frequency is used. Table VI indicates that a single-pass exponential gain of e^4 at 1.5 μ m may be expected for a 10.6 μ m trigger input at 1 GW/cm², provided that $\Delta n = 10^{17}$ cm⁻³ and $\Gamma = 0.1$ cm⁻¹. A similar calculation yields a gain of $e^{1.4}$ at 4.24 μ m for a 1.91 μ m trigger input at 1 GW/cm².

Stimulated Raman effect in molecular hydrogen gas at 20 atmospheres of pressure has recently generated more than 100 mJ of 1.91 μ m radiation from a 1.064 μ m source.

A pulse length of ~ 7 nsec and a beam area of 10^{-2} cm² can easily reach 1 GW/cm² intensity levels. Thus, a successful demonstration of stimulated TPE amplifier requires a 10^{17} cm⁻³ inversion density in a 1 m long active medium and an injection signal at 4.24 μ m. These requirements are not impossible, but they are not without challenging experimental problems.

This chapter has illustrated two types of two-photon gain medium. The discussion on the atomic mercury system described the polarization properties and the near-resonance enhancement of ASRS gain. An example of a system with non-resonant ASRS and TPE was presented with a review of the proposed iodine system. Feasibility studies on each system led to experimental requirements that can be achieved with the existing technology. However, the requirements for stimulated TPE amplification showed that a reasonable probability of success exists only at the very limit of energy storage in a metastable system.

CHAPTER V

CONCLUSION

This work has contributed to a further understanding of the limitations of energy storage in metastable states and the two photon energy extracion schemes for generating high power laser outputs.

The experimental studies on the decay properties of the metastable mercury excimer system identified an intrinsic non-radiative deactivation mechanism that ultimately limits the useful lifetime and the energy storage capacity of the metastable states. The loss mechanism was determined to be mutual quenching of excited metastable species by two-body collisions. Thus, the decay mechanism directly tied lifetime and capacity as interdependent quantities. The measured quenching rate constant suggested that an inversion density on the order of 10^{17} cm^{-3} and a lifetime of 0.1 microsecond are the practical limits of energy storage in the mercury excimer system. Furthermore, because of the intrinsic nature of the decay mechanism other metastable systems are likely to be governed by similar storage limitations.

The discussion of two photon energy extraction including saturation of the population inversion extended the theory of two photon amplificaion for the case of an ideal two-photon gain medium. The exact analytical solutions to the

steady-state amplification equations quantitatively characterized the extraction efficiency and saturation behavior of an ideal two-photon amplifier. The amplifier performance could then be evaluated on the basis of trigger intensity and a gain parameter, G , which depends only on the trigger photon frequency and the parameters of the medium. One important result indicated that G greater than unity is a necessary condition for efficient extraction by amplification of stimulated two-photon emission. However, for G less than unity efficient amplification at the complementary frequency to the trigger frequency could still be achieved if the trigger photon flux is sufficiently larger than the maximum flux that can be extracted.

Calculations of the gain parameter showed that $G > 1$ may be achieved if the population inversion densities of greater than 10^{17} cm^{-3} can be realized. This implies that efficient TPE gain medium exists only at the maximum storage limit of a vapor medium consisting of excited metastable species.

The analysis of extraction efficiency and saturation did not include the effects of competing nonlinear processes. In real systems ASRS and four-wave mixing can be significant and should be included in the extraction calculations. However, since the coupled nonlinear equations cannot be solved analytically, such calculations require computer numerical

methods.⁵⁵ Therefore, the ideal extraction calculations provide a helpful guide in understanding the maximum performance that can be expected of a two-photon amplifier.

The feasibility analysis of the proposed gain media using atomic mercury and iodine showed that experimental requirements are feasible but not without careful optimization of the currently available pumping methods and trigger laser sources. Since G is of the order of unity for both systems under optimum conditions, only moderate amplification and extraction can be expected. Thus, an efficient two photon gain medium remains to be discovered in the future. Nevertheless, a successful demonstration in Hg or I would be interesting not only from an application point of view but also as a new physical effect.

APPENDIX A

Optically pumped Hg₂ studies

H. Komine and R. L. Byer

Edward L. Ginzton Laboratory, W. W. Hansen Laboratories of Physics, Stanford University, Stanford, California

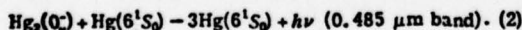
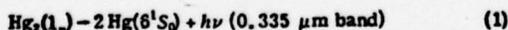
(Received 3 May 1977)

The continuous emission bands of molecular mercury at 0.335 and 0.485 μm are excited in a pure mercury vapor by direct optical pumping of the weakly bound ground state molecules with a 5 nsec pulse of intense 0.266 μm radiation in order to study the radiative and collisional properties of the excited molecules at densities between 10^{14} and 10^{17} cm^{-3} . Fluorescence time history of both bands are empirically analyzed in terms of dynamics governing the excited molecules. The analysis includes a density-dependent nonexponential decay caused by bimolecular excimer quenching with a measured rate constant of $k_{\text{qu}} = 2.1 \times 10^{-10}$ $\text{cm}^3 \text{sec}^{-1} \text{molecule}^{-1}$. Because of interest in the mercury system as a potential laser medium, estimates of gain coefficients are derived from fluorescent power measurements. However, transmission measurements of the excited medium at 0.325 and 0.4416 μm show significant net loss due to excited state absorption with an estimated absorption cross section on the order of 10^{-17} cm^2 at 0.325 μm . Energy storage limitations implied by the bimolecular excimer quenching is also examined.

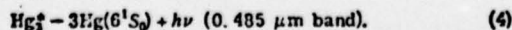
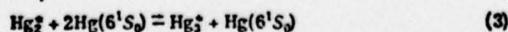
I. INTRODUCTION

The visible and the ultraviolet continuous emission bands of molecular mercury have been investigated¹⁻⁴ as potential laser transitions after such possibility was pointed out as early as 1960.⁵ The Hg₂ system has been considered as a potential electric discharge pumped laser medium capable of efficiently generating high output powers at wavelengths of interest for laser fusion and photochemical applications. Although stimulated emission has not yet been demonstrated, recent developments have included gain measurements in the ultraviolet,³ electric discharge pumping studies of a high pressure mercury vapor,⁴ and spectroscopic and kinetic analysis of the excited molecular states.⁶⁻⁸

The molecular emission bands considered for laser action are due to bound-continuum transitions that originate from the lowest bound excited states and terminate on the repulsive part of the ground state where the molecules dissociate rapidly. The traditional assignment of the ultraviolet band centered at 0.335 μm is the $^3\text{I}_u - ^1\Sigma_g^+$ transition as indicated in Fig. 1, while that of the visible band centered at 0.485 μm is the $^3\text{O}_u - ^1\Sigma_g^+$ transition induced by collisions with mercury atoms.⁹ The following reactions describe the transitions:



Based on more recent extensive studies of the mercury fluorescence bands, Drullinger, Hessel, and Smith⁷ suggest that transitions due to an excited mercury trimer complex may be responsible for the 0.485 μm band emission at mercury densities greater than 5×10^{17} cm^{-3} and temperatures above 575 $^\circ\text{K}$. According to their kinetic results the excited trimers, Hg₃^{*}, exist in thermal equilibrium with the excited dimers, Hg₂^{*}, and radiate by dissociating into atoms as described by the following reactions:



Because a thermal equilibrium relationship exists be-

tween Hg₂^{*} and Hg₃^{*}, the excited dimers and trimers are collectively referred to as excimers in this paper, and the distinction is asserted where possible or necessary.

The early investigators^{10,11} and Drullinger *et al.*⁷ have also studied the broad continuous absorption band associated with the $^1\Sigma_g^+ - ^3\text{I}_u$ transition. The absorption due to the weakly bound ground state extends from about 0.320 μm to the 0.2537 μm resonance line and varies as the square of the atomic mercury density.¹⁰ At mercury densities greater than 10^{17} cm^{-3} where resonance line pumping cannot be used for a large volume excitation, the optical pumping of the ground state molecules directly creates vibrationally excited 1_u molecules.

We have used this molecular optical pumping method to investigate the mercury excimer system as a potential laser medium by directly creating excimers at densities between 10^{14} and 10^{15} cm^{-3} with a 5 nsec pulse of 0.266 μm radiation as schematically shown in Fig. 1. Some of the radiative and collisional properties of the excimers at these densities are studied by monitoring fluorescence time history and by probing the excited medium at 0.325 and 0.4416 μm with a HeCd laser. Our experimental results show net absorption at these probe wavelengths and

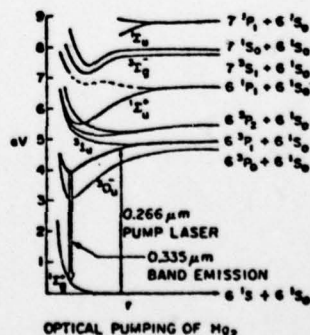


FIG. 1. Partial potential curves of Hg₂ molecule according to Mrozowski.⁹ The excited 1_u molecules are created by optical pumping of the ground state molecules with 0.266 μm radiation.

indicate evidence of bimolecular quenching of excimers causing a faster decay at higher excimer densities. Although stimulated emission due to excimers is absent in the optically pumped mercury excimer system, the results of our study may aid in the further understanding of the dynamics of the mercury excimer system and other potential excimer laser systems.

II. EXPERIMENTAL APPARATUS

Figure 2 shows a schematic of the experimental apparatus. Our optical pump source consisted of an electro-optic Q-switched Nd:YAG laser with an unstable resonator cavity configuration followed by two stages of second harmonic generator crystals to produce 0.266 μm radiation from the 1.064 μm laser. The unstable resonator Nd:YAG laser produced up to 200 mJ of near diffraction limited output with a 6.3 mm diameter annular beam cross section in a 10 nsec pulse at 10 pulses per second.¹² The 1.064 μm output was doubled in a Type II angle phase-matched 25 mm long deuterated potassium dihydrogen phosphate (KD*P) to generate up to 30 mJ of 0.532 μm radiation. The 0.532 μm beam was transmitted through a heat absorbing glass filter to eliminate the 1.064 μm radiation. After a 2:1 beam reducing telescope, the collimated 3 mm diameter 0.532 μm beam was doubled again in a Type I angle phase-matched 25 mm long ammonium dihydrogen phosphate (ADP) crystal to generate 0.266 μm output of up to 10 mJ in a 5 nsec pulse. The 0.266 μm beam was separated from the second harmonic by Brewster angle quartz prisms and directed to a cell containing mercury vapor. The collimated 0.266 μm beam has an effective area of 2×10^{-2} cm^2 , yielding a maximum peak intensity of 100 MW/cm^2 . The pumping level was normally held to less than 5 mJ per pulse at 10 pulses per second because of induced surface scatter loss to the ADP crystal by the 0.266 μm radiation at higher pumping levels.

The mercury cell and oven apparatus consisted of a quartz cell with a sidearm mercury reservoir inside an oven of the same shape with independent temperature controls for each section of the cell. The cell tube had an inner diameter of 1.4 cm and a length of 90 cm with

optically contacted fused silica Brewster windows at the ends of the tube. Pure distilled mercury was introduced into the sidearm tube via careful cleaning and bake-out procedures since purity and cleanliness have been recognized to be essential.⁶ The cell and sidearm sections and all glass tubing used in the filling procedure were chemically cleaned with chromic acid and rinsed with distilled water several times before treated with spectroscopic grade methanol and dry nitrogen gas. The entire filling apparatus was torched and the cell and sidearm sections were baked in the oven at over 700 and 400 $^{\circ}\text{C}$, respectively, for three hours under a vacuum of 2×10^{-6} torr. Pure natural isotopic mercury of instrument grade was introduced into the filling apparatus under one atmosphere pressure of dry nitrogen and the apparatus was sealed and evacuated with another bake-out sequence. The mercury droplets were slowly distilled into the sidearm until 2-3 g were transferred and the sidearm was sealed.

Several thermocouples monitored the vapor temperature at various positions along the cell and sidearm. The mercury vapor density was controlled by a section of the sidearm having the lowest temperature from which the density was calculated using the vapor pressure vs temperature data.¹³ The sidearm temperature was maintained to within 1 $^{\circ}\text{C}$, and the calculated density was estimated to be accurate to 5%. The cell was operated at a Hg vapor density of $1-5 \times 10^{18}$ cm^{-3} at pressures in the 100-400 torr range. The cell temperature was maintained at 570 ± 5 $^{\circ}\text{C}$ in order to prevent vapor condensation in the cell and to enhance the ultraviolet band intensity.

The pump radiation is absorbed by the Hg vapor according to Lambert's law, and the ratio of the transmitted intensity to the incident intensity is given by $I(l)/I(0) = \exp(-KN^2l)$, where N and l are the Hg density and the cell length, respectively. K is a wavelength dependent parameter which has a value of 7.27×10^{-40} cm^5 at 0.266 μm .⁷ Experimentally, 50% of the pump energy is absorbed at $N \approx 3.4 \times 10^{18}$ cm^{-3} .

Fluorescence from the cell could be detected either

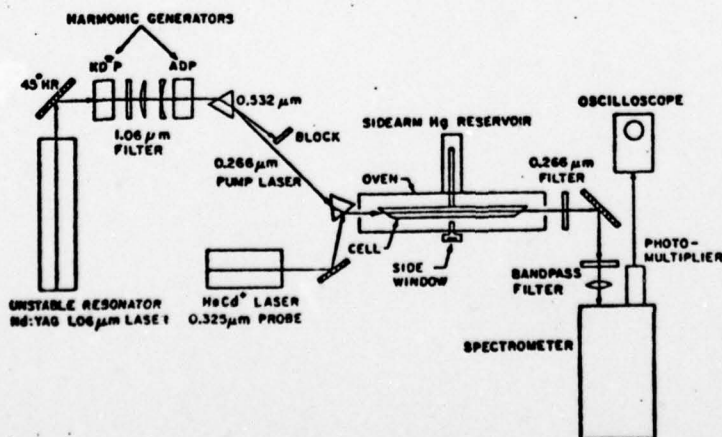


FIG. 2. Schematic layout of the optical pumping experiments.

from the ends or through a side hole at the middle of the cell for observation perpendicular to the pump beam. The cell temperature at the middle was between 350 and 360 °C because of the oven construction geometry. The side fluorescence detection arrangement included a Corning glass 7-51 filter and a 5 nm wide 334 nm Hg line filter for the ultraviolet band and a 5 nm wide 488 nm spike filter for the visible band. The fluorescence was detected by an RCA 7265 photomultiplier tube with S-20 response, and the output signal was monitored on a Tektronix 556 oscilloscope with 1A5 wide band preamplifier. For detection of wavelengths outside the S-20 response range, an RCA 6903 photomultiplier with S-13 response for shorter uv wavelengths was used. Germanium and silicon detectors were used for infrared and visible atomic emission. Fluorescence detection from one end of the cell was arranged with the same filters and a 1 m Chromatix 1800 l/mm grating spectrometer for additional spectral filtering as shown in Fig. 2.

The band spectra measurements were made using an arrangement similar to the above without the 5 nm wide band pass filters. The spectral scan data were taken with a laboratory built "box car" integrator and Hewlett-Packard chart recorder. In fluorescence time history measurements which did not require high spectral resolution, the filtering consisted of a 60° quartz prism for spatial separation followed by a 20 cm J-Y holographic monochromator with 2 nm resolution.

A series of experiments for probing net gain or loss due to the excimers was conducted by measuring the transmission of the excited medium with a Liconix Model 301 cw HeCd laser operating at 0.4416 and 0.325 μm. The probe laser had a TEM₀₀ mode beam diameter of 0.9 mm and a beam divergence of 0.5 mrad. The probe beam was combined and overlapped with the pump beam by reflecting off the output surface of the second prism as shown in Fig. 2. Initial experiments with focused pump beam showed severe beam steering effects of the

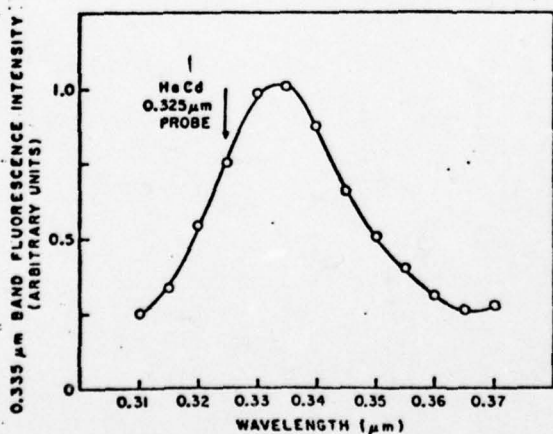


FIG. 3. 0.335 μm band fluorescence spectra at Hg density of $2.3 \times 10^{18} \text{ cm}^{-3}$ and 570 °C vapor temperature. An arrow indicates the position of the 0.325 μm probe wavelength used in the excimer optical transmission experiment.

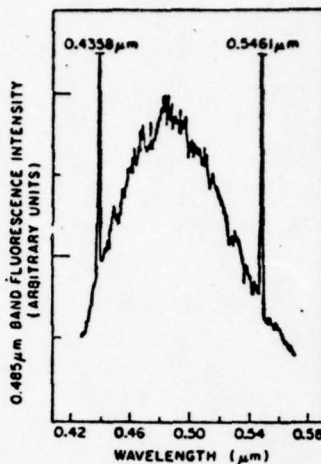


FIG. 4. 0.485 μm band fluorescence spectra at a Hg density of $3.1 \times 10^{18} \text{ cm}^{-3}$ and 570 °C vapor temperature. Two strong atomic superfluorescent emission lines at 0.4358 and 0.5461 μm are also observed.

probe beam lasting for about one millisecond. A 0.6328 μm HeNe probe beam also showed the same behavior, and the cause is attributed to thermal refractive index variation induced by the excited medium. The beam steering problem was eliminated by carefully overlapping the probe beam with the collimated unfocused pump beam.

III. RESULTS AND DISCUSSION

A. Fluorescence spectra

The ultraviolet and the visible band fluorescence spectra excited by direct optical pumping of Hg₂ molecules exhibited the well known features of the emission bands.¹⁴ Figure 3 shows the ultraviolet band which has a peak at 0.335 μm with an estimated half maximum width of 30 nm. Figure 4 shows the visible band before photomultiplier response correction. The band has a peak near 0.485 μm with a half maximum width of 100 nm, but the photomultiplier response correction shifts the true peak wavelength to a value between 0.50 and 0.52 μm. Several small dips in the visible band spectra occur at the same positions in repeated scans. In particular, the dips near 0.47–0.48 and 0.53 μm appear to be suggestive of absorption. The origin of these structures, however, is unknown at this time.

The spectral scans in the ultraviolet to 0.2 μm showed no evidence of any other molecular emission bands, but did show several fluorescent emission lines due to neutral atomic mercury transitions. Further scans in the visible and infrared revealed additional atomic emission lines. Twelve of the nineteen observed emission lines showed stimulated amplification of spontaneous fluorescence emission or superfluorescence. The superfluorescence and the normal spontaneous atomic mercury transitions are listed in Table I. The mechanisms of atomic population inversion and the superfluorescent laser action have been investigated in detail, and the results are pub-

TABLE I. Observed atomic emission lines.

λ (μm)	Transition	Remark	λ (μm)	Transition	Remark
0.2967	$6^3P_0 - 6^3D_1$	(a)	0.4047	$6^3P_0 - 7^3S_1$	(a)
0.3126	$6^3P_1 - 6^3D_2$	(a)	0.4078	$6^3P_1 - 7^1S_0$	(a)
0.31316	$6^3P_1 - 6^3D_1$	(a)	0.4358	$6^3P_1 - 7^3S_1$	(d)
0.31318	$6^3P_1 - 6^3D_2$	(a)	0.5461	$6^3P_2 - 7^3S_1$	(b)*
0.3341	$6^3P_2 - 6^3S_1$	(a)	0.5770	$6^1P_1 - 6^3D_2$	(c)
0.3650	$6^3P_2 - 6^3D_3$	(b)*	0.5791	$6^1P_1 - 6^1D_2$	(c)
0.3655	$6^3P_2 - 6^3D_2$	(c)	1.1287	$7^3S_1 - 7^3P_2$	(b)
0.36629	$6^3P_2 - 6^3D_1$	(c)	1.357	$7^1S_0 - 7^1P_1$	(b)
0.36833	$6^3P_2 - 6^1D_2$	(c)	1.367	$7^3S_1 - 7^3P_1$	(b)
			1.395	$7^3S_1 - 7^3P_0$	(b)*

*Normal spontaneous fluorescence only.

°Superfluorescent emission (* dominant laser lines).

*Superfluorescent emission appeared only with focused pump radiation.

°Superfluorescent emission observed only at low pump energies.

lished elsewhere.¹⁵ A brief discussion of the pumping mechanisms is given in Sec. III F following the results of the excimer studies, since the excimers appear to participate in the production of high lying atomic states.

The total fluorescence energy emitted by the atomic transition was less than 1% of the pump energy, and most of the absorbed pump energy was radiated by the molecular fluorescence. We have measured the absolute fluorescence yield of the visible band using a calibrated photomultiplier. The measurements were made at the side fluorescence window with atomic Hg densities of $N \approx 4.0 \times 10^{18} \text{ cm}^{-3}$ and $N \approx 4.4 \times 10^{18} \text{ cm}^{-3}$ at a vapor temperature of $355 \pm 1^\circ \text{C}$. The measured pump absorption was 0.015 cm^{-1} at $N \approx 4.0 \times 10^{18} \text{ cm}^{-3}$ and 0.016 cm^{-1} at $N \approx 4.4 \times 10^{18} \text{ cm}^{-3}$ for a pump energy density of 30 mJ/cm^2 . Under these conditions, the measured fluorescence yield for the visible band was between 0.8 and 1.0. The visible band intensity dominated over the ultraviolet band intensity by a ratio of 10 ± 2 to 1. The relative band intensities were reversed, however, when the fluorescence was detected from the excited vapor at 570°C . The effect of the vapor temperature on the relative band intensities is in agreement with the findings of Drullinger *et al.*⁷

B. Fluorescence time history

In order to understand the dynamics of the mercury excimer system, we have experimentally analyzed the time history of the excimer fluorescence bands at various Hg densities between 1 and $4.5 \times 10^{18} \text{ cm}^{-3}$ at temperatures of $355 \pm 1^\circ \text{C}$ and $570 \pm 5^\circ \text{C}$. Figures 5 and 6 illustrate the representative oscilloscope traces of the fluorescence time history of the 0.335 and the 0.485 μm bands. A comparison between the 0.335 μm band data and the 0.485 μm band data shows that the two fluorescence intensity signals differ initially but become similar after an elapsed time of 0.5 μsec .

The 0.335 μm band fluorescence time history consists

of a fast "spike" coincident with the pump pulse and a slowly decaying component immediately following the initial "spike". Figure 5(a) shows these features at a Hg density of $3.4 \times 10^{18} \text{ cm}^{-3}$ with 570°C vapor temperature. The width of the "spike" is limited by the 10 nsec time resolution of our detection system. The same features appeared at all wavelengths between 0.32 and 0.36 μm . The ultraviolet fluorescence time history at the 355°C vapor temperature also showed the initial "spike" followed by a slow decay. A careful arrangement of spatial filtering followed by a holographic grating-monochromator eliminated scattering from the 0.266 μm radiation and the superfluorescent emission at 0.546 and 0.365 μm , but the initial "spike" and the slow decay component remained unchanged. Thus, the fast component "spike" is believed to be associated with the ultraviolet fluorescent emission from the excited molecules. Recent experimental analysis of the fast decay component by Smith *et al.*⁸ concur with our interpretation.

The visible band fluorescence time history showed a gradual fluorescence intensity growth that differed considerably from the time dependence of the ultraviolet band fluorescence. Figure 6(a) shows the growth of the

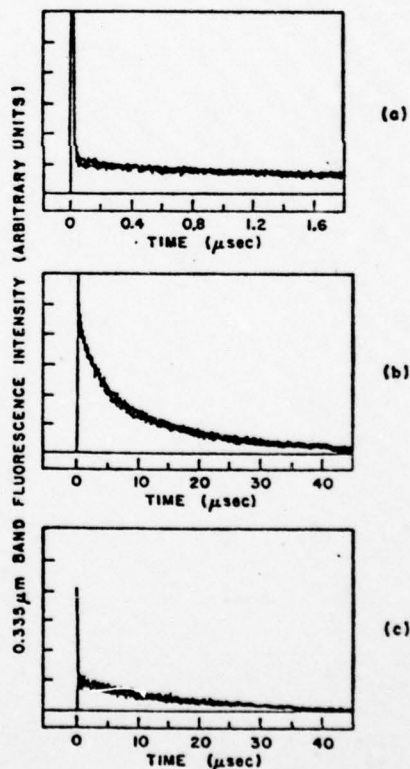


FIG. 5. 0.335 μm band fluorescence time history traces at a Hg density of $3.4 \times 10^{18} \text{ cm}^{-3}$ and 570°C vapor temperature. (a) Initial behavior showing a "spike" and a slow decay. (b) long-time decay with nonexponential character at a pump energy of $\sim 2 \text{ mJ}$; (c) long-time decay with nearly exponential character at a pump energy of $\sim 0.5 \text{ mJ}$.

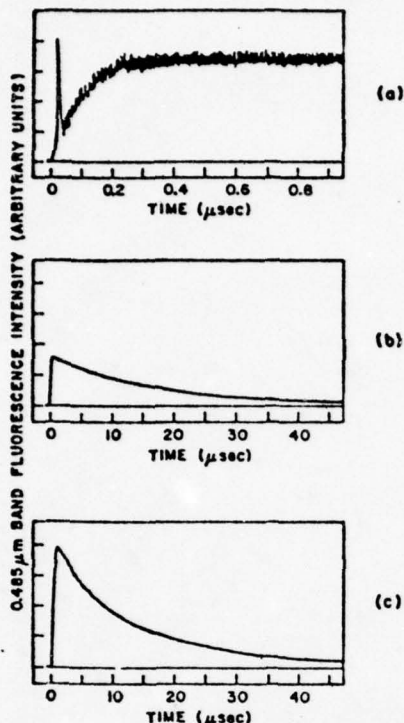


FIG. 6. 0.485 μm band fluorescence time history traces at a Hg density of $3.8 \times 10^{18} \text{ cm}^{-3}$ and 356°C vapor temperature. (a) Initial growth behavior and a small amount of superfluorescent $0.5461 \mu\text{m}$ radiation transmitted through a 488 nm band pass filter; (b) long time decay with nearly exponential character at a pump energy of 0.12 mJ ; (c) long time decay with non-exponential character at a pump energy of 0.37 mJ .

0.485 μm band intensity as a function of time at a Hg density of $3.8 \times 10^{18} \text{ cm}^{-3}$ with 356°C vapor temperature. The fluorescence intensity starts from essentially zero signal at the time of excitation and reaches a peak value in $0.5 \mu\text{sec}$. A 488 nm band pass filter that was used to monitor the visible band also transmitted a small amount of superfluorescent $0.546 \mu\text{m}$ radiation. The transmitted radiation was recorded with the visible band fluorescence signal as a fast pulse marking the time of excitation.

The growth curve of the $0.485 \mu\text{m}$ band fluorescence intensity is well approximated by an exponential return curve of the form $(1 - e^{-bt})$. Figure 7 shows the values of the growth rate, represented by the parameter b , as a function of Hg density, N , at a vapor temperature of 356°C . The growth rate increases from $5.7 \pm 0.8 \times 10^6 \text{ sec}^{-1}$ at $N \approx 1.9 \times 10^{18} \text{ cm}^{-3}$ to $11.0 \pm 0.8 \times 10^6 \text{ sec}^{-1}$ at $N \approx 3.8 \times 10^{18} \text{ cm}^{-3}$, which indicates that b has an approximately linear dependence on the Hg density.

For observation times longer than $0.5 \mu\text{sec}$ the two fluorescence bands decayed with the same time history. The long time decay was approximately exponential at low excitation energies, but became non-exponential at higher pump energies.

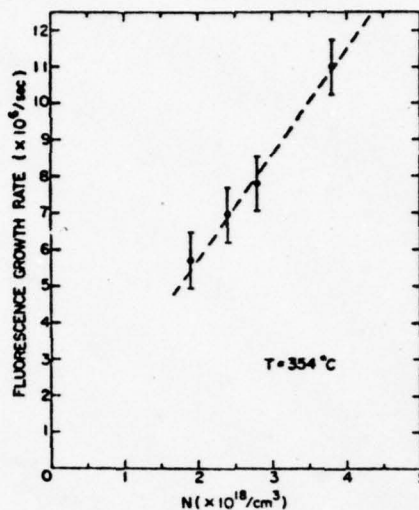


FIG. 7. 0.485 μm band fluorescence growth rate as a function of Hg density, N , at 354°C vapor temperature.

The initial nonexponential decay at higher pump energies gradually became an exponential character when the fluorescence intensity had diminished to a level comparable to the peak of the fluorescence intensity under low energy excitation. Figures 5(b) and 5(c) illustrate this behavior for the ultraviolet band intensity. Figures 6(b) and 6(c) show the same effect for the visible band intensity. Thus, in order to measure the long time exponential decay rate the excitation energy was kept to a minimum. The results of these measurements are plotted in Fig. 8 as a function of Hg density at a vapor temperature of $355^\circ \pm 1^\circ\text{C}$.

The observed exponential decay rate ranges from 3.3

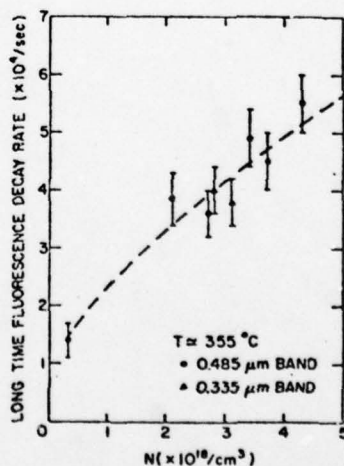


FIG. 8. Long time exponential decay rate as a function of Hg density, N , for both fluorescence bands at 355°C vapor temperature.

$\times 10^3 \text{ sec}^{-1}$ to $5 \times 10^4 \text{ sec}^{-1}$, corresponding to a time constant of 30 to 20 μsec , respectively. These values of decay rate are somewhat larger than those obtained by Drullinger *et al.*⁷ The slight discrepancy on the order of 20% is possibly due to quenching by a small amount of impurities in the cell. However, a cleanliness test⁴ using a HeCd laser at 0.325 and 0.4416 μm to probe the vapor showed no noticeable fluorescence after several months of operation.

The results of the fluorescence time history measurements may be represented by empirical formulas for the population of each molecular species that are responsible for the respective fluorescence. For low excitation energies, the population of the 0.485 μm band radiators is described by the difference of two exponential decay terms:

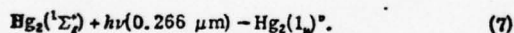
$$n(0.485 \mu\text{m band radiator}) \propto [e^{-at} - e^{-bt}]. \quad (5)$$

The parameters a and b are the long time decay rate and the fluorescence growth rate, respectively. The population of the 0.335 μm band radiators for time $t \geq 40 \text{ nsec}$ is approximated by a simple exponential decay involving the same long time decay rate for the visible band:

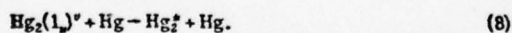
$$n(0.335 \mu\text{m band radiator}) \propto [e^{-at}]. \quad (6)$$

For time $t \leq 0.5 \mu\text{sec}$, the 0.335 μm band fluorescence intensity shows a slight upward departure from the above equation. However, signal-to-noise limitations prevented detailed analysis of the decay behavior in the time interval from 40 to 500 nsec.

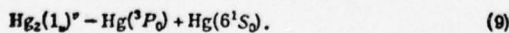
Our experimental analysis may be summarized as a qualitative description of the dynamics of the molecular mercury system excited by a short pulse of 0.266 μm radiation. The molecular absorption of the pump photons, each having an energy of 37590 cm^{-1} , directly creates vibrationally excited 1_u dimers near the dissociation energy limit of the 0_u^- state. This limit lies at 38125 cm^{-1} above the ground state of Hg₂ if the ground state dissociation energy is assumed to be 480 cm^{-1} .¹⁶



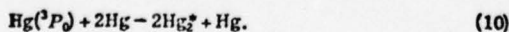
Some of the vibrationally excited 1_u dimers may undergo rapid vibrational relaxation and mixing of excited electronic states, resulting in a thermal equilibrium distribution of population among the Hg₂⁺(1_u , 0_u^- , 1_g , 0_g , 0_u^+) states in less than 40 nsec.



Alternatively, kinetic energy might be assumed to be sufficient to dissociate the excited molecules into the 6^3P_0 and 6^1S_0 atoms prior to vibrational relaxation



Then, the excited dimers must be formed by three body collisions involving the metastable 6^3P_0 atoms



Recent investigation by Stock *et al.*¹⁷ indicates that the above processes, Eq. (9) and Eq. (10), account for more than 90% of the molecular fluorescence when the mercury vapor is optically pumped with 265 nm radiation. Using

their experimentally determined molecular formation rate of $1.55 \times 10^{-21} \text{ cm}^6 \text{ sec}^{-1}$ the 0.335 μm band fluorescence rise time is 560 nsec at $N = 3.4 \times 10^{18} \text{ cm}^{-3}$. Our time history data do not show such growth behavior. However, the explanation may be attributed to signal detection limitations. Fluorescence from excited dimers governed by Eq. (8) may also contribute partially to the early fluorescence time history.

Since 266 and 265 nm photon energy difference is less than kT , the reaction paths of the vibrationally excited dimers are expected to be similar at the two optical pumping wavelengths. Therefore, the dominant processes governing the 0.335 μm radiators are the dissociation of vibrationally excited dimers to yield metastable atoms followed by the formation of Hg₂⁺ molecules via three body collisions.

Drullinger *et al.*⁷ have suggested that the 0.485 μm band fluorescence at Hg densities greater than $5 \times 10^{17} \text{ cm}^{-3}$ and temperatures greater than 575 °K may be explained in terms of a bound excited trimer complex, Hg₃⁺. The trimer state is estimated to lie about 6500 cm^{-1} below the 1_u state of Hg₂⁺ in thermal equilibrium. Since the Hg density and temperature in our experiments satisfy the above conditions, we assume that the Hg₂⁺ and Hg₃⁺ molecules are populated in thermal equilibrium according to the reaction given by Eq. (3).

If the Hg₃⁺ molecules are created according to Eq. (3), the trimer formation rate is a function of the forward and reverse reaction rates as well as the decay rates of each species. Because of a lack of complete kinetic data, we have not yet analyzed the 0.485 μm band fluorescence growth rate in terms of the analytical expression for the trimer formation rate. However, the empirical description of the fluorescence time history suggests that a molecular formation process, described by Eq. (3), rather than a collision-induced radiation effect, described by Eq. (2), is the primary mechanism for the production of the 0.485 μm band radiation under our experimental conditions. This description is helpful in the interpretation of the excimer absorption measurements.

C. Biexcimer quenching

During the fluorescence time history measurements we encountered nonexponential decay behavior on both the ultraviolet and the visible bands at high pump energies. After plotting several decay curves obtained at various pump energies while keeping the Hg density and temperature constant, we realized that all decay curves could be matched identically by shifting the origin of time. This property suggested a quenching process that depends on the density of the excited states. An evidence for such a quenching process in molecular mercury was first observed by Eckstrom *et al.*¹⁸ in an e beam pumped high pressure mercury vapor experiment. The process was interpreted as biexcimer collisional deactivation of the excited metastable molecules, Hg₂⁺, involving the following reaction:



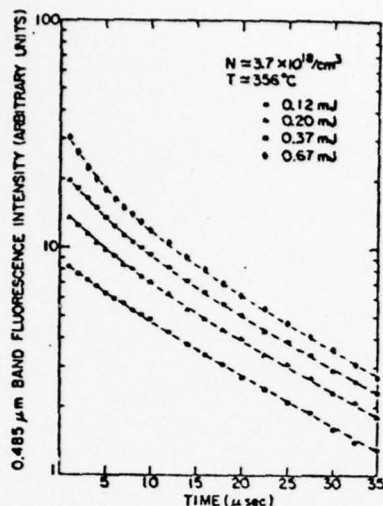


FIG. 9. 0.485 μm band nonexponential long time decay time history at various excitation energies.

where Hg_2^{**} is assumed to be an unspecified highly excited molecule.

If the effect of quenching is included in an empirical rate equation for the population density of the Hg_2^{**} molecules, n , one obtains the following equation:

$$(d/dt)[n(t)] = -a[n(t)] - k[n(t)]^2 \quad (12)$$

The exact solution of the above equation for $t \geq t_0$ is given by

$$n(t) = n_0 \left[\left(1 + \frac{kn_0}{a} \right) e^{a(t-t_0)} - \left(\frac{kn_0}{a} \right) \right]^{-1} \quad (13)$$

The biexcimer quenching rate constant is given by the parameter k . $n_0 = n(t_0)$ is the population density at time $t = t_0$, and a is the long time exponential decay rate. The solution indicates a nonexponential time dependence of $n(t)$ for a time interval short compared to the reciprocal of the long time decay rate. For $a(t - t_0) \gg 1$ the solution becomes approximately exponential with the long time decay rate. These properties of the solution agree well with the experimentally observed decay properties.

In order to determine the biexcimer quenching rate constant, a set of 0.485 μm band fluorescence decay data was analyzed using the method of least squares curve fit of the data with the exact formula given by Eq. (13). Figure 9 shows the 0.485 μm band fluorescence decay data and the curve fit indicated by the dashed curves. The analysis yielded the value of the long time decay rate and the values of kn_0 at various pump energies. The value of n_0 for the lowest pump energy could be independently calculated from the pump beam energy density and the absorption coefficient, since the total excimer fluorescence yield was near unity. At higher pump energies n_0 at 1 μsec was calculated from the relative fluorescence signal normalized to the lowest pump energy data. Figure 10 shows the plot of kn_0 as a function of n_0 . The data points indicate a linear dependence on

n_0 , as expected, and the slope of the plot represents the biexcimer quenching rate constant, k . A linear least squares curve fit of the data points yielded the rate constant of $k = 2 \pm 1 \times 10^{-10} \text{ cm}^3 \text{ sec}^{-1} \text{ molecule}^{-1}$ with most of the uncertainty due to our estimate of the beam area. Our value of k is somewhat larger than the order of magnitude estimate of $10^{-11} \text{ cm}^3 \text{ sec}^{-1} \text{ molecule}^{-1}$ obtained by Eckstrom *et al.*¹⁸ However, the disagreement might be due to differences in the experimental conditions.

The fluorescence time history of the 0.335 μm band and the 0.485 μm band showed a common long time decay due to a thermal equilibrium distribution of the radiators. As long as the biexcimer quenching rate is slow compared to processes that equilibrate the 0.335 μm band and the 0.485 μm band radiators, the common fluorescence decay is expected regardless of which molecular state is responsible for the quenching. A comparison of the fluorescence decay data of the two bands at 356 $^\circ\text{C}$ vapor temperature confirmed this point, even though the relative intensity of the 0.335 μm band was an order of magnitude smaller than the 0.485 μm band intensity.

Since the quenching rate is not required to remain the same when the relative population distribution of the radiators is altered, we analyzed the 0.335 μm band fluorescence decay data at 570 $^\circ\text{C}$ vapor temperature. The analysis showed that, to within experimental error the biexcimer quenching rate constant was the same as the value obtained at the 356 $^\circ\text{C}$ vapor temperature. Thus, the quenching behavior is not appreciably affected by the relative population distribution of the 0.335 μm band and the 0.485 μm band radiators.

The relative populations of the 0.335 μm band radiators, the 0.485 μm band radiators, and the metastable excited dimers in the O_2^+ and O_2^- states may be obtained from the results of the theoretical analyses of Smith *et al.*⁸ For the 0.335 μm band radiators, $[1_u]/[0_u^+]$ $\approx \exp(-2500/kT)$ yields a ratio of 1.4×10^{-2} at 843 $^\circ\text{K}$ and 3.3×10^{-3} at 629 $^\circ\text{K}$. The relative population of the 0.485

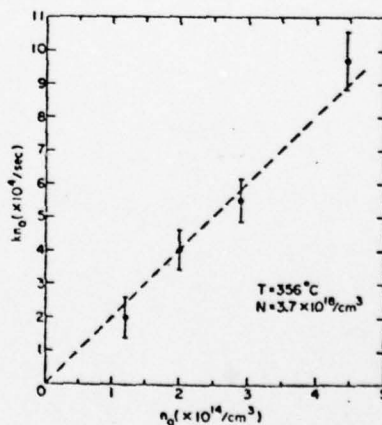


FIG. 10. Biexcimer quenching rate, kn_0 , as a function of the initial excimer density n_0 .

μm band radiators is given by $[\text{Hg}_2^*]/[0_2^*] \approx 20 \times n \times 2.2 \times 10^{-24} \exp(4000/kT)$, which yields a ratio of 4×10^{-5} at 843 K and 4×10^{-4} at 629 K for the total excimer density of $n = 10^{15} \text{ cm}^{-3}$. The calculations show that while the $[\text{Hg}_2^*]/[1_n]$ ratio varies rapidly with T by a factor of 43, nearly 99% of the excimers resides in the 0_2^* states.

In light of the relative population distribution in the excimer system the temperature insensitive biexcimer quenching rate may be interpreted as being due to collisional deactivation of excited dimers involving the metastable 0_2^* states. Therefore, the biexcimer loss mechanisms appear to be directly associated with the 0_2^* states which act as the energy reservoir for the entire excimer system.

The observed properties of the biexcimer quenching suggest that the quenching process could significantly affect the decay of the excited mercury molecules at densities greater than 10^{15} cm^{-3} . At 10^{17} cm^{-3} excited state density the quenching rate becomes $\sim 10^7 \text{ sec}^{-1}$ which reduces the effective lifetime of the molecules to about 100 nsec. Since one of the desirable characteristics of a high power laser medium with high output energy is a storage time ≥ 100 nsec, a practical limit of the excited state density may be estimated to be on the order of 10^{17} cm^{-3} . For the ultraviolet band this limit is equivalent to about 50 J/l of optical stored energy. Bimolecular collisional deactivation can also be expected to be present in molecules similar to the Hg₂ system, such as Cd₂, Zn₂, HgCd, and HgTl and a similar excited state density limitation may apply to most of these potential laser media.

D. Fluorescence power and gain

One of the essential requirements for a laser medium is to have a sufficient net gain within its spontaneous emission bandwidth to achieve threshold for oscillation. Metal vapor excimer systems have been considered as potential candidates having high power output and wide tunability in the visible and ultraviolet wavelengths with small stimulated emission cross sections for high saturation intensities.¹⁹ One difficulty, however, is the small stimulated emission cross section, on the order of 10^{-18} cm^2 to 10^{-20} cm^2 , which must be larger than the absorption cross section as well as large enough to yield a net gain at a reasonable population inversion density for oscillation. Thus, the existence of a net gain becomes the crucial factor in an excimer system such as Hg₂.

Direct gain measurements may be obtained by a number of methods, but are difficult at low net gains. We chose to measure the gain coefficient, γ , by measuring the absolute spontaneous fluorescence power per frequency interval per unit volume, $dP/d\nu$, emitted from the excited region.

For a transition with a normalized homogeneous frequency distribution, $g(\nu)$, and a frequency insensitive spontaneous emission rate, A , we have

$$dP/d\nu = nAh\nu g(\nu) \quad (14)$$

and

$$\gamma(\nu) = \frac{\Delta n A c^2}{8\pi\nu^2} g(\nu) \quad (15)$$

Combining Eqs. (14) and (15) yields

$$\gamma(\nu) = \left(\frac{\Delta n}{n}\right) \left(\frac{c^2}{8\pi h\nu^2}\right) \left(\frac{dP}{d\nu}\right) \quad (16)$$

where Δn and n are the inversion density and the excimer population density. Theoretical analysis²⁰ of bound-continuum transitions in diatomic molecules showed that spontaneous emission power spectrum from excimer states in vibrational thermal equilibrium may be well approximated by the above expression for $dP/d\nu$. The frequency distribution, $g(\nu)$, consists of a sum over contributions from all vibrational states in thermal equilibrium. $g(\nu)$ can be calculated in principle if the parameters of the upper and lower state potentials are known. Such calculation is not necessary for obtaining γ from the experimentally measured $dP/d\nu$. Furthermore, the population inversion density, Δn , can be assumed to be equal to the upper state density, n , for a bound continuum transition to a repulsive lower state that is well above the kinetic energy of the ground state atoms.

Experimentally, we measured an approximate value for $dP/d\nu$ near the peak of the 0.485 μm band at $\nu = \nu_0$ using a 488 nm spike filter with a 10 nm bandwidth and a photomultiplier. The photomultiplier power response was calibrated using an argon ion laser at 488 nm. Thus, the peak gain coefficient, γ_0 , was calculated at $\lambda = 0.488 \mu\text{m}$ using

$$\gamma_0 = \gamma(\nu_0) \approx \left(\frac{c^2}{8\pi\nu_0^2}\right) \left(\frac{1}{h\nu_0}\right) \left(\frac{dP}{d\nu}\right)_{\nu=\nu_0} \quad (17)$$

At a Hg density of $4.3 \times 10^{18} \text{ cm}^{-3}$ and 355 °C vapor temperature, we obtained $\gamma_0 \approx 2.5 \pm 1.3 \times 10^{-5} \text{ cm}^{-1}$ using a relatively low pumping level of $\sim 30 \text{ mJ/cm}^2$ with the corresponding total excited state density of $6 \pm 3 \times 10^{14} \text{ cm}^{-3}$. Under the same pumping conditions a similar measurement of the gain coefficient for the 0.335 μm band gave an order of magnitude smaller value than the value at 0.488 μm in good agreement with the theoretical gain estimates obtained by Smith *et al.*⁸ At greater pumping energy densities γ_0 increases to a value on the order of 10^{-4} cm^{-1} , but since the pump energy was limited to 5 mJ larger values of γ_0 were not observed.

We also attempted to measure $dP/d\nu$ from the high temperature region of the cell where the ultraviolet band fluorescence is dominant. Because of a complex fluorescence collection geometry, reliable data could not be obtained. However, we estimate a maximum gain coefficient on the order of 10^{-4} cm^{-1} at 0.335 μm in our experiment by considering the fluorescence yield and the available pump energy.

These gain coefficient measurements imply a single pass gain of about 1% in our cell which is detectable with appropriate electronics if there are no appreciable loss mechanisms. Therefore, in order to measure a net single pass gain or loss for the mercury excimer system, we probed the excited medium with a cw HeCd laser op-

erating at 0.325 and 0.4416 μm . The measurements are discussed in the next section.

E. Excimer optical transmission at 0.325 and 0.4416 μm

Previous measurements of the mercury excimer optical transmission have been made with e beam pumped high pressure mercury vapor. Hill *et al.*² observed net loss of transmission for visible wavelengths on the short wavelength side of the 0.485 μm band. More recently, Schlie *et al.*³ reported net gain measurements at several wavelengths within the 0.335 μm band. One of our principal objectives was to study the optical transmission of the excited medium under a more selective production of excimer states obtainable with optical pumping. Using cw HeCd laser outputs at 0.4416 and 0.325 μm , we probed the excited mercury vapor to measure the optical transmission as a function of time.

The representative 0.325 μm probe transmission is characterized by a rapid decrease of signal in less than 50 nsec followed by a gradual recovery lasting about 20 μsec . Figures 11(a) and 11(b) show the transmission time history from the time of the pump excitation to 40 μsec . The HeCd laser output fluctuation caused the jitter in Fig. 11(b), but the probe signal was relatively smooth on a fast time scale.

The depth or amplitude of signal loss varied proportionally with the pump energy at a constant Hg density. At a fixed pump energy a decrease in the Hg density led to a smaller signal loss as indicated by Figs. 11(a) and 11(c). This was expected since less pump energy is absorbed at a reduced Hg density. The 0.4416 μm probe transmission demonstrated the same time history shown in Fig. 11(d), but the depth of signal loss was only 20% to 25% of the loss at the 0.325 μm probe wavelength under the same conditions.

The signal loss amplitude time dependence is quite similar to the 0.325 μm band fluorescence time history

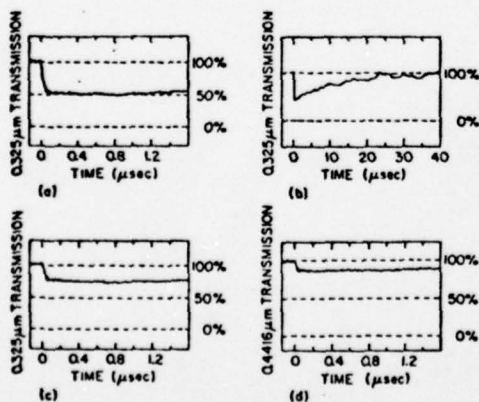


FIG. 11. Probe transmission of the excited mercury vapor at 570°C. (a) and (b) 0.325 μm probe transmission at a Hg density of $4.1 \times 10^{18} \text{ cm}^{-3}$ and a pump energy of 1.2 mJ; (c) 0.325 μm probe transmission at a Hg density of $3.1 \times 10^{18} \text{ cm}^{-3}$ and a pump energy of 1.2 mJ; (d) 0.4416 μm probe transmission at a Hg density of $3.4 \times 10^{18} \text{ cm}^{-3}$ and a pump energy of 2 mJ.

except for the initial "spike." This correlation suggests that the probe signal loss is caused by the same excimer states that are responsible for the 0.335 μm band. The optical transmission loss is interpreted as absorption due to certain Hg₂^{*} excimer states. Since several electronic states of Hg₂^{*} near 30 000 cm^{-1} above the ground state are believed to be in thermal equilibrium, the lowest excited dimer states are likely to be primarily responsible for absorption. An examination of the Hg₂ potential curves^{5,9,21} suggests that absorption from the lowest Hg₂^{*} states to several higher molecular states is energetically possible with the probe wavelengths.

It is not known whether the excited state absorption is caused by bound-bound or bound-continuum transitions, but the absorption cross-section at the probe wavelengths can be obtained experimentally. Based on estimates of the excimer density, the absorption cross section for the 0.325 μm wavelength is estimated to be greater than 10^{-17} cm^2 . A somewhat smaller absorption is obtained for the 0.4416 μm wavelength.

Our observation of net loss at 0.4416 μm is consistent with the results obtained by Hill *et al.*,² but the measured net loss at 0.325 μm in our experiment is in disagreement with Schlie's measurements.³ Recent experiments by Drullinger²² and York and Judd²³ also showed evidence of net loss at 0.325 μm . The reasons for the disagreement are not well understood, but it has been suggested²⁴ that the difference may arise from the pumping methods. The optical pumping scheme generally provides a more selective means of populating excimers without the presence of free electrons and other excited species generated by e beam pumping. Thus, we believe that our data indicate a net absorption at 0.325 μm due to Hg₂^{*} states.

Our measurements also indicate that the loss per unit length of 10^{-3} to 10^{-2} cm^{-1} exceeds our estimates of gain coefficient by more than an order of magnitude. Therefore, stimulated emission in the mercury excimer system appears to be prevented by excited state absorption. However, without a further understanding of the absorption process and a detailed spectroscopic analysis we cannot state for certain that mercury dimer will not achieve net gain under selected conditions.

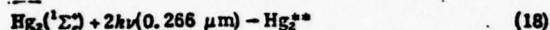
F. Superfluorescent atomic Hg transitions

Laser action has been observed earlier in neutral atomic mercury by direct two photon pumping.²⁵ We achieved atomic laser action in our experiment by optical pumping of the molecular states and not by atomic two photon absorption resonances. The fluorescence emission lines have been identified to originate from the 8^3S_1 , 7^3P_2 , 7^1P_1 , 6^3D_2 , and 6^1D_2 atomic states. The observed emission lines are listed in Table I.

One of the strongest superfluorescent emission from these levels is the $6^3D_2 - 6^3P_2$ transition at 0.365 μm . Detailed measurements of the 0.365 μm output energy showed a quadratic dependence on the pump energy which suggested absorption of two pump photons. The 0.365 μm output was proportional to the square of the atomic mercury density, N , indicating that the absorption was

due to the ground state Hg₂ molecules whose equilibrium population is proportional to N^2 .²⁰ The superfluorescent pulse lasted less than 2 nsec and was coincident with the peak of the pump pulse at all pump energies above threshold. These results suggested that the 6³D₂ atoms are produced by photodissociation of excited molecules caused by either direct or sequential absorption of two pump photons.

Since two pump photons have enough energy to create atomic states below 75 000 cm⁻¹, molecular two photon absorption followed by dissociation can explain the observed fluorescence emission lines.

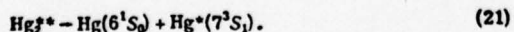


Thus, another strong superfluorescent emission at 1.395 μm corresponding to the 7³P₀ - 7³S₁ transition can be explained by the above pumping mechanism.

At Hg densities $N \geq 3 \times 10^{18}$ cm⁻³, the 7³S₁ - 6³P₂ transition at 0.546 μm becomes the dominant laser output having the lowest pumping threshold. A typical energy conversion from the pump to the green output was less than 0.17% with unfocused beam, but up to 1% conversion could be achieved with a focused beam. The output energy measurements showed a quadratic dependence on the pump energy as in the 0.365 μm case, but the output varied approximately as N^4 instead of N^2 . The output pulse also showed a 2 to 5 nsec delay relative to the pump pulse peak.

The 0.546 μm output properties could not be explained by the same pumping mechanisms governing the other emission lines. The output energy and threshold measurements also ruled out the possibility of 0.546 μm laser action due to cascading transitions originating from the 7³P₁ state. This implied that the primary mechanism of creating the 7³S₁ atoms must be due to collisional processes involving the excimers. The pulse delay and the output energy dependence varying as high powers of N supported this hypothesis and led to two models of pumping mechanisms.

The first model is based on bimolecular excited dimer collisions followed by decomposition to yield an excited atom in the 7³S₁ state according to the following reaction



Since the optically pumped Hg₂^{*} population varies as N^2 , the above reactions immediately explained the N^4 dependence of the output and the pulse delay. However, in order for this process to be the primary pumping mechanism, a bimolecular rate constant of 10⁻⁹ cm³ sec⁻¹ molecule⁻¹ is necessary. The corresponding collisional cross section is $\sigma_c \approx 3 \times 10^{-14}$ cm². Collisional deactivation involving the Hg(6³P₀) and Hg(6³P₁) atoms is known to have comparable cross section values.²⁸ Since optical pumping creates 1_u states near the dissociation limit of the 0_u state, the required value of σ_c is not unreasonable, even though the bimolecular rate is an order of

magnitude larger than our measured value for the excimers in the lowest excited states.

The second model to explain the delayed 0.546 μm emission is based on the excimer photodissociation by the trailing part of a 5 nsec pump pulse. In this model collisions are assumed to yield Hg₂^{*} and Hg₂^{**} states prior to photodissociation. Based on the experimental fluorescence growth-rate this process is estimated to yield $\geq 10^{12}$ cm⁻³ excimer density during a pump pulse. If these excimers are immediately photodissociated to produce the 7³S₁ atoms, superfluorescence threshold could be reached provided that the photodissociation cross section is greater than 10⁻¹⁷ cm². Since the Hg₂^{*} absorption cross section at 0.325 μm is estimated to be greater than 10⁻¹⁷ cm², the delayed excimer photodissociation model can be considered as an alternative explanation to the bimolecular dimer collisional model.

Experiments designed to distinguish the two models have not yet been conducted. However, once the pumping mechanism is understood, the superfluorescent 0.546 μm transition may be useful as a diagnostic tool for monitoring the excimer population.

IV. CONCLUSION

We have investigated by optical pumping the properties of the mercury excimer system which may be relevant to the understanding of Hg₂ as a potential laser medium. Optical pumping with 0.266 μm radiation excited 0.335 and 0.485 μm band fluorescence which showed different initial time history and a common long time decay behavior.

The difference in the initial time history arises from the different formation mechanisms governing the fluorescence radiators. The optically pumped vibrationally excited 1_u dimers are partially relaxed, but the dominant reactions leading to 1_u population are the creation of ³P₀ metastable atoms by dissociation and the subsequent Hg₂^{*} formation via three body collisions. The 0.485 μm band radiators are thought to be Hg₂^{*} which are formed from Hg₂^{*}. The formation rate is found to be nearly proportional to the Hg density from 1.9 to 3.8 × 10¹⁸ cm⁻³ with the corresponding rates of 5.7 × 10⁶ sec⁻¹ and 1.1 × 10⁷ sec⁻¹. The initial time history lasting 0.5 μsec is followed by a common decay behavior for the both bands with a typical exponential decay time constant of 20 to 30 μsec.

As one of the main objectives of our study, we have determined gain coefficients for the continuous emission bands by measuring the absolute spontaneous fluorescence power per frequency interval per volume of excited mercury vapor. The results for the 0.485 μm band showed a peak gain coefficient of 2.5 ± 1.3 × 10⁻³ cm⁻¹ with an excited state density of 6 ± 3 × 10¹⁴ cm⁻³. The same conditions gave an order of magnitude smaller gain coefficient for the 0.335 μm band, but the higher vapor temperature enhanced the gain.

Based on our available pump energy and experimental conditions we estimated a maximum gain coefficient on the order of 10⁻⁴ cm⁻¹ for the 0.335 μm band. However,

when the excited medium transmission was probed at 0.325 μm a significant net loss rather than gain was observed. The time history of net loss is interpreted as net absorption due to the Hg₂^{*} states with an estimated absorption cross section of greater than 10⁻¹⁷ cm². Probe transmission at 0.4416 μm also showed net absorption cross section. These measurements signified that excimer absorption may be more than an order of magnitude greater than the stimulated emission gain. Further analysis of the absorption process and excited state spectroscopy are needed to fully evaluate the Hg₂ excimer system as a potential laser medium. However, our results indicate that a demonstration of stimulated emission in Hg₂ is likely to remain a difficult problem.

Another important property of excimers analyzed in our study is the excited state deactivation by bimolecular excimer collisions. The quenching rate constant was measured to be $2 \pm 1 \times 10^{-10}$ cm³ sec⁻¹ molecule⁻¹. The process is believed to be an inherent decay property directly associated with the low-lying Q₂^{*} dimer states which serve as the energy reservoir of the excimer system. For a potential laser medium with a 100 nsec energy storage time, the biexcimer quenching process implies an inherently limiting excimer density on the order of 10¹⁷ cm⁻³, which is equivalent to about 50 J/l of optical stored energy.

The mercury excimer system has yet to be demonstrated as a laser medium, but our optical pumping studies of the excited states show some of the radiative and collisional properties at excimer densities approaching the required inversion densities for laser oscillation. These properties are likely to be present in other similar molecular systems such as HgCd, Cd₂, and HgTl and it is hoped that the results of Hg₂ experiments will be useful in understanding the dynamics of these molecules.

ACKNOWLEDGMENTS

We wish to acknowledge the support provided by AFOSR and ERDA and helpful discussions with M. Hessel, R. Drullinger, L. Schlie, G. York, and D. Judd. We appreciate many helpful comments by E. Smith. We also thank Professor B. Hudson of Chemistry Department for the use of the HeCd laser and N. Holmes and

M. Artusy for their assistance in processing the mercury cell.

- ¹R. J. Carbone and M. M. Litvak, *J. Appl. Phys.* **39**, 5, 2413 (1968).
- ²R. M. Hill, D. J. Eckstrom, D. C. Lorents, and H. H. Nakano, *Appl. Phys. Lett.* **23**, 373 (1973).
- ³L. A. Schlie, B. D. Guenther, and R. D. Rathge, *Appl. Phys. Lett.* **28**, 393 (1976).
- ⁴G. W. York and R. J. Carbone (a paper presented at the 3rd Summer Colloquium on Electronic Transition Lasers, Aspen, Colorado, September 7-10, 1976).
- ⁵F. G. Houtermans, *Helv. Phys. Acta.* **33**, 933 (1960).
- ⁶R. E. Drullinger, M. M. Hessel, and E. W. Smith, *Natl. Bur. Stand. (U.S.) Monogr.* **143** (1975).
- ⁷R. E. Drullinger, M. M. Hessel, and E. W. Smith, *J. Chem. Phys.* (to be published).
- ⁸E. W. Smith, R. E. Drullinger, M. M. Hessel, and J. Cooper (to be published in *J. Chem. Phys.*).
- ⁹S. Mrozowski, *Z. Phys.* **104**, 228 (1937).
- ¹⁰H. Kuhn and K. Freudenberg, *Z. Phys.* **76**, 38 (1932).
- ¹¹R. Lennuter, *Comput. Rend. Acad. Sci.* **213**, 169 (1941); R. Lennuter and Y. Crenn, *ibid.* **216**, 486, 533 (1943).
- ¹²R. L. Herbst, H. Komine, and R. L. Byer, *Opt. Commun.* **21**, 5 (1977).
- ¹³*Handbook of Chemistry and Physics*, edited by R. C. Weast (Chemical Rubber, Cleveland, 1966-67), 47th ed. p. D-108.
- ¹⁴Lord Rayleigh, *Proc. R. Soc. Ser. A* **125**, 1 (1929); A. O. McCoubrey, *Phys. Rev.* **92**, 1249 (1954); P. Pringsheim, *Fluorescence and Phosphorescence* (Interscience, New York, 1964), p. 218-235.
- ¹⁵H. Komine and R. L. Byer, *J. Appl. Phys.* (to be published).
- ¹⁶J. Frank and N. Grotrian, *Z. Tech. Phys.* **3**, 194 (1922).
- ¹⁷M. Stock, E. W. Smith, R. E. Drullinger, and M. M. Hessel (*J. Chem. Phys.* to be published).
- ¹⁸D. J. Eckstrom, R. W. Hill, D. C. Lorents, and H. H. Nakano, *Chem. Phys. Lett.* **23**, 112 (1973).
- ¹⁹D. C. Lorents, R. M. Hill, and D. J. Eckstrom, *Molecular Metal Lasers*, Semi-annual Technical Report No. 1, Stanford Research Institute, Menlo Park, CA, 1972.
- ²⁰F. H. Mies, *Mol. Phys.* **26**, 5, 1233 (1973).
- ²¹P. J. Hay, T. H. Dunning, Jr., and R. C. Raffanetti, *J. Chem. Phys.* **65**, 2679 (1976).
- ²²R. E. Drullinger (private communication).
- ²³G. W. York and D. Judd (private communication).
- ²⁴M. Stock, R. E. Drullinger, and M. M. Hessel (in a paper given at the Third Summer Colloquium on Electronic Transition Lasers, September 7-10, Snowmass, Colorado, 1976).
- ²⁵R. Wallenstein, *Opt. Commun.* **18**, 2 (1976); IXth International Quantum Electronics Conference, (Abstract).
- ²⁶O. Bochkova, S. Frish, and Yu. Tolmachev, *Opt. Comm.* **7**, 423 (1973).

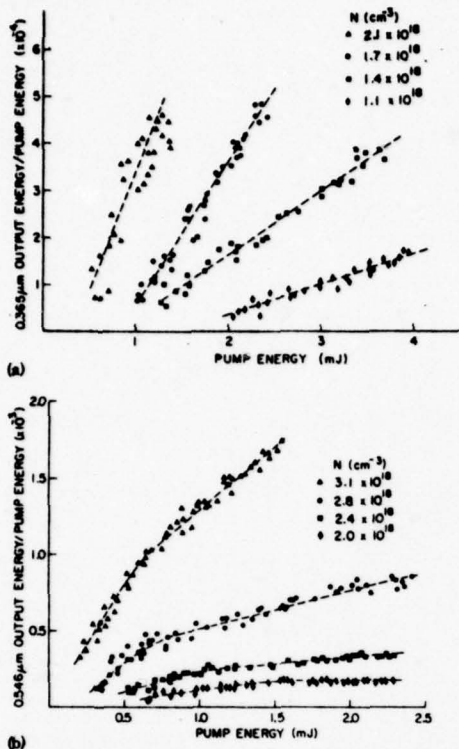


FIG. 2. (a) Output energy/0.266- μm pump energy ratio versus pump energy at various atomic Hg densities, 0.365- μm data (ratio in units of 10^{-4}). (b) Output energy/0.266 μm pump energy ratio versus pump energy at various atomic Hg densities, 0.546- μm data (ratio in units of 10^{-3}).

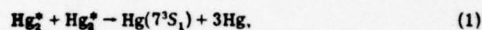
by probing with a 0.325- μm HeCd laser. Details of the Hg_2 measurements will be published elsewhere.

Table I shows the atomic Hg transitions that were observed to superfluoresce. Of these, the 0.365-, 0.546-, and 1.395- μm transitions were strong. The green 0.546- μm ($7^3S_1 - 6^3P_2$) and ultraviolet 0.365- μm ($6^3D_3 - 6^3P_2$) transitions were studied in detail to help determine the pumping mechanisms involved in creating the atomic population inversions.

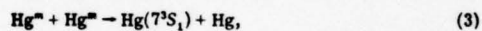
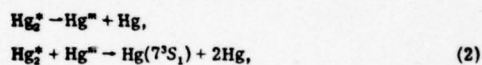
Figures 2(a) and 2(b) show the output energy ratios versus the input pump energy for the 0.365- and 0.546- μm transitions at various atomic mercury number densities. The ultraviolet output energy ratio varies linearly with the input pump energy showing that the 0.365- μm emission is proportional to the incident pump energy squared. The green output energy ratio shows the same power-law scaling initially, but decreases when the 0.365- μm transition reaches threshold and begins to oscillate. From Fig. 2(b) the observed conversion efficiency is 0.17% at the highest Hg density. However, conversion efficiencies up to 1% have been observed when the incident 0.266- μm pump radiation was focused into a 30-cm-long mercury cell.

If we plot the slopes shown in Figs. 2(a) and 2(b) versus the second power of the atomic number density, N^2 , we obtain the results shown in Fig. 3. From Fig. 3 it is evident that the ultraviolet emission varies as the atomic density squared, which is the same dependence the Hg_2 density has relative to atomic mercury density. Inspection of the atomic levels shows that there is not a two-photon resonance within the atomic system so that the N^2 dependence and pump energy squared dependence suggest that the pumping is within the molecular system and that it occurs by the absorption of two pump photons followed by direct photodissociation of Hg_2 into the 6^3D_3 , 7^3P_1 , 8^3S_1 , 6^1D_2 , and 7^1P_1 atomic levels. The pumping mechanism may be by either sequential absorption of two photons or by two-photon absorption within the molecular system.

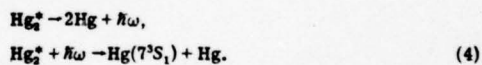
On the other hand the approximate N^4 dependence of the 0.546- μm transition suggests pumping mechanisms involving two excited dimers, Hg_2^* . The formation of 7^3S_1 atoms may occur via direct dimer collisions,



or through intermediate reactions involving collisions with metastable 6^3P_0 atoms, Hg^m ,



or photodissociation by absorption of spontaneous molecular emission,



Another possible mechanism that leads to N^4 dependence is a three-body recombination of a metastable atom to form an excited dimer Hg_2^* followed by photodissociation by the 0.266- μm pump pulse.

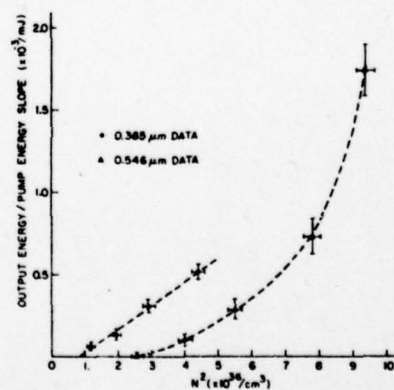
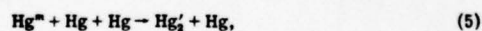
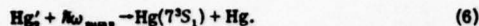


FIG. 3. Output energy/pump energy slope (in units of $10^{-3}/\text{mJ}$) versus N^2 (in units of $10^{16}/\text{cm}^3$).



If the Hg_2^* formation is assumed to be in thermal equilibrium, the lowest excited dimer states near $30\,000\text{ cm}^{-1}$ above the ground state are significantly populated. A simple energy consideration shows that a $0.266\text{-}\mu\text{m}$ pump photon has only enough energy to cause photodissociation of Hg_2^* leading to an excited atom in the 7^3S_1 state. These processes should lead to a time delay of the $0.546\text{-}\mu\text{m}$ emission relative to the $0.266\text{-}\mu\text{m}$ pump pulse.

To test the proposed inversion mechanisms we carefully measured the time history of the 0.365- and $0.546\text{-}\mu\text{m}$ transitions with a time resolution of 2 nsec . The $0.365\text{-}\mu\text{m}$ superfluorescent pulse is 2 nsec wide and occurs at the peak of the 5.0-nsec -wide $0.266\text{-}\mu\text{m}$ pump pulse. This is consistent with pumping via two photons followed by rapid dissociation to the 6^3D_2 level.

The peak of the $0.546\text{-}\mu\text{m}$ pulse is delayed by 2 nsec for a 1.5-mJ pump pulse and by 5 nsec for a 0.6-mJ pump pulse energy. Longer delays are not observed since the $0.546\text{-}\mu\text{m}$ transition is self-terminating. The observed time behavior of the $0.546\text{-}\mu\text{m}$ output is consistent with the 7^3S_1 formation via a collision process followed by rapid dissociation of the highly excited Hg_2 molecules.

Since the $0.546\text{-}\mu\text{m}$ superfluorescent emission self-terminates in 2 nsec we chose to monitor the 7^3S_1 population by observing the time behavior of the non-superfluorescing $0.4358\text{-}\mu\text{m}$ transition. We observed that the $0.4358\text{-}\mu\text{m}$ fluorescence had slightly less than a 20-nsec buildup time followed by an initial exponential decay time of less than 10 nsec and a slower tail with a decay time of about 20 nsec . The peak fluorescence emission occurred 10 nsec after the peak of the $0.266\text{-}\mu\text{m}$ pump pulse.

We have also investigated the infrared transitions and observed the strongest infrared superfluorescence at $1.395\text{ }\mu\text{m}$ corresponding to the $7^3\text{P}_0 - 7^3\text{S}_1$ transition. The superfluorescence threshold pump energy for this transition was observed to be higher than that for the $0.546\text{-}\mu\text{m}$ emission even though the $1.395\text{-}\mu\text{m}$ transition has a larger calculated stimulated emission cross section based on the Einstein A coefficients for these transitions.^{10,11} Furthermore, the threshold pump energy for the $1.395\text{-}\mu\text{m}$ superfluorescence increased from 0.3 to 0.4 mJ at $N=2.3 \times 10^{18}/\text{cm}^3$ to about 1 mJ at $N=3.0 \times 10^{18}/\text{cm}^3$. These observations are contrary to the expected behavior of $7^3\text{P} - 7^3\text{S}_1$ population inversion if the mechanism of 7^3S_1 formation was solely due to radiative decay from the 7^3P_0 state with a lifetime¹¹ of 43 nsec . Also this model does not lead to the N^4 dependence of the $0.546\text{-}\mu\text{m}$ emission. Thus, while the $7^3\text{P}_0 - 7^3\text{S}_1$ radiative decay is observed, experimental evidence suggests that a more dominant mechanism must be responsible for the formation of the 7^3S_1 state at high Hg densities.

The formation of 7^3S_1 states via mechanisms (1)–(4) may be described by a simplified rate equation with respective rate constants:

$$\frac{d}{dt} [7^3\text{S}_1] = (k_1 + k_4)[\text{Hg}_2^*] + k_2[\text{Hg}_2^*][\text{Hg}^m] + k_3[\text{Hg}^m]^2 - \frac{1}{\tau} [7^3\text{S}_1]$$

where τ is the lifetime of the 7^3S_1 state. Since a significant 7^3S_1 population is observed to last for only about 20 nsec after the pump pulse, the primary reactions are assumed to be those involving Hg_2^* species which may be relatively short-lived vibrationally excited dimers. If we assume $[\text{Hg}_2^*] = [\text{Hg}^m]$ during and immediately following the pump pulse, we may obtain an estimate for the combined rate constant $k = k_1 + k_2 + k_4$ from experimental data. At $N = 3.9 \times 10^{18}/\text{cm}^3$ and $T = 570^\circ\text{C}$, a 1-mJ pump pulse creates approximately $10^{14}/\text{cm}^3$ of Hg_2^* and generates a $0.546\text{-}\mu\text{m}$ pulse of about $0.1\text{ }\mu\text{J}$ with a 3-nsec delay with respect to the peak of the pump pulse. This leads to $k \sim 10^9\text{ cm}^3/\text{sec}$ for an estimate of the combined rate constant. Since the mean relative speed is approximately $3 \times 10^4\text{ cm/sec}$, the corresponding collisional cross section is about $3 \times 10^{-14}\text{ cm}^2$. This value of k is approximately two orders of magnitude greater than the value found for dimer collisions involving dimers in the bottom of the potential well as previously reported by workers at Stanford Research Institute¹² and verified by our Hg_2 fluorescence decay measurements. However, our estimate of the collisional cross section is not unreasonable for collisions involving excited dimers near the dissociation limit of the potential well, since collisions involving two excited Hg atoms in 6^3P_0 or 6^3P_1 states have cross sections¹³ on the order of 10^{-14} cm^2 .

The combined rate constant includes a contribution due to photodissociation of dimers by spontaneous molecular emission, k_4 . An estimate of this contribution may be obtained using an approximate expression $k_4 \sim \frac{1}{2}\sigma A d$, where σ is the photodissociation cross section, A is the spontaneous emission rate for Hg_2^* , and d is the diameter of the pump beam. If the atomic spontaneous emission rate of $\sim 8 \times 10^6\text{ sec}^{-1}$ for the $6^3\text{P}_1 - 6^1\text{S}_0$ transition is used for A and $\sigma \geq 3 \times 10^{-17}\text{ cm}^2$ is assumed from our dimer absorption measurement at $0.325\text{ }\mu\text{m}$, then $k_4 \geq 4 \times 10^{-11}\text{ cm}^3/\text{sec}$ is obtained. Our estimate of k_4 suggests that it is not a significant contribution to the combined rate constant; however, we cannot completely rule out the possibility of a larger value of k_4 since accurate values for A and σ are not presently available.

If the direct molecular absorption leads immediately to dissociative formation of metastable atoms, then processes (5) and (6) may become a primary path for the formation of the 7^3S_1 state. A pair of simplified equations governing processes (5) and (6) is given by

$$\frac{d}{dt} [\text{Hg}_2^*] = k_p N^2 [\text{Hg}^m]$$

and

$$\frac{d}{dt} [7^3\text{S}_1] = k_6 [\text{Hg}_2^*] - \frac{1}{\tau} [7^3\text{S}_1]$$

The requisite condition for this process to be important is that Hg_2^* density must attain at least $10^{11}/\text{cm}^3$ during the pulse length, τ_p , of the $0.266\text{-}\mu\text{m}$ radiation. Using an estimated molecular formation rate constant, k_p , of about $(2-3) \times 10^{-31}\text{ cm}^6/\text{sec}$ molecule and assuming $N = 3.9 \times 10^{18}\text{ cm}^3$ and $[\text{Hg}^m] \sim 10^{14}/\text{cm}^3$ during a 1-mJ pulse, we find that Hg_2^* density may reach on the order of $10^{12}/\text{cm}^3$ in 5 nsec . The photodissociation rate, k_6 ,

may be expressed in terms of the pump intensity I_p and the photodissociation cross section σ .

$$k_0 = \sigma I_p / N \omega_{\text{pump}}$$

The 7^2S_1 formation is Hg_2^+ density limited if $k_0 \tau_p \gg 1$, and for a 1-mJ pulse with a $8.4 \times 10^{-2} \text{ cm}^2$ beam area this condition is satisfied if $\sigma \geq 6 \times 10^{-17} \text{ cm}^2$. This value of σ is comparable to the dimer absorption cross section obtained at $0.325 \mu\text{m}$, suggesting that the above model is a possible explanation for the observed properties of the $0.546\text{-}\mu\text{m}$ emission. Evidently a correct model for the formation of the 7^2S_1 state requires a further understanding of the kinetics of the highly excited dimers near the dissociation limit of the 3^1O_2 state.

In conclusion we have observed superfluorescent emission in atomic mercury due to dissociation of Hg_2 pumped by $0.266\text{-}\mu\text{m}$ radiation. The measured intensity and density dependence suggest that two pumping mechanisms are involved: direct absorption of two pump photons by Hg_2 followed by rapid dissociation, and absorption of pump photons followed by dimer-dimer interactions and radiative excitations leading to molecular dissociation and the formation of mercury atoms in the 7^2S_1 level. The observed superfluorescent energy conversion efficiency of 0.17% corresponds to an 7^2S_1 inversion density of approximately 10^{11} cm^{-3} which is formed by collisions of excited dimers at a density near $10^{14}\text{--}10^{15} \text{ cm}^{-3}$. The N^4 scaling suggests that dimer-dimer collisions are an important process in the production of atomic mercury states and may be a

limiting process for the energy storage density in future dimer laser systems.

The authors wish to acknowledge the support provided by LASL and helpful discussions with M. Hessel and D. Judd.

¹R. J. Carbone and M. M. Litvak, *J. Appl. Phys.* **39**, 2413 (1968).

²R. M. Hill, D. J. Eckstrom, D. C. Lorents, and H. H. Nakano, *Appl. Phys. Lett.* **23**, 373 (1973).

³R. E. Drullinger, M. M. Hessel, and E. W. Smith, *Natl. Bur. Stand. (U.S. Monogr. 143)* (1975).

⁴G. W. York and R. J. Carbone, 3rd Summer Colloq. on Electronic Transition Lasers, Aspen, Colo. 1976 (unpublished).

⁵L. A. Schlie, B. D. Guenther, and R. D. Rathge, *Appl. Phys. Lett.* **28**, 393 (1976).

⁶R. Wallenstein, *Opt. Commun.* **18**, 2 (1976); IXth International Quantum Electronics Conference, abstract (unpublished).

⁷R. L. Herbst, H. Komine, and R. L. Byer, *Opt. Commun.* (to be published).

⁸P. J. Hay, T. H. Dunning, Jr., and R. C. Raffanetti, *J. Chem. Phys.* **65**, 2679 (1976).

⁹S. Mrozowski, *Z. Phys.* **104**, 228 (1937).

¹⁰P. Jean, M. Martin, J. P. Barrat, and J. L. Cojan, *C. R. Acad. Sci. (Paris)* **264**, 149 (1967).

¹¹R. J. Anderson, E. T. P. Lee, and C. C. Lin, *Phys. Rev.* **157**, 31 (1967).

¹²D. J. Eckstrom, R. M. Hill, D. C. Lorents, and H. H. Nakano, *Chem. Phys. Lett.* **23**, 112 (1973).

¹³O. Bochkova, S. Frish, and Yu. Tolmachev, *Opt. Commun.* **7**, 423 (1973).

APPENDIX C

POLARIZATION PROPERTIES OF TWO PHOTON TRANSITIONS

1. INTRODUCTION

In two photon processes the transition rate is a function of the intensity and the polarization of the two electromagnetic fields. In calculating the gain for stimulated two-photon emission and anti-Stokes Raman scattering, detailed information on the polarization dependence is necessary to analyze the effect of more than one intermediate state. A general treatment of nonlinear atomic susceptibilities using irreducible spherical tensor techniques by Yuratich and Hanna⁵⁶ provides means of studying the polarization properties. In this appendix the polarization properties of two photon transitions are derived using a similar approach.

The nonlinear susceptibility $\chi^{(3)}$ and the transition rate $W^{(2)}$ for two photon processes are obtained from perturbation calculations. In the electric dipole approximation the interaction hamiltonian is given by³⁶

$$\mathcal{H}_{int} = - \vec{\mu} \cdot (\vec{E}_1 + \vec{E}_2 + \vec{E}_3) \quad (C.1)$$

where the electric fields are given by

$$\vec{E}_\ell(\vec{r}, t) = \frac{1}{2} \hat{\epsilon}_\ell E_\ell e^{i(\vec{k} \cdot \vec{r} - \omega_\ell t)} + \text{c.c.} \quad (\text{C.2})$$

For two photon transitions between states $|a\rangle \equiv |\gamma_a J_a M_a\rangle$ and $|b\rangle \equiv |\gamma_b J_b M_b\rangle$ with an energy difference $\hbar\omega_{ba}$ the resonance conditions are $\omega_1 + \omega_2 = \omega_{ba}$ for two-photon emission (TPE) and $\omega_3 - \omega_1 = \omega_{ba}$ for anti-Stokes Raman scattering (ASRS). The perturbation calculations³⁶ yield the following formulas for $\chi_\ell^{(3)}$ and $w_{ba}^{(2)}$ for the $|b\rangle \Rightarrow |a\rangle$ transition.

$$\begin{aligned} \chi_1^{\text{TPE}} &= \chi_2^{\text{TPE}} \\ &= \left[\frac{N_b - N_a}{4\hbar\epsilon_0} \right] \left[\frac{1}{g_b} \right] \frac{\left[\sum_{M_b} \sum_{M_a} |\alpha_{1,2}|^2 \right]}{[(\omega_1 + \omega_2 - \omega_{ba}) + i\Gamma/2]} \end{aligned} \quad (\text{C.3a})$$

$$\begin{aligned} \chi_3^{\text{ASRS}} &= \chi_1^{\text{ASRS}} * \\ &= \left[\frac{N_b - N_a}{4\hbar\epsilon_0} \right] \left[\frac{1}{g_b} \right] \frac{\left[\sum_{M_b} \sum_{M_a} |\alpha_{1,3}|^2 \right]}{[(\omega_3 - \omega_1 - \omega_{ba}) + i\Gamma/2]} \end{aligned} \quad (\text{C.3b})$$

where N_b and N_a are the population densities, $g_b = 2J_b + 1$ is the degeneracy of $|b\rangle$, and Γ is the two photon transition linewidth (FWHM).

$$w_{ba}^{\text{TPE}} = \left[\frac{\Gamma/2}{(\omega_1 + \omega_2 - \omega_{ba})^2 + (\Gamma/2)^2} \right] \frac{|E_1|^2 |E_2|^2}{8 \hbar^2 g_b} \sum_{M_b} \sum_{M_a} |\alpha_{1,2}|^2 \quad (\text{C.4a})$$

$$w_{ba}^{\text{ASRS}} = \left[\frac{\Gamma/2}{(\omega_3 - \omega_1 - \omega_{ba})^2 + (\Gamma/2)^2} \right] \frac{|E_3|^2 |E_1|^2}{8 \hbar^2 g_b} \sum_{M_b} \sum_{M_a} |\alpha_{1,3}|^2 \quad (\text{C.4b})$$

$$\alpha_{1,2} = \sum_{\mathbf{k}} \left[\frac{\langle a | \hat{\epsilon}_2^* \cdot \vec{\mu} | \mathbf{k} \rangle \langle \mathbf{k} | \hat{\epsilon}_1^* \cdot \vec{\mu} | b \rangle}{\hbar(\omega_{\mathbf{k}b} + \omega_1)} + \frac{\langle a | \hat{\epsilon}_1^* \cdot \vec{\mu} | \mathbf{k} \rangle \langle \mathbf{k} | \hat{\epsilon}_2^* \cdot \vec{\mu} | b \rangle}{\hbar(\omega_{\mathbf{k}b} + \omega_2)} \right] \quad (\text{C.5a})$$

$$\alpha_{1,3} = \sum_{\mathbf{k}} \left[\frac{\langle a | \hat{\epsilon}_3^* \cdot \vec{\mu} | \mathbf{k} \rangle \langle \mathbf{k} | \hat{\epsilon}_1 \cdot \vec{\mu} | b \rangle}{\hbar(\omega_{\mathbf{k}b} - \omega_1)} + \frac{\langle a | \hat{\epsilon}_1 \cdot \vec{\mu} | \mathbf{k} \rangle \langle \mathbf{k} | \hat{\epsilon}_3^* \cdot \vec{\mu} | b \rangle}{\hbar(\omega_{\mathbf{k}b} + \omega_3)} \right] \quad (\text{C.5b})$$

Since two photon transitions are second order processes, a summation over intermediate states $|k\rangle \equiv |\gamma_k J_k M_k\rangle$ appears in Eqs.(C.5a and 5b). The expression in Eq.(C.5b) is the well known electric dipole form of the Raman scattering polarizability.⁵⁷ The corresponding term for two-photon emission has a similar form. These quantities contain the frequency dependence, the matrix elements, and the polarization properties of the two photon processes.

When the quantum numbers of a particular atomic or molecular system are specified the two photon transition formulas may be reduced to a more specific and useful form for applications. In particular the angular momentum quantum numbers yield explicit information on the polarization dependence of the matrix elements in Eqs.(C.5a and 5b). In atomic systems the total angular momentum J and the spatial component M are the essential quantities. In molecules the relevant quantities are the symmetry properties and the rotational and electronic angular momentum quantum numbers.

2. WIGNER-ECKART THEOREM AND IRREDUCIBLE TENSOR OPERATORS

The mathematical formalism for analyzing the polarization dependence of the matrix elements in Eqs.(C.5a and 5b) is the Wigner-Eckart theorem and the irreducible tensor operator algebra.^{39,56} The theorem is useful in computing the matrix element of a tensor operator as a product of

a "reduced matrix element" and a factor that contains the geometrical property of the operator and the angular momentum quantum numbers.

The Wigner-Eckart theorem states that the matrix element of the q-th component of an irreducible spherical tensor operator of rank k, $T_q^{(k)}$, is given by the following relation:⁵⁸

$$\begin{aligned} \langle \gamma J M | T_q^{(k)} | \gamma' J' M' \rangle &= (-1)^{J-M} \begin{pmatrix} J & k & J' \\ -M & q & M' \end{pmatrix} \\ &\times \langle \gamma J || T^{(k)} || \gamma' J' \rangle \end{aligned} \quad (C.6)$$

where γ represents all other relevant quantum numbers.

The spherical tensor components satisfy the following commutation relations with the angular momentum operator components.

$$[J_0, T_q^{(k)}] = q T_q^{(k)} \quad (C.7a)$$

$$[J_{+1}, T_q^{(k)}] = - \left[\frac{k(k+1) - q(q+1)}{2} \right]^{\frac{1}{2}} T_{q+1}^{(k)} \quad (C.7b)$$

$$[J_{-1}, T_q^{(k)}] = + \left[\frac{k(k+1) - q(q-1)}{2} \right]^{\frac{1}{2}} T_{q-1}^{(k)} \quad (C.7c)$$

The adjoint of the operator components satisfies

$$\left[T_q^{(k)} \right]^\dagger = (-1)^q \left[T_{-q}^{(k)} \right] \quad (C.8)$$

The factor in Eq. (C.6) containing six quantum numbers is the Wigner $3j$ symbol which represents the geometrical properties of the matrix element. Some of the properties of the $3j$ symbol includes i) the triangle rule for (J, K, J') , ii) $-M + q + M' = 0$, iii) invariance under even permutations of the columns, and iv) a possible sign change by $(-1)^{J+K+J'}$ under odd permutations of the columns or under a sign reversal of the bottom row. The numerical value of the $3j$ symbols can be computed from formulas or obtained from tables.⁵⁹

The $3j$ symbol is also related to the Clebsh-Gordan coefficient

$$\begin{pmatrix} j_1 & j_2 & j_3 \\ m_1 & m_2 & m_3 \end{pmatrix} = (-1)^{j_1 - j_2 - m_3} \frac{\langle j_1 m_1 j_2 m_2 | j_1 j_2 j_3 -m_3 \rangle}{\sqrt{2j_3 + 1}} \quad (C.9)$$

The double bar matrix element in Eq. (C.6) is the reduced matrix element which contains the physical parameters of the operator. Further reduction of the reduced matrix element may be obtained by specifying the coupling scheme of the angular momentum. In many atomic systems the Russell-Sanders coupling

of the total orbital angular momentum \vec{L} and the total electron spin \vec{S} to yield the total angular momentum $\vec{J} = \vec{L} + \vec{S}$ is a good approximation. However, intercombination transitions ($\Delta S \neq 0$) play an important role in heavier elements, and the intermediate coupling scheme must be used. Thus, a more accurate and practical method of computing the reduced matrix element in general is to evaluate it directly from experimental parameters. This computational method is discussed in Appendix D.

3. POLARIZATION PROPERTIES

The application of the Wigner-Eckart theorem in the two photon transition formulas first requires the definition of the tensor operator components. In the electric dipole approximation the operator is $\vec{\mu} = -e\vec{r}$, and the components are $\vec{\mu} \cdot \hat{\epsilon}$. Since $\vec{\mu}$ is a vector operator the rank is $k=1$,

$$\vec{\mu} = T^{(1)}, \quad (\text{C.10a})$$

and the spherical tensor components are

$$\mu_q = \vec{\mu} \cdot \hat{\epsilon}_q = T_q^{(1)} \quad (\text{C.10b})$$

where $\hat{\epsilon}_q$ is the unit vector defined by

$$\hat{\epsilon}_{+1} = -\frac{1}{\sqrt{2}} \left[\hat{\epsilon}_x + i\hat{\epsilon}_y \right] \quad (\text{C.11a})$$

$$\hat{\epsilon}_0 = \hat{\epsilon}_z \quad (\text{C.11b})$$

$$\hat{\epsilon}_{-1} = +\frac{1}{\sqrt{2}} \left[\hat{\epsilon}_x - i\hat{\epsilon}_y \right] \quad (\text{C.11c})$$

The unit vectors in the spherical tensor notation describe the circular polarizations, $\hat{\epsilon}_{+1}$ and $\hat{\epsilon}_{-1}$, when the propagation direction is along the z axis. This allows a direct application of the Wigner-Eckart theorem for treating the case of two circularly polarized collinear light beams.

The treatment of the cartesian polarization vectors, however, requires a linear combination of the spherical tensor components. For a light beam propagating along the y -axis the two allowed components are $\hat{\epsilon}_z$ and $\hat{\epsilon}_x$. From Eqs.(C.11a, 11b and 11c), the cartesian unit vectors are

$$\hat{\epsilon}_x = \frac{1}{\sqrt{2}} (\hat{\epsilon}_{-1} - \hat{\epsilon}_{+1}) \quad (\text{C.12a})$$

$$\hat{\epsilon}_y = \frac{i}{\sqrt{2}} (\hat{\epsilon}_{-1} + \hat{\epsilon}_{+1}) \quad (\text{C.12b})$$

$$\hat{\epsilon}_z = \hat{\epsilon}_0 \quad (\text{C.12c})$$

The electric dipole operator components are now expressed as

$$\vec{\mu} \cdot \hat{\epsilon}_z = T_0^{(1)} \quad (\text{C.13a})$$

$$\vec{\mu} \cdot \hat{\epsilon}_x = \frac{1}{\sqrt{2}} (T_{-1}^{(1)} - T_{+1}^{(1)}) \quad (\text{C.13b})$$

The substitution of the operator components from Eq.(C.10b) and Eqs.(C.13a and 13b) into the Wigner-Eckart theorem yields explicit polarization dependence of the matrix elements in Eqs.(C.5a and 5b). For circularly polarized beams the matrix elements are

$$\langle \gamma J M | \mu_{\pm 1} | \gamma' J' M' \rangle = (-1)^{J-M} \langle \gamma J || \vec{\mu} || \gamma' J' \rangle \begin{pmatrix} J & 1 & J' \\ -M & \pm 1 & M' \end{pmatrix} \quad (\text{C.14})$$

In the case of linearly polarized light,

$$\langle \gamma J M | \mu_z | \gamma' J' M' \rangle = (-1)^{J-M} \langle \gamma J || \vec{\mu} || \gamma' J' \rangle \begin{pmatrix} J & 1 & J' \\ -M & 0 & M' \end{pmatrix} \quad (\text{C.15a})$$

$$\begin{aligned} \langle \gamma J M | \mu_x | \gamma' J' M' \rangle &= (-1)^{J-M} \langle \gamma J || \vec{\mu} || \gamma' J' \rangle \\ &\times \frac{1}{\sqrt{2}} \left[\begin{pmatrix} J & 1 & J' \\ -M & -1 & M' \end{pmatrix} - \begin{pmatrix} J & 1 & J' \\ -M & +1 & M' \end{pmatrix} \right] \end{aligned} \quad (\text{C.15b})$$

The matrix elements of $\hat{\epsilon}_q^* \cdot \vec{\mu} = \mu_q^\dagger$ may be computed similarly using Eq.(C.8) or the relation

$$\langle \gamma J M | \mu_q^\dagger | \gamma' J' M' \rangle = \langle \gamma' J' M' | \mu_q | \gamma J M \rangle^* \quad (\text{C.16})$$

The matrix elements in Eq.(C.14) and Eqs.(C.15a and 15b) determine the polarization properties of the two photon transitions. The substitution of the matrix elements into Eqs. (C.5a and 5b) is straightforward and leads to the following formulas for various polarization cases.

Circular polarization

$$\alpha_{1,2} = (-1)^{J_a + J_b - M_a - M_b} \times \sum_k R_k \left\{ \frac{\begin{pmatrix} J_a & 1 & J_k \\ -M_a & -q_2 & M_k \end{pmatrix} \begin{pmatrix} J_b & 1 & J_k \\ -M_b & q_1 & M_k \end{pmatrix}}{\hbar(\omega_{kb} + \omega_1)} + \frac{\begin{pmatrix} J_a & 1 & J_k \\ -M_a & -q_1 & M_k \end{pmatrix} \begin{pmatrix} J_b & 1 & J_k \\ -M_b & q_2 & M_k \end{pmatrix}}{\hbar(\omega_{kb} + \omega_2)} \right\}$$

(C.17a)

where $M_b - M_a = q_1 + q_2$ with $q_1 = \pm 1$ and $q_2 = \pm 1$.

$$\alpha_{1,3} = (-1)^{J_a + J_b - M_a - M_b} \times \sum_k R_k \left\{ \frac{\begin{pmatrix} J_a & 1 & J_k \\ -M_a & -q_3 & M_k \end{pmatrix} \begin{pmatrix} J_b & 1 & J_k \\ -M_b & -q_1 & M_k \end{pmatrix}}{\hbar(\omega_{kb} - \omega_1)} + \frac{\begin{pmatrix} J_a & 1 & J_k \\ -M_a & q_1 & M_k \end{pmatrix} \begin{pmatrix} J_b & 1 & J_k \\ -M_b & q_3 & M_k \end{pmatrix}}{\hbar(\omega_{kb} + \omega_3)} \right\}$$

(C.17b)

where $M_b - M_a = q_3 - q_1$ with $q_1 = \pm 1$ and $q_3 = \pm 1$.

R_k is the product of reduced matrix elements given by

$$R_k = \langle \gamma_a J_a \parallel \vec{u} \parallel \gamma_k J_k \rangle \langle \gamma_b J_b \parallel \vec{u} \parallel \gamma_k J_k \rangle^* \quad (\text{C.17c})$$

Linear polarization

For parallel polarization vectors $\hat{\epsilon}_1 = \hat{\epsilon}_2 = \hat{\epsilon}_3 = \hat{\epsilon}_z$ gives

$$\alpha_{1,2} = (-1)^{J_a + J_b - M_a - M_b} \times \sum_k R_k \left\{ \begin{pmatrix} J_a & 1 & J_k \\ -M_a & 0 & M_k \end{pmatrix} \begin{pmatrix} J_b & 1 & J_k \\ -M_b & 0 & M_k \end{pmatrix} \left[\frac{1}{\hbar(\omega_{kb} + \omega_1)} + \frac{1}{\hbar(\omega_{kb} + \omega_2)} \right] \right\} \quad (\text{C.18a})$$

and

$$\alpha_{1,3} = (-1)^{J_a + J_b - M_a - M_b} \times \sum_k R_k \left\{ \begin{pmatrix} J_a & 1 & J_k \\ -M_a & 0 & M_k \end{pmatrix} \begin{pmatrix} J_b & 1 & J_k \\ -M_b & 0 & M_k \end{pmatrix} \left[\frac{1}{\hbar(\omega_{kb} - \omega_1)} + \frac{1}{\hbar(\omega_{kb} + \omega_3)} \right] \right\} \quad (\text{C.18b})$$

where $M_a = M_b = M_k$.

For perpendicular polarization vectors $\hat{\epsilon}_1 = \hat{\epsilon}_z$, $\hat{\epsilon}_2 = \hat{\epsilon}_x$,
and $\hat{\epsilon}_3 = \hat{\epsilon}_x$ give

$$\alpha_{1,2} = (-1)^{J_a + J_b - M_a - M_b} \quad (\text{C.19a})$$

$$\times \sum_k \frac{R_k}{\sqrt{2}} \left\{ \frac{\begin{pmatrix} J_b & 1 & J_k \\ -M_b & 0 & M_k \end{pmatrix} \left[\begin{pmatrix} J_a & 1 & J_k \\ -M_a & -1 & M_k \end{pmatrix} - \begin{pmatrix} J_a & 1 & J_k \\ -M_a & 1 & M_k \end{pmatrix} \right]}{\hbar(\omega_{kb} + \omega_1)} \right.$$

$$\left. + \frac{\begin{pmatrix} J_a & 1 & J_k \\ -M_a & 0 & M_k \end{pmatrix} \left[\begin{pmatrix} J_b & 1 & J_k \\ -M_b & -1 & M_k \end{pmatrix} - \begin{pmatrix} J_b & 1 & J_k \\ -M_b & 1 & M_k \end{pmatrix} \right]}{\hbar(\omega_{kb} + \omega_2)} \right\}$$

and

$$\alpha_{1,3} = (-1)^{J_a + J_b - M_a - M_b} \quad (\text{C.19b})$$

$$\times \sum_k \frac{R_k}{\sqrt{2}} \left\{ \frac{\begin{pmatrix} J_b & 1 & J_k \\ -M_b & 0 & M_k \end{pmatrix} \left[\begin{pmatrix} J_a & 1 & J_k \\ -M_a & -1 & M_k \end{pmatrix} - \begin{pmatrix} J_a & 1 & J_k \\ -M_a & 1 & M_k \end{pmatrix} \right]}{\hbar(\omega_{kb} - \omega_1)} \right.$$

$$\left. + \frac{\begin{pmatrix} J_a & 1 & J_k \\ -M_a & 0 & M_k \end{pmatrix} \left[\begin{pmatrix} J_b & 1 & J_k \\ -M_b & -1 & M_k \end{pmatrix} - \begin{pmatrix} J_b & 1 & J_k \\ -M_b & 1 & M_k \end{pmatrix} \right]}{\hbar(\omega_{kb} + \omega_3)} \right\}$$

The expressions in Eqs.(C.17), (C.18), and (C.19) are calculated for given values of M_b and M_a . The resulting sum is squared and summed over all possible values of M_b and M_a in order to obtain $\chi^{(3)}$ and $W^{(2)}$. In performing the summation over M_b and M_a some algebraic simplification can be made due to the properties of the 3j symbols. For the circular polarization case once q_1 and q_2 are specified, the restriction on M_k , M_a , and M_b reduces the summations to just one term for each value of M_b . In the parallel polarization case the summation over M_a and M_k is particularly simple since $M_a = M_b = M_k$. The summation over M_a and M_k in the perpendicular polarization case also leads to a more concise expression after some algebraic manipulation. The following formulas summarize the linear polarization cases.

Linear polarization

$$\sum_{M_b} \sum_{M_a} |\alpha_{1,2}|^2 = \sum_{M_b} \left| \sum_{\gamma_k} \sum_{J_k} R_k \left[\frac{S_p}{\hbar(\omega_{kb} + \omega_1)} + \frac{(-1)^p S_{-p}}{\hbar(\omega_{kb} + \omega_2)} \right] \right|^2$$

(C.20a)

$$\sum_{M_b} \sum_{M_a} |\alpha_{1,3}|^2 = \sum_{M_b} \left| \sum_{\gamma_k} \sum_{J_k} R_k \left[\frac{S_p}{\hbar(\omega_{kb} - \omega_1)} + \frac{(-1)^p S_{-p}}{\hbar(\omega_{kb} + \omega_3)} \right] \right|^2$$

(C.20b)

where $p = 0$ and $p = -1$ describe the parallel and perpendicular polarization cases, respectively. S_p and S_{-p} are the 3j symbol factors given by

$$S_p = \begin{pmatrix} J_b & 1 & J_k \\ -M_b & 0 & M_b \end{pmatrix} \begin{pmatrix} J_a & 1 & J_k \\ -M_b - p & p & M_b \end{pmatrix} \quad (\text{C.20c})$$

$$S_{-p} = \begin{pmatrix} J_b & 1 & J_k \\ -M_b & -p & M_b + p \end{pmatrix} \begin{pmatrix} J_a & 1 & J_k \\ -M_b - p & 0 & M_b + p \end{pmatrix} \quad (\text{C.20d})$$

$$R_k = \langle \gamma_a^{J_a} \parallel \vec{u} \parallel \gamma_k^{J_k} \rangle \langle \gamma_b^{J_b} \parallel \vec{u} \parallel \gamma_k^{J_k} \rangle^* \quad (\text{C.20e})$$

In summary the polarization properties of the two photon transitions can be analyzed by applying the Wigner-Eckart theorem to the electric dipole matrix elements. The 3j symbols yield the relationship between the polarization vectors and the angular momentum quantum numbers. Equations (C.17) through (C.20) are particularly useful when only a few intermediate states contribute significantly in Eqs.(C.5a and 5b). For example, if the reduced matrix elements are known, the interference behavior of $\chi^{(3)}$ can be analyzed for the various polarization conditions.^{44,60,61}

APPENDIX D

REDUCED MATRIX ELEMENT, SPONTANEOUS EMISSION RATE AND OSCILLATOR STRENGTH IN TWO PHOTON TRANSITIONS

The numerical computation of the nonlinear susceptibility and the transition rate for stimulated TPE and ASRS requires a knowledge of the energy levels and the electric dipole matrix elements of all intermediate states that connect the initial and the final states. In principle the necessary quantities may be calculated quantum mechanically using approximate wave functions. For hydrogenic systems²⁰ and alkali atoms^{62,63} such calculations are feasible. However, in practice, spectroscopic data and the experimental transition strengths provide a limited amount of the required information in many-electron atomic systems. This appendix describes useful relationships between the empirical quantities and the matrix elements and some methods of determining the relative signs of the products of reduced matrix elements, R_k , that appear in Eqs.(C.20a, 20b, 20c, 20d and 20e) of Appendix C.

In one photon transitions electric dipole matrix element determines the spontaneous emission rate, A , which is given by

$$A(\gamma J \rightarrow \gamma' J') = \frac{1}{2J+1} \left(\frac{4\omega^3}{3\hbar c^3} \right) \left| \langle \gamma J \| \vec{\mu} \| \gamma' J' \rangle \right|^2 \quad (D.1)$$

where ω is the transition frequency in radian-sec⁻¹. The reduced matrix element of $\vec{\mu}$ is also related to the oscillator strength f according to

$$f(\gamma J \rightarrow \gamma' J') = \frac{1}{2J+1} \left(\frac{2m\omega}{3\hbar e^2} \right) \left| \langle \gamma J \| \vec{\mu} \| \gamma' J' \rangle \right|^2 \quad (D.2)$$

Eq. (D.2) may be expressed in terms of other physical constants of atomic scale to give a simple formula for the square of the reduced matrix element.

$$\left| \langle \gamma J \| \vec{\mu} \| \gamma' J' \rangle \right|^2 = (2J+1) f(\gamma J \rightarrow \gamma' J') (ea_0)^2 \left(\frac{R}{\bar{\nu}} \right) \quad (D.3)$$

where e is the electron charge, a_0 is the Bohr radius, R is the Rydberg constant (109737 cm^{-1}), and $\bar{\nu}$ is the transition frequency in cm^{-1} . Since strongly allowed transitions have f values on the order of unity, Eq. (D.3) gives a reasonable estimate for the magnitude of the reduced matrix element when accurate data are not available.

The empirical parameters A and f determine only the magnitude of the reduced matrix element. The sign information cannot be obtained from one photon transition, since the reduced

matrix element always appears as a squared quantity. However, the sign of the reduced matrix element may be obtained theoretically for atomic systems in which the radial integrals can be computed numerically with reasonable accuracy.⁶²

Therefore, the combination of empirical parameters and approximate theoretical calculations provide one method of obtaining both the sign and the magnitude of the reduced matrix element.

For atomic systems in which the radial integrals are not available an analysis of the perturbed wave functions in the intermediate coupling scheme provides another semi-empirical technique for determining the relative signs of reduced matrix element products, R_k , in Eqs.(C.20a, 20b, and 20c). The analysis is based on the relationship between R_k and the mixing coefficients of the perturbed wave functions.

The angular momentum coupling scheme most often used to label atomic states is the Russel-Saunders case in which the total angular momentum is formed by a vector sum of the total orbital and the total spin angular momenta. This L-S coupling scheme is a good approximation when the electrostatic interaction among the electrons dominates over the spin-orbit interaction. However, in many atoms the spin-orbit interaction is a significant perturbation, and the perturbed states $|SLJM\rangle_I$ must be described by a linear combination of the L-S basis functions $|S'L'JM\rangle$.¹¹

$$|SLJM\rangle_I \propto |SLJM\rangle + \sum_{S'L'} C_{S'L'} |S'L'JM\rangle \quad (D.4)$$

where the mixing coefficients are given by

$$C_{S'L'} = \frac{\langle S'L'JM | \mathcal{H}_{\text{spin-orbit}} | SLJM \rangle}{(\mathcal{E} - \mathcal{E}')} \quad (\text{D.5})$$

\mathcal{E} and \mathcal{E}' are the unperturbed energies.

The formulas in Eqs. (D.4 and D.5) may be applied to a specific electron configuration using the tables of the spin-orbit interaction matrix elements¹¹ and the spectroscopic data for the perturbed energy levels. For example, a two-electron system with $s\ell$ configuration has the following perturbed states which are symbolically represented in the $^2S + ^1L_J$ notation.

$$|\gamma \ ^1L_\ell\rangle = \alpha |0L\ell M\rangle + \beta |1L\ell M\rangle \quad (\text{D.6a})$$

$$|\gamma \ ^3L_\ell\rangle = \alpha |1L\ell M\rangle - \beta |0L\ell M\rangle \quad (\text{D.6b})$$

$$|\gamma \ ^3L_{\ell\pm 1}\rangle = |1L\ell\pm 1 M\rangle \quad (\text{D.6c})$$

where $L = \ell$, and γ represents other relevant quantum numbers.

The mixing coefficients are given by¹¹

$$\frac{\beta}{\alpha} = \frac{1}{2} \xi \frac{\sqrt{\ell(\ell+1)}}{\epsilon_3 - \epsilon_1} \quad (\text{D.7a})$$

$$\alpha^2 + \beta^2 = 1 \quad (\text{D.7b})$$

where ξ is the spin-orbit interaction parameter determined from spectroscopic data, and $\epsilon_3 - \epsilon_1$ is the energy difference between the triplet and the singlet states due to electrostatic interaction.

Using Eqs.(D.6a, 6b, and 6c) the reduced matrix elements in the intermediate coupling scheme can be expressed in terms of the L-S coupling basis functions.

$$\begin{aligned} \langle \gamma \ ^1L_J || \vec{u} || \gamma' \ ^1L'_{J'} \rangle &= \alpha \alpha' \langle \gamma \ 0LJ || \vec{u} || \gamma' \ 0L'J' \rangle \\ &+ \beta \beta' \langle \gamma \ 1LJ || \vec{u} || \gamma' \ 1L'J' \rangle \end{aligned} \quad (\text{D.8a})$$

$$\begin{aligned} \langle \gamma \ ^1L_J || \vec{u} || \gamma' \ ^3L'_{J'} \rangle &= \alpha' \beta \langle \gamma \ 1LJ || \vec{u} || \gamma' \ 1L'J' \rangle \\ &- \alpha \beta' \langle \gamma \ 0LJ || \vec{u} || \gamma' \ 0L'J' \rangle \end{aligned} \quad (\text{D.8b})$$

$$\begin{aligned} \langle \gamma \ ^3L_J || \vec{u} || \gamma' \ ^3L'_{J'} \rangle &= \alpha \alpha' \langle \gamma \ 1LJ || \vec{u} || \gamma' \ 1L'J' \rangle \\ &+ \beta \beta' \langle \gamma \ 0LJ || \vec{u} || \gamma' \ 0L'J' \rangle \end{aligned} \quad (\text{D.8c})$$

Equation (D.8b) is significant in that the non-vanishing values of the reduced matrix element give rise to inter-combination ($\Delta S \neq 0$) transitions.

The reduced matrix element in the L-S coupling scheme may be simplified further using the following relation¹⁶.

$$\begin{aligned}
 & \langle \gamma S L J \| T^{(1)} \| \gamma' S' L' J' \rangle \\
 &= (-1)^{J' + L + S + 1} \sqrt{(2J + 1)(2J' + 1)} \\
 & \times \left\{ \begin{array}{ccc} L & J & S \\ & & \\ J' & L' & 1 \end{array} \right\} \langle \gamma L \| T^{(1)} \| \gamma' L' \rangle
 \end{aligned} \tag{D.9}$$

where the factor with the braces is the Wigner 6j symbol. Thus, the reduced matrix element for the $S=0$ and $S=1$ cases are proportional to a common factor as shown by the following relations.

$$\langle \gamma 0 L J \| \vec{\mu} \| \gamma' 0 L' J' \rangle = \sigma_{L J, L' J'} \langle \gamma L \| \vec{\mu} \| \gamma' L' \rangle \tag{D.10a}$$

and

$$\langle \gamma 1 L J \| \vec{\mu} \| \gamma' 1 L' J' \rangle = \tau_{L J, L' J'} \langle \gamma L \| \vec{\mu} \| \gamma' L' \rangle \tag{D.10b}$$

The parameters σ and τ are defined by

$$\sigma_{LJ, L'J'} = (-1)^{L+L'} \sqrt{(2L+3)(2L'+3)} \begin{pmatrix} L & L+1 & 0 \\ L'+1 & L' & 1 \end{pmatrix} \times \delta_{J, L+1} \delta_{J', L'+1} \quad (\text{D.11a})$$

$$\tau_{LJ, L'J'} = (-1)^{L+J'} \sqrt{(2J+1)(2J'+1)} \begin{pmatrix} L & J & 1 \\ J' & L' & 1 \end{pmatrix} \quad (\text{D.11b})$$

The numerical value of σ and τ can be computed by evaluating the 6j symbols using the tables.⁵⁹

The product of reduced matrix elements, R_k , in the intermediate coupling scheme can now be expressed in terms of the L-S coupling matrix elements using Eqs. (D.8a, 8b and 8c) and Eqs. (D.10a and 10b). The following formulas give R_k for various transitions.

$\Delta S = 0$ transitions

For singlet transitions between 1L_J and ${}^1L_{J''}$, the formulas are

$$\begin{aligned} & \langle \gamma \ ^1L_J \| \vec{\mu} \| \gamma' \ ^1L_{J'} \rangle \langle \gamma'' \ ^1L_{J''} \| \vec{\mu} \| \gamma' \ ^1L_{J'} \rangle^* \\ & = \lambda (\alpha \alpha' \sigma_{LJ, L'J'} + \beta \beta' \tau_{LJ, L'J'}) \quad (\text{D.12a}) \\ & \quad \times (\alpha' \alpha'' \sigma_{L''J'', L'J'} + \beta' \beta'' \tau_{L'', J'', L'J'}) \end{aligned}$$

and

$$\begin{aligned}
 & \langle \gamma \ ^1L_J \| \vec{\mu} \| \gamma' \ ^3L_{J'} \rangle \langle \gamma'' \ ^1L_{J''} \| \vec{\mu} \| \gamma' \ ^3L_{J'} \rangle^* \\
 & = \lambda (\alpha' \beta \tau_{L_J, L'J'} - \beta' \alpha \sigma_{L_J, L'J'}) \\
 & \quad \times (\alpha' \beta'' \tau_{L''J'', L'J'} - \alpha'' \beta' \sigma_{L''J'', L'J'})
 \end{aligned} \tag{D.12b}$$

where

$$\lambda = \langle \gamma L \| \vec{\mu} \| \gamma' L' \rangle \langle \gamma'' L'' \| \vec{\mu} \| \gamma' L' \rangle^* \tag{D.12c}$$

The formulas for triplet transitions between 3L_J and $^3L_{J''}$ are

$$\begin{aligned}
 & \langle \gamma \ ^3L_J \| \vec{\mu} \| \gamma' \ ^3L_{J'} \rangle \langle \gamma'' \ ^3L_{J''} \| \vec{\mu} \| \gamma' \ ^3L_{J'} \rangle^* \\
 & = \lambda (\alpha \alpha' \tau_{L_J, L'J'} + \beta \beta' \sigma_{L_J, L'J'}) \\
 & \quad \times (\alpha' \alpha'' \tau_{L''J'', L'J'} + \beta' \beta'' \sigma_{L''J'', L'J'})
 \end{aligned} \tag{D.13a}$$

and

$$\begin{aligned}
 & \langle \gamma \ ^3L_J \| \vec{\mu} \| \gamma' \ ^1L_{J'} \rangle \langle \gamma'' \ ^3L_{J''} \| \vec{\mu} \| \gamma' \ ^1L_{J'} \rangle^* \\
 & = \lambda (\alpha \beta' \tau_{L_J, L'J'} - \alpha' \beta \sigma_{L_J, L'J'}) \\
 & \quad \times (\alpha'' \beta' \tau_{L''J'', L'J'} - \alpha' \beta'' \sigma_{L''J'', L'J'})
 \end{aligned} \tag{D.13b}$$

$\Delta S = 1$ transitions

For intercombination transitions between 3L_J and $^1L''_{J''}$. The products of the reduced matrix elements are given by

$$\begin{aligned} & \langle \gamma \ ^3L_J \| \vec{\mu} \| \gamma' \ ^3L'_J \rangle \langle \gamma'' \ ^1L''_{J''} \| \vec{\mu} \| \gamma' \ ^3L'_J \rangle^* \\ & = \lambda (\alpha \alpha' \tau_{LJ, L'J'} + \beta \beta' \sigma_{LJ, L'J'}) \\ & \quad \times (\alpha' \beta'' \tau_{L''J'', L'J'} - \alpha'' \beta' \sigma_{L''J'', L'J'}) \end{aligned} \tag{D.14a}$$

and

$$\begin{aligned} & \langle \gamma \ ^3L_J \| \vec{\mu} \| \gamma' \ ^1L'_J \rangle \langle \gamma'' \ ^1L''_{J''} \| \vec{\mu} \| \gamma' \ ^1L'_J \rangle^* \\ & = \lambda (\alpha \beta' \tau_{LJ, L'J'} - \alpha' \beta \sigma_{LJ, L'J'}) \\ & \quad \times (\alpha' \alpha'' \sigma_{L''J'', L'J'} + \beta' \beta'' \tau_{L''J'', L'J'}) \end{aligned} \tag{D.14b}$$

Therefore, according to Eqs.(D.12a, 12b and 12c), Eqs. (D.13a and 13b), and Eqs. (D.14a and 14b) the relative signs of the products of reduced matrix element for each intermediate state having the same configuration may be determined in terms of the mixing coefficients and the numerical factors σ and τ defined in Eqs. (D.11a and 11b). Since states having the same configuration generally have

nearly the same energies, the above analysis is suitable for treating the near-resonance Raman scattering in the intermediate coupling scheme.

The effect of the sign of the reduced matrix element does not appear in one photon or linear optical process. However, nonlinear optical effects depend on the sign of the matrix element products according to Eqs. (C.5a and 5b). Thus, nonlinear optical processes may be used to experimentally determine the relative sign of the matrix element products.

One such method was demonstrated by Vriens and Adriaansz⁴⁴ using depolarization measurement of Raman scattering intensity as a function of frequency. The technique is based on a comparison between the experimentally measured depolarization ratio and the calculated values for Raman scattering near two intermediate states. Since Raman intensity depends on the polarization of the scattered light and the interference between the two intermediate states, the calculation can yield two different depolarization ratios corresponding to constructive and destructive interference cases.

The depolarization ratios are calculated using Eqs. (C.20a, 20b, 20c, 20d and 20e) and the known values of the magnitude of the reduced matrix elements for each of the two possible relative signs of the reduced matrix element products, R_k . Since the amount of interference depends on the frequency detuning from the intermediate states the calculated ratios also

depend on the incident field frequency. Therefore, a comparison of the experimental values and the calculated ratios at various frequencies determines the proper choice of the relative sign of R_k .

Proposed atomic mercury anti-Stokes frequency converter

H. Komine and R. L. Byer

Microwave Laboratory, W. W. Hansen Laboratories of Physics, Stanford University, Stanford, California 94305
(Received 20 March 1975; in final form 9 June 1975)

We propose to use population stored in the radiatively trapped $6^3P_1^o$ atomic mercury resonant level (1850 Å) for frequency conversion by an anti-Stokes or two-photon process. Inversion is with respect to the lower-lying $6^3P_{0,1,2}^o$ levels which are assumed empty following selective quenching or rapid conversion to the mercury dimer. Photon conversion gains of 2.5×10^{-2} cm/MW for 1.06- μ m and 8.7×10^{-5} cm/MW for 10.6- μ m input wavelengths with corresponding 0.4157- and 0.9116- μ m output wavelengths are calculated at a 10^{16} - cm^{-3} inversion density.

PACS numbers: 32.10.K, 42.60.L

Recent requirements for high-energy laser sources and frequency conversion of existing high-energy lasers to shorter wavelengths for application to laser fusion has led to reconsideration of the two-photon laser first proposed by Sorokin and Braslau.¹ In its ideal form the two-photon laser stores energy in a metastable level without superfluorescence limiting until induced to emit by an intense input trigger pulse. Inversion densities of greater than 10^{18} cm^{-3} are needed to obtain adequate energy storage and gain for the two-photon scattering process. To avoid superfluorescence at the high inversion densities, an energy level scheme must be found that precludes any single-photon transition out of the inverted level. Unfortunately, the high inversion density and level scheme requirements have not yet allowed the two-photon laser to be achieved in the laboratory.

The atomic iodine system with inversion produced by photodissociation on the spin orbit split $5^2P_{1/2}$ - $5^2P_{3/2}$ (1.315 μ m) ground-state transition has been suggested as a candidate for two-photon conversion.² Unfortunately, the inversion density is limited to approximately 3×10^{18} cm^{-3} by superfluorescence which leads to a low saturation intensity and anti-Stokes gain.³ The lack of nearby atomic levels to resonantly enhance the third-order susceptibility also limits the gain in the iodine system. Nevertheless, Carmen and Lowdermilk⁴ have demonstrated $e^{7.2}$ gain in iodine using a visible dye laser to probe the anti-Stokes up-shifted 1.06- μ m pump wave.

An investigation of the Periodic Table for atomic systems with metastable levels that allow energy storage and two-photon processes showed that there are very few candidates. Of those investigated, a number such as Tl are similar to iodine with split ground-state levels. In such cases inversion must be obtained with respect to the ground state making a high inversion density difficult to achieve. None of the atomic systems with higher-lying metastable levels met the requirement of no single-photon radiative decay from the upper two-photon level.

However, atomic mercury, though lacking a truly metastable state above the $6^3P_{0,1,2}^o$ levels does offer the possibility of obtaining inversion between the $6^1P_1^o$ and $6^3P_{0,1,2}^o$ levels. The $6^1P_1^o$ level does not decay by single-photon decay to the lower-lying $6^3P_{0,1,2}^o$ levels. Furthermore, it is radiatively trapped with respect to the 6^1S_0 ground state at high vapor densities, thus becoming

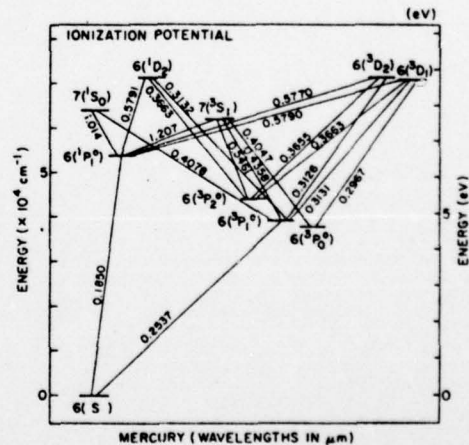
effectively metastable. In addition, the higher-lying mercury levels with their relatively strong singlet-triplet intercombination transitions provide resonant enhancement of the susceptibility, leading to significantly improved anti-Stokes and two-photon gains.

Figure 1 shows a simplified energy level diagram for atomic mercury. For the present case, we assume that the $6^1P_1^o$ level is inverted with respect to the $6^3P_{0,1,2}^o$ levels. Possible methods for obtaining the required inversion are discussed later.

If we let i and f denote the initial (${}^iP_1^o$) and final (${}^fP^o$) levels of mercury and let I_1 and I_2 be the input intensity and the output anti-Stokes or two-photon intensity, then the equations governing the generated intensities are

$$\begin{aligned} dI_1/dz &= \pm \delta_1 I_2 I_1, \\ dI_2/dz &= \delta_2 I_1 I_2, \end{aligned} \quad (1)$$

where the positive sign applies to the two-photon process where $\omega_{if} = \omega_1 + \omega_2$, and the negative sign describes the anti-Stokes case where $\omega_{if} + \omega_1 = \omega_2$. The gain coefficients related by their frequency ratio $\delta_1/\delta_2 = \omega_1/\omega_2$ are given by



$$\delta_n = \omega_n \Delta N \left| \sum_a \mu_a^{(1)} \mu_a^{(2)} \right|^2 / 2N^2 c^2 \epsilon_0^2 n_1 n_2 \Delta \omega_{f1}, \quad (2)$$

where ΔN is the population inversion density, n_1 and n_2 are indices of refraction, and $\Delta \omega_{f1}$ is the effective linewidth of the two-photon levels or the incident laser linewidth whichever is larger. The summation term is

$$\left| \sum_a \mu_a^{(1)} \mu_a^{(2)} \right|^2 = \left| \sum_a \frac{\mu_a^{(1)} \mu_a^{(2)}}{\omega_1 \pm \omega_{a1}} \pm \frac{\mu_a^{(1)} \mu_a^{(2)}}{\omega_2 \pm \omega_{a1}} \right|^2, \quad (3)$$

where the superscripts indicate the dipole component projection in the polarization direction of wave (1) or (2) and the plus and minus signs again denote the two-photon and anti-Stokes processes.

Equation (1) shows the two-photon process results in gain at both I_1 and I_2 while the anti-Stokes process depletes I_1 during the conversion to I_2 . However, the equations describe a simplified interaction in which conversion losses to higher-order Stokes and competing two-photon or anti-Stokes processes are neglected. Similarly, saturation of the inversion is also not included. Limitations due to competing processes and saturation have been recently considered.³ Here we assume that one process dominates and leads to depletion of the input wave or the population inversion before significant losses occur via other channels. This situation applies to stimulated Raman scattering and has been considered for that case.⁵ For stimulated Raman scattering approximately 40% photon conversion efficiency is reached before higher-order Stokes generation becomes important. A similar photon conversion efficiency should be possible for the two-photon and anti-Stokes processes.

The anti-Stokes gain factors given by Eq. (2) are listed in Table I for 1.06- and 10.6- μm input wavelengths. The summation is taken over intermediate states for which oscillator strengths⁶⁻¹⁰ and signs^{11,12} are known. For the 1.06- μm input, close-lying intermediate levels for the anti-Stokes case provide significant gain improvement. The two-photon gain for both 1.06- and 10.6- μm inputs is slightly less than the 10.6- μm anti-Stokes gain owing to the lack of resonant intermediate states between the 6^1P_1 and $6^3P_{0,1,2}$ levels. The calculated unsaturated gains assume a 10^{18}-cm^{-3} inversion density and a linewidth determined by pressure broadening of the 6^1P_1 resonance level.¹³ These gains are more than adequate for efficient single-pass anti-Stokes conversion at intensities of less than 10^9 W/cm² which is well below gas breakdown intensity limits for even 1 atm of total mercury vapor pressure.

Atomic mercury meets the requirements for a potential two-photon or anti-Stokes laser medium if population inversion can be achieved. It is not yet clear whether electrical excitation methods will produce high inversion densities. However, radiation trapping of the 6^1P_1 level and rapid quenching of the $6^3P_{0,1,2}$ levels enhance the probability of success.

Radiation trapping is well known and has been considered in detail by Holstein.¹⁴ The trapped lifetime τ in a cylinder of radius R is considerably increased over the untrapped radiative lifetime by the factor $1/g$ where

$$g \approx (\pi k_p R)^{-1/2}, \quad (4)$$

$$k_p = \frac{\lambda^2 N g_1 g_2 \gamma_n}{2\pi g_1 \gamma_p},$$

where k_p is the absorption coefficient on line center, N is the ground-state population density, g_1 and g_2 are the level degeneracies, and γ_n and γ_p are the natural and pressure-broadened linewidths.

The absorption coefficient increases with pressure until the pressure-broadened linewidth equals the Doppler width. For the 6^1P_1 - 6^1S_0 (1850 Å) resonant transition in mercury, the density at which this occurs is near $2 \times 10^{16} \text{ cm}^{-3}$ at 300°C. At this density $k_p \approx 1.6 \times 10^6$ and $g \approx 4.4 \times 10^{-4}$. The radiatively trapped lifetime of the transition is therefore approximately 3 μsec in a 1-cm-diam cylinder. Apparent lifetimes as long as 20 μsec have been observed.¹⁵

Radiation trapping is also present for the triplet-to-singlet 2537-Å resonant line. However, in this case, unlike the 1850-Å transition, quenching by foreign gas molecules such as hydrogen is very effective in rapidly reducing the triplet level population. Based on measured quenching cross sections,^{16,17} 1 Torr of hydrogen in 100 Torr of mercury vapor leads to triplet level quenching in approximately 10^{-7} sec, which is 30 times shorter than the radiatively trapped 6^3P_1 lifetime. Furthermore, H_2 has a significantly smaller cross section for quenching the 6^1P_1 level compared to the 6^3P_1 level¹⁸ and H_2 does not collisionally induce a 6^1P_1 -to- 6^3P_1 intersystem transition.¹⁹ Thus selective quenching may enable population inversion to be achieved in the afterglow of a mercury discharge. Additional processes such as the formation of Hg_2 dimer molecules from the triplet levels may also proceed rapidly enough at higher pressures to reduce the triplet level population. Based on the measured rate constant²⁰ for the production of

TABLE I. Anti-stokes and two-photon gains in atomic mercury for 1.06- and 10.6- μm input wavelengths.

λ_1	$ f\rangle$	Anti-Stokes Raman			Two-photon emission		
		λ_2 (μm)	δ_1 (cm/MW)	δ_2	λ_2 (μm)	δ_1 (cm/MW)	δ_2
1.06 μm	$6^3P_2^o$	0.5148	-2.0×10^{-2}	4.1×10^{-2}	15.94	7.4×10^{-4}	5.0×10^{-5}
	$6^3P_1^o$	0.4157	-2.5×10^{-2}	6.5×10^{-2}	1.902	3.5×10^{-4}	2.0×10^{-4}
	$6^3P_0^o$	0.3873	-3.8×10^{-2}	1.1×10^{-2}	1.423	7.8×10^{-5}	5.8×10^{-5}
10.6 μm	$6^3P_2^o$	0.9116	-8.7×10^{-5}	1.0×10^{-3}	1.101	7.2×10^{-5}	7.0×10^{-4}
	$6^3P_1^o$	0.6410	-5.4×10^{-5}	9.2×10^{-4}	0.7292	4.3×10^{-5}	6.2×10^{-4}
	$6^3P_0^o$	0.5758	-1.4×10^{-5}	2.6×10^{-4}	0.6460	1.1×10^{-5}	1.8×10^{-4}

Hg_2^* from $\text{Hg} (^3P_0)$ of $k = 3.4 \pm 1.7 \times 10^{-31} \text{ cm}^6 \text{ mol}^{-2} \text{ sec}^{-1}$ the formation rate of Hg_2^* is $3.4 \times 10^7 \text{ sec}^{-1}$ at $N = 10^{19} \text{ cm}^{-3}$. Thus at pressures above 100 Torr depopulation of the triplet levels by dimer formation is rapid enough to ensure inversion.

Electrical excitation of mercury has been the subject of theoretical studies.²¹⁻²³ Rockwood²² has calculated excitation rates to the singlet and triplet levels from previously measured electron scattering cross sections for mercury using a comprehensive model. Binary excitation rates to the 6^1P_1 and $6^3P_{0,1,2}$ levels are approximately 10^{-10} and $10^{-9} \text{ cm}^3/\text{sec}$ at an E/N of 10^{-15} V cm^2 . Excitation to higher-lying atomic levels is negligible. These excitation rates lead to high fractional excitation of the mercury electronic levels for E/N in the range of $3 \times 10^{-17} - 10^{-15} \text{ cm}^2$. Furthermore, at E/N near 10^{-16} V cm^2 the fractional ionization is small such that electron-electron collisions are not important and thermalization of the medium is avoided.

Although population inversion in mercury by electrical excitation has not been demonstrated experimentally, the two-photon and anti-Stokes gains calculated in this paper can be measured. One approach is to use two-photon absorption at the 6^1S_0 -to- 7^1S_0 transition to populate the 7^1S_0 level which subsequently decays to the lower 6^1P_1 level creating the required population inversion with respect to the $6^3P_{0,1,2}$ levels. A second approach is to use resonance excitation at 2537 \AA to populate the $6^3P_{0,1}$ levels and measure the cross section to the 6^1P_1 level by Raman scattering on the noninverted population density.

In summary we have shown that atomic mercury has high two-photon and anti-Stokes gain coefficients for inversion between the 6^1P_1 and $6^3P_{0,1,2}$ levels. At mercury densities of 10^{16} cm^{-3} or greater electrical excitation of the radiatively trapped 6^1P_1 level followed by rapid quenching of the $6^3P_{0,1,2}$ levels by hydrogen or Hg_2^* formation may provide a possible method to obtain the required population inversion without the superfluorescence limit characteristic of single-photon amplifiers. Finally, anti-Stokes amplifiers may be advantageous in laser fusion applications by providing, in addition to frequency up-conversion, isolation from waves reflect-

ed back from the target due to nonlinear frequency conversion and to amplifier saturation.

The authors wish to acknowledge helpful discussions with S. E. Harris and the support of Stanford Center for Materials Research.

- ¹P. P. Sorokin and N. Braslau, *IBM J. Res. Develop.* **8**, 177 (1964).
- ²A. V. Vinograd and E. A. Yukov, *JETP Lett.* **16**, 447 (1972).
- ³J. R. Murray, C. K. Rhodes, and R. L. Carmen, Paper No. D. 9, VIII International Quantum Electronics Conference, 1974, San Francisco, Calif. (unpublished).
- ⁴R. L. Carmen and W. H. Lowdermilk, in Ref. 3, Paper No. H. 6.
- ⁵D. Van der Linde, M. Maier, and W. Kaiser, *Phys. Rev.* **178**, 11 (1969).
- ⁶C. H. Corliss and W. R. Bozman, *Experimental Transition Probabilities for Spectral Lines of Seventy Elements*, NBS Monograph 53 (U.S. Government Printing Office, Washington, D. C., 1962).
- ⁷A. Lurio, *Phys. Rev.* **140**, A1505 (1965).
- ⁸R. J. Anderson, E. T. P. Lee, and C. C. Lin, *Phys. Rev.* **157**, 31 (1967).
- ⁹S. E. Frisch and A. N. Klucharyov, *Opt. Spectros.* **22**, 92 (1967).
- ¹⁰P. Jean, M. Martin, J. P. Barrat, and J. L. Cojan, *C. R. Acad. Sci. B* **264**, 1709 (1967).
- ¹¹M. C. Bignon, *J. Phys. (Paris)* **28**, 51 (1967).
- ¹²Y. Lecluse, *J. Phys. (Paris)* **28**, 671 (1967).
- ¹³W. R. Hindmarsh and J. M. Farr, in *Progress in Quantum Electronics*, 1st. ed., edited by J. H. Sanders and S. Stenholm (Pergamon, New York, 1972), Vol. 2, Part 3.
- ¹⁴T. Holstein, *Phys. Rev.* **83**, 1159 (1951).
- ¹⁵J. A. Aubrecht, B. M. Whitcomb, R. A. Anderson, and R. C. Pickett, *J. Opt. Soc. Am.* **58**, 196 (1968).
- ¹⁶A. C. G. Mitchell and M. W. Zemansky, *Resonance Radiation and Excited Atoms* (Cambridge U. P., Cambridge, England, 1971).
- ¹⁷J. G. Calvert and J. N. Pitts, *Photochemistry* (Wiley, New York, 1967).
- ¹⁸A. Granzow, M. Z. Hoffman, and N. N. Lichten, *J. Phys. Chem.* **73**, 4289 (1969).
- ¹⁹V. Madhavan, N. N. Lichten, and M. Z. Hoffman, *J. Phys. Chem.* **77**, 875 (1973).
- ²⁰A. G. Ladd, C. G. Freeman, M. J. McEwan, R. F. C. Claridge, and L. F. Phillips, *J. Chem. Soc. Faraday Trans. II* **69**, 849 (1973).
- ²¹J. C. McConnell and B. L. Moiseiwitsch, *J. Phys. B* **1**, 406 (1968).
- ²²S. D. Rockwood, *Phys. Rev. A* **8**, 2348 (1973).
- ²³S. D. Rockwood, *J. Appl. Phys.* **45**, 5229 (1974).

REFERENCES

1. Steinfeld, J. I., ed., Electronic Transition Lasers, (The M.I.T. Press, Cambridge, Mass., 1975).
2. Komine, H. and R. L. Byer, (to be published in J. Chem. Phys., 1977). (See Appendix A)
3. Sorokin, P. P. and N. Braslau, IBM J. Res. Dev., 8, 177 (1964).
4. Prokhorov, A. M., Science, 149, 828 (1965).
5. Letokhov, V. S., JETP Lett., 7, 221 (1968).
6. Carman, R. L., Phys. Rev. A, 12, 1048 (1975).
7. Komine, H. and R. L. Byer, Appl. Phys. Lett., 27, 300 (1975). (See Appendix E)
8. Vinogradov, A. V. and E. A. Yukov, JETP Lett., 16, 447 (1972).
9. Kasper, J. V. V. and G. C. Pimentel, Appl. Phys. Lett., 5, 231 (1964); Kasper, J. V. V., J. H. Parker, and G. C. Pimentel, Phys. Rev. Lett., 14, 352 (1965).
10. Hohla, K. and K. L. Kompa, in Handbook of Chemical Lasers, J. F. Bott and F. Gross, eds., (Wiley, New York, 1976), p. 667.
11. Condon, E. U. and G. H. Shortley, The Theory of Atomic Spectra, (University Press, Cambridge, England, 1970), Chap. IV, VII, VIII, IX.
12. Mrozowski, S., Rev. Mod. Phys., 16, 153 (1944).

13. Opechowski, W., Zeits. fur Physik, 109, 485 (1938).
14. Herzberg, G., Molecular Spectra and Molecular Structure
v. I: Spectra of Diatomic Molecules, 2nd. ed., (Van
Nostrand Reinhold Company, New York, 1950), Chap. V.
15. Mulliken, R. S., Phys. Rev. 36, 699 (1930).
16. Mizushima, M., Quantum Mechanics of Atomic Spectra and
Atomic Structure, (W. A. Benjamin Inc., New York,
1970)
17. Einaudi, F. R., Rend. R. Acad. dei Lincei, 17, 552
(1933).
18. Goepfert-Mayer, M., Ann. der Phys., 9, 23 (1931).
19. Breit, G. and E. Teller, Astrophys. J., 91, 215 (1940).
20. Shapiro, J. and G. Breit, Phys. Rev., 113, 179 (1959).
21. Dalgarno, A., in Physics of the One- and Two- Electron
Atoms, F. Bopp and H. Kleinpoppen, eds., (North-Holland,
Amsterdam, 1969), p. 261.
22. Lipeles, M., R. Novick, and N. Tolk, Phys. Rev. Lett.,
15, 690 (1965).
23. Elton, R. C., L. J. Palumbo, and H. R. Griem, Phys.
Rev. Lett., 20, 783 (1968).
24. Yatsiv, S., M. Rokni, and S. Barak, Phys. Rev. Lett.,
20, 1282 (1968).

25. Fornaca, G., F. Giammanco, A. Giuliotti, and M. Vaselli, *Lett. al Nuovo Cimento*, 9, 395 (1973).
26. Yariv, A., Quantum Electronics, 2nd. ed., (Wiley, New York, 1975), Chap. 12.
27. Aldridge, F. T., *Appl. Phys. Lett.*, 22, 180 (1973).
28. Calvert, J. G. and J. N. Pitts, Photochemistry, (Wiley, New York, 1966), Chap. 2.
29. Mitchell, A. C. G. and M. W. Zemansky, Resonance Radiation and Excited Atoms, (Cambridge U. P., Cambridge, England, 1971), Chap. 4.
30. Bochkova, O., S. Frish, and Yu. Tolmachev, *Opt. Comm.*, 7, 423 (1973).
31. Stock, M., E. W. Smith, R. E. Drullinger, and M. M. Hessel, (unpublished).
32. Drullinger, R. E., M. M. Hessel, and E. W. Smith, *J. Chem. Phys.*, 66, 5656 (1977).
33. See, for example, Lavigne, P., J. C. Lachambre, and J. Gilbert, *Appl. Phys. Lett.*, 28, 265 (1976).
34. Gordon, E. B. and Yu. L. Moskvin, *Sov. Phys. JETP*, 43, 901 (1976).
35. Yuen, H. P., *Appl. Phys. Lett.*, 26, 505 (1975).
36. Pantell, R. H. and H. E. Puthoff, Fundamentals of Quantum Electronics, (Wiley, New York, 1969), Chap. 1,3,5.

37. Carman, R. L., F. Shimizu, C. S. Wang, and N. Bloembergen, Phys. Rev. A 2, 60 (1970).
38. See, for example, Dirac, P. A. M., Quantum Mechanics, 3rd. ed., (Oxford U. P., London and New York, 1958), p.248.
39. Penney, C. M., J. O. S. A., 59, 34 (1969).
40. Harris, S. E., (private communication).
41. Lurio, A., Phys. Rev. 140, 5A, 1505 (1965).
42. Holstein, T., Phys. Rev., 72, 1212 (1947); Phys. Rev., 83, 1159 (1951).
43. Bjorkholm, J. E. and P. F. Liao, Phys. Rev. Lett., 33, 128 (1974).
44. Vriens, L. and M. Adriaansz, J. Appl. Phys., 46, 3146 (1975); Opt. Commun., 11, 402 (1974).
45. Djeu, N. and R. Burnham, Appl. Phys. Lett., 30, 473 (1977) and references therein.
46. Harris, S. E. and D. M. Bloom, Appl. Phys. Lett., 24, 229 (1974).
47. Hodgson, R. T., P. P. Sorokin, and J. J. Wynne, Phys. Rev. Lett., 32, 343 (1970).
48. Jean, P., M. Martin, J.-P. Barrat, J.-L. Cojan, Comptes Rend., 264 B, 1709 (1967).
49. Anderson, R. J., E. T. P. Lee, and C. C. Lin, Phys. Rev., 157, 31 (1967).

50. Frisch, S. E. and A. N. Klucharyov, *Opt. and Spectro.*, 22, 92 (1967).
51. Bigeon, M. C., *J. Physique*, 28, 51 (1967).
52. LeCluse, Y., *J. Physique*, 28, 671 (1967).
53. Carman, R. L. and W. H. Lowdermilk, Paper No. H. 6, VIII International Quantum Electronics Conference, 1974, San Francisco, Calif., (unpublished).
54. Brosnan, S. J., R. N. Fleming, R. L. Herbst, and R. L. Byer, *Appl. Phys. Lett.*, 30, 330 (1977).
55. See for example, Van der Linde, D., M. Maier, and W. Kaiser, *Phys. Rev.* 178, 11 (1969).
56. Yuratich, M. A. and D. C. Hanna, *J. Phys. B: Atom. Molec. Phys.*, 9, 729 (1976).
57. Szymanski, H. A., ed., Raman Spectroscopy: Theory and Practice Vol. II, (Plenum Press, New York, 1970), Chap. 2.
58. Edmonds, A. R., Angular Momentum in Quantum Mechanics, (Princeton University Press, Princeton, New Jersey, 1957), Chap. 5.
59. Rotenberg, M., R. Bivins, N. Metropolis, and J. K. Wooten, Jr., The 3j and 6j Symbols, (Technology Press, Cambridge, Mass., 1959).
60. Cotter, D. and D. C. Hanna, *J. Phys. B: Atom. Molec. Phys.*, 9, 2165 (1976).

61. Vriens, L., Opt. Commun., 11, 396 (1974).
62. Bates, D. R. and A. Damgaard, Phil. Trans. Roy. Soc. London, A 242, 101 (1949).
63. Miles, R. B. and Harris, S. E., IEEE J. Quantum Electron., 9, 470 (1973).